Light-controlled self-assembly

Crystallization in the spotlight

ACADEMISCH PROEFSCHRIFT

ter verkrijging van de graad van doctor
aan de Universiteit van Amsterdam
op gezag van de Rector Magnificus
Prof. Dr. ir. P. P. C. C. Verbeek
en overstaan van een door het College voor Promoties ingestelde
commissie, in het openbaar te verdedigen in de Aula der Universiteit
op vrijdag 29 november 2024, te 17.00 uur

door

Marloes Houkje Bistervels

geboren te Nieuwegein, Nederland

Promotiecommissie:

Promotor:	Prof. Dr. W.L. Noorduin	Universiteit van Amsterdam
Copromotor:	Prof. Dr. A.M. Brouwer	Universiteit van Amsterdam
Overige leden:	Prof. Dr. E. Alarcon Llado	Universiteit van Amsterdam
	Prof. Dr. N. Shahidzadeh	Universiteit van Amsterdam
	Dr. S. Jabbari Farouji	Universiteit van Amsterdam
	Prof. Dr. A. De Wit	Vrije Universiteit Brussel
	Prof. Dr. M. Wolthers	Universiteit Utrecht
	Prof. Dr. D. Wilson	Radboud Universiteit Nijmegen

Faculteit der Natuurwetenschappen, Wiskunde en Informatica

UNIVERSITEIT VAN AMSTERDAM

Het hier beschreven onderzoek is uitgevoerd binnen de groep van prof. dr. Willem L. Noorduin aan het AMOLF (gevestigd te Science Park 104, 1098 XG, Amsterdam). Het onderzoek is gedeeltelijk gefinancieerd door de Nederlandse Organisatie voor Wetenschappelijk Onderzoek (NWO) als onderdeel van het Vidi onderzoeks programma “Shaping up materials” met project nummer 016.Vidi.189.083

ISBN: 978-94-6506-645-5

Cover design:
Eye of author interlaced with single $BaCO_3$-silica nanocomposite crystal.
Conceptualization by Lisa Hopf.
Photograph by Bart Bistervels.
Production by Marloes Bistervels.

Printed by Ridderprint.

A digital copy of this thesis can be obtained via `dare.uva.nl` or `ir.amolf.nl`

The author can be reached at: `marloesbistervels@gmail.com`

Contents

List of Figures

List of Abbreviations

CNT	Classical Nucleation Theory
NCNT	Non-Classical Nucleation Theory
LIN	Laser-induced Nucleation
$CaCO_3$	Calcium carbonate
ACC	amorphous calcium carbonate
MCO_3/SiO_2	nanocomposites of nanocrystalline earth alkali metal carbonates with amorphous silica
SAM	Self-assembled monolayers
MCO_3	Alkali metal carbonate
UV	Ultraviolet
MCGb	Malachite green carbinol base
LIN	Laser-induced Nucleation
NIR	Near-infrared
KP	Ketoprofen
DTAB	Dodecyltrimethylammonium bromide
SEM	Scanning electron microscopy
EDS	Energy Dispersion Spectroscopy
XRD	X-Ray diffraction analysis
ND	Neutral density
CO_2	Carbon dioxide
LED	Light emitting diode
ITO	indium tin oxide
HPTS	8-hydroxypyrene-1,3,6-trisulfonic trisodium salt
SDS	Sodium dodecyl sulfate
3D	Three-dimensional
GBL	Gamma-butyrolactone
DMF	Dimethylformamide
DMSO	Dimethyl sulfoxide
LSCT	Lower solution critical temperature
L-W	2,6 lutidine-water

List of Symbols & Physical Constants

T	Temperature	degrees Celsius (°C)
G	Gibss free energy	joule (J)
μ	Chemical potential	energy units per mole of the substance (J mol^{-1})
γ	Surface tension	newton per meter (N m^{-1})
V_m	Volume per building unit	cubic meter (m^3)
σ	Supersaturation	moles per milliliter (mol mL^{-1})
a_i	Molar concentration of the species i	moles per milliliter (mol mL^{-1})
r	radius	meter (m)
I_{UV}	Light irradiance	watt per millimeter square (J s^{-1} mm^{-2})
I_{NIR}	Laser diode output power	watt (J s^{-1})
f	Focal length	millimeter (mm)
NA	Numerical Aperture	dimensionless
k_b	Boltzmann constant	1.3806452e-23 J K^{-1}
R	Gas constant	8.314 J mol^{-1} K^{-1}

Dedicated to the scientific community,
with gratitude for the lessons learned
and the knowledge shared.

Chapter 1

Introduction

Controlling local gradients at the right time and place enables living organisms to autonomously form basic building blocks into intricate mineral crystal architectures with remarkable physicochemical properties, including structural resilience,[1,2] protective efficacy,[3] and sensory enhancement[4]—essential for the sustenance and survival of life forms.[5–10] If humans could harness the potential of this type of self-assembly in a similar manner, it could unlock a myriad of new structures and fabricate materials with unimaginable properties. Intrigued by this thought, researchers have explored routes to synthetically replicate such biorelevant crystals.[11–16] Specifically, achieving spatiotemporal control in these syntheses can lead to a profound understanding of the constructive crystallization processes in nature and serve as a foundation for innovative synthetic routes to create unprecedented functional materials based on user-defined designs. Nevertheless, replicating nature's remarkable autonomous dynamic regulation at the sub-micrometer scale remains a challenging task in chemical synthesis.[17–21]

Light-driven reactions offer ample opportunities for achieving spatiotemporal control over self-assembly. Methods using such reactions have already demonstrated sub-micrometer spatial resolution and millisecond temporal control in colloidal crystal systems.[22–25] However, practical implementation challenges hinder the extension of these principles to synthetic biorelevant crystallization. The objective of this thesis is to investigate how light can be harnessed to achieve this spatiotemporal control on the nucleation and growth of biorelevant crystals.

In this introduction, we will briefly discuss the fundamental principles and phenomena employed in developing new methodologies that enable spatiotemporal control over crystallization of biorelevant crystals. This includes the phenomena of biominerals and crystallization; methods of controlling crystallization, using calcium carbonate as a model system; the co-precipitation of barium carbonate with silica into nanocomposites; and the developments in light-driven self-assembly. Finally, we give an overview of the subsequent chapters in this thesis.

1.1 Biominerals

The formation of biominerals in nature serves as a striking example that highlights the potential of spatiotemporally controlled crystallization.[5,16,26,27] This section offers a concise overview of their formation process while highlighting the distinctive characteristics that make them exceptional.

Biominerals, naturally found inorganic substances, are meticulously crafted within living organisms through a precise self-assembly process known as biomineralization. Regulated by proteins, this intricate process involves involves nature's adept management of local chemical gradients and biological geometries, orchestrating crystallization processes with precise spatiotemporal control.[7,28,29] For instance, polymeric frameworks and cellular vesicles serve as molds or connectors between inorganic and organic processes to guide the formation of distinct patterns.[26,30] Simultaneously, local environmental factors such as precursor concentration, temperature, and pH intricately regulate the kinetics of chemical reactions, forming the appropriate composition at the correct place and time.[30–37] This delicate interplay of controlled parameters gives rise to intricate morphologies, which significantly depart from the symmetry of crystal lattices, and thereby present unique physicochemical properties. Shells,[38], bones,[39] and teeth[40] exemplify this phenomenon, showcasing resilience, toughness, and strength owing to their distinct combination of composition, external shape, and highly organized atomic arrangement, and highlight the influence of precisely controlled local gradients (Figure 1.1).

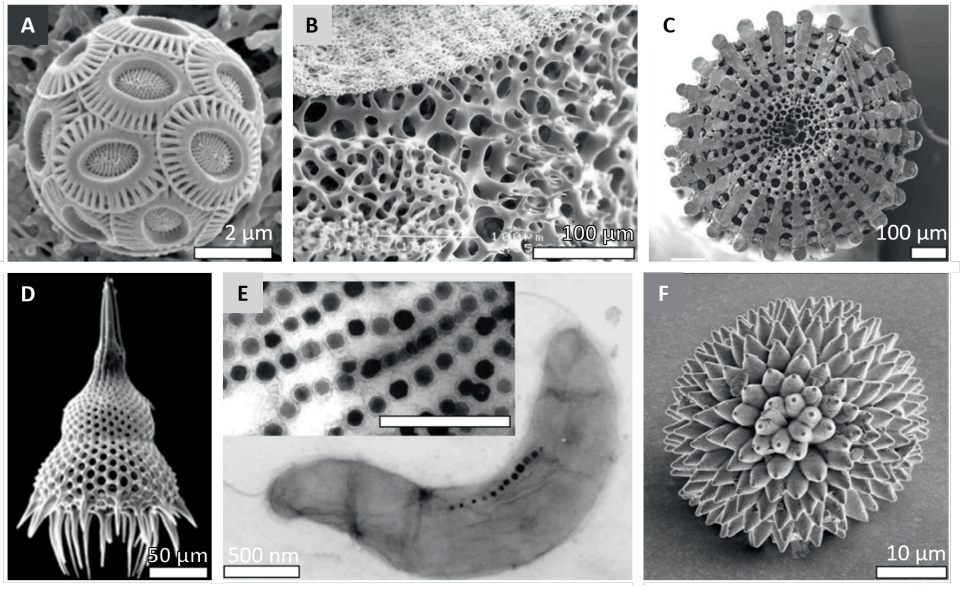

Figure 1.1: Various biominerals found in nature. SEM images of A) a cell wall of coccolithophore species, B) a stereom structure of a sea urchin skeleton, C) a transverse section of the primary spine of a sea urchin, and D) an endoskeleton of a cell of the radiolaria Lamprocyclas martialis. E) Transmission electron microscopy (TEM) image of a single chain of biomagnetite nanocrystals of a cell of Magnetospirillum gryphiswaldense; inset: the isolated biomagnetite nanocrystals. F) SEM image of a microsclere from the demosponge Geodia cydonium. (A-C) are $CaCO_3$-based, (D-F) are SiO_2-based, and (E) is Fe_3O_4-based. Courtesy of (A) J. Young, (B) J. Aizenberg, (C) P. Dubois, (D) J. Dolven, (E) D. Schüler, and (F) I. Zlotnikov. Copied from [10].

1.2 Crystallization

Replicating the spatiotemporal precision of nature's biomineralization demands a fundamental understanding of the principles governing nucleation and growth in crystallization processes. To facilitate this understanding, we will briefly delve into established nucleation theories, their corresponding thermodynamics, and the factors influencing the crystallization process. For the purpose of this discussion, our exploration will be confined to homogeneous nucleation and growth emerging from solutions.

Classical nucleation theory

Crystallization denotes a phase transition characterized by the transformation of initially disordered atoms, ions, or molecules into a systematically arranged and periodic solid structure, recognized as a crystal lattice.[41,42] The underlying mechanism of crystallization is often explained by two closely related fundamental theories: classical nucleation theory[43,44] and non-classical nucleation theory (Figure 1.2).[45,46]

In the classical nucleation theory (CNT), crystallization begins with the formation of a single nucleus, followed by its growth into a crystalline structure.[41] The transformation of dissolved species into a solid crystal is, in principle, a spontaneous process that aims to minimize the total Gibbs free energy of the system.[47] This process is primarily driven by a supersaturated state, a state in which the concentration of species in a solute exceeds the solubility threshold, corresponding with a chemical potential gradient between the two phases that is positive compared to the equilibrium state:

$$\sigma = \ln \frac{a_i}{a_i^{eq}} = \frac{\Delta \mu_i}{k_b T} \tag{1.1}$$

with

$$\Delta \mu_i = \mu_i - \mu_i^{eq} \tag{1.2}$$

and

$$\mu_i = \mu_i^0 + nRT \ln(a_i) \tag{1.3}$$

Where σ is the supersaturation, a_i is the molar concentration of the species i in the solute, a_i^{eq} is equilibrium concentration, k_b is the Boltzmann constant, T is the temperature, n is the number of moles, R is the universal gas constant, μ_i represents the chemical potential of species i in the solute, μ_i^{eq} its equilibrium chemical potential and μ_i^0 its standard potential.

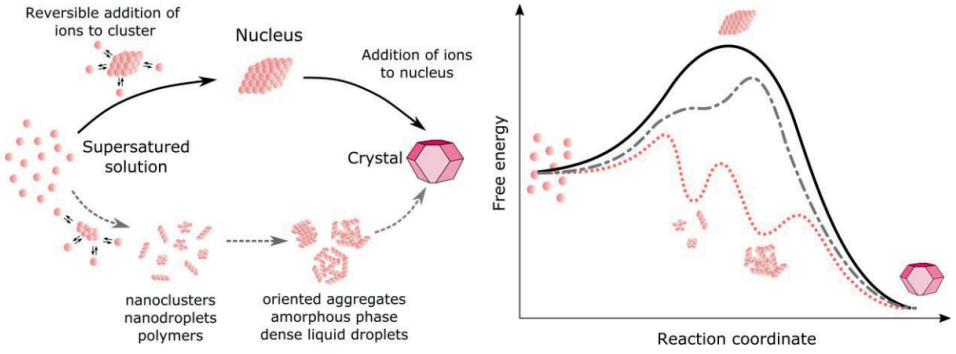

Figure 1.2: Schematic of crystallization processes following classical or non classical nucleation theory. Left, development of the stages of the crystal components with single (classical, solid black line) or with multiple (non-classical, dotted and dashed dotted grey and pink line) steps. Right, the associated free energy of the developing system. The reaction coordinate can be compared with the radius of the (nucleus of the) crystal in the text. Copied from [48].

In a supersaturated state, the means to lower the Gibbs free energy of the system is by generating a volume of solid species (G_v). However, this formation of a thermodynamic new phase requires an activation energy, as the creation of a new interface between the solution and the solid surface area of the nucleus increases interfacial energy (G_s) (Figure 1.2).[49] Therefore, the Gibbs free energy describing the crystallization process (G_{crys}) contains an energetically unfavorable-surface term (G_s), and an energetically favorable volume term (G_v):

$$\Delta G_{crys} = \Delta G_s + \Delta G_v \tag{1.4}$$

with

$$\Delta G_s = 4\pi r^2 \gamma \tag{1.5}$$

and

$$\Delta G_v = -\frac{4}{3}\pi r^3 \frac{\Delta \mu}{V_m} \tag{1.6}$$

Where r is the radius of the aggregation of species that forms a nucleus, γ is the surface tension between the solid and the solute, and V_m is the volume per building unit.

The critical size with r^* of a stable nucleus that can grow into a crystal can be found by setting $\Delta G_{crys}/\delta r = 0$, yielding:

$$r^* = \frac{2\gamma V_m}{\Delta \mu} \tag{1.7}$$

Substituting r^* in G_{crys} provides a measure of the nucleation rate. We find that a larger supersaturation leads to a larger G_v, consequently yielding smaller r^* values, thereby expediting nucleation. Conversely, a higher surface tension creates a higher energy barrier and increases r^*. As a results of this energy barrier, the solution may remain in a metastable state.

Non-classical nucleation theory

Another approach to describe nucleation is the non-classical nucleation theory (NCNT). In the context of NCNT, it is proposed that multiple clusters with sizes falling below the critical nucleation size form first.[50] Clusters can manifest as either crystalline or amorphous particles, progressing through diverse modes of aggregation or attachment to form bulk crystals.[46] Attachment, for instance, can occur along preferred orientations of crystal facets, facilitated by a match in crystal lattices.[51] Ultimately, the clusters that attach in the resultant superstructure have the capacity to reorganize and fuse, culminating in the formation of a single crystal.[46,52] The energy terms of the Gibbs free energy are now described by the multiple aggregation steps involved:

$$G_{crys} = G_{prenuclation} + G_{aggregation} + G_{rearrangement} + G_{crystallization} \tag{1.8}$$

Where every sub G can be described with the sub processes.

While the intermediate steps of crystal formation in the NCNT diverge from the CNT, we find that the same concepts pertaining to energy and driving forces remain applicable. The phase transition process operates through supersaturation and aims to minimize the system's Gibbs free energy. But just as in the CNT, the initial formation of new phases faces an energy barrier due to rising interfacial energy and the subsequent creation of a unified solid crystal leads to a reduction in the overall energy of the system (Figure 1.2).

1.3 $CaCO_3$ as a case study of controlling crystallization

Among the many crystal systems we know, the biorelevant mineral calcium carbonate ($CaCO_3$) is an ideally suited model compound for examining spatiotemporal control over crystallization. $CaCO_3$ has been the subject of thorough investigation, unveiling its underlying mechanisms and exploiting its remarkable capability to generate a diverse array of shapes.[11,53] Furthermore, the compound already demonstrates versatile applications in both natural[54,55] and industrial settings.[56–59] Gaining spatiotemporal control over this system not only advances our understanding of various natural self-assembly processes but also opens innovative pathways for producing novel functional materials. This section delves into the fundamental natural attributes of this compound while highlighting strategic methodologies developed for controlled crystallization.

Natural features of $CaCO_3$

After quartz (crystalline SiO_2), $CaCO_3$ crystals are the second most abundant crystals on earth and belong to the class of alkali earth metal carbonates.[60] $CaCO_3$ is sparingly soluble in water and its solubility increases with increasing pressure and pH, and with decreasing temperature. $CaCO_3$ appears in three main crystal forms (named polymorphs) : calcite (rhombohedral), aragonite (hexagonal), and vaterite (orthorombic) (Figure 1.3).[61] Its crystalline form is often preceded by an amorphous phase called amorphous calcium carbonate (ACC), which is thermally highly unstable but easily formed kinetically and, therefore, often used as a precursor.[62]

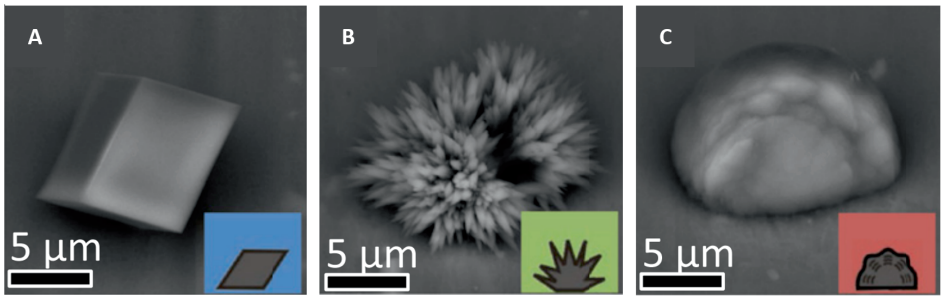

Figure 1.3: Synthesized $CaCO_3$ with different polymorphism. SEM images of A) calcite, B) aragonite, and C) vaterite with rhombohedral, hexagonal, and orthorhombic geometrical unit cells, respectively. Copied from [63]

$CaCO_3$ readily interacts with organic macromolecules, forming composites that greatly expand the variety of $CaCO_3$ architectures and their associated properties.[55] Therefore, many organisms use $CaCO_3$ as a building block to create highly functional biominerals that fulfill essential functions for survival. For instance, the alignment and optical properties of calcite crystals in the skeleton of brittle stars enable the regulation of photosensory phenomena.[4] While layered aragonite crystals of $CaCO_3$ within nacre, bonded together by complementary organic materials, offer robustness and durability, providing protective strength and hardness (Figure 1.4).[64]

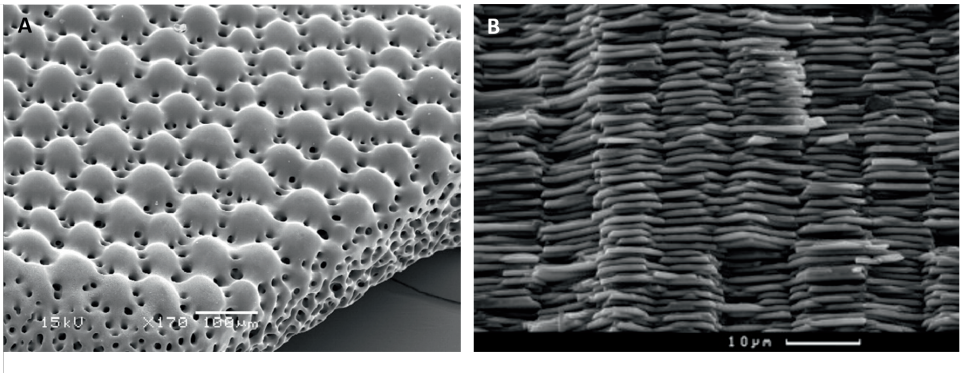

Figure 1.4: Natural shapes of $CaCO_3$. SEM images of A) a part of the skeleton of the brittlestar Ophiocoma wendtii (Ophioroidea, Echinodermata), and B) a microstructure of nacre from the seawater snail Haliotis laevigata. Copied from (A) [65] and (B) [64].

Synthetic routes of controlled $CaCO_3$ crystallization

In laboratory settings, strategic methods for guiding $CaCO_3$ draw inspiration from nature's ability to orchestrate localized gradients, relying on the fundamental principles of nucleation. Typically, this exploration begins with a close examination of natural processes, whereafter newfound insights are reformulated for synthetic methods.[11,29] We can categorize these methods of controlled $CaCO_3$ crystallization into three main themes: 1) manipulation of thermodynamics through soluble additives, 2) templating by insoluble additives and 3) indirect adjustment by leveraging external environmental factors (Figure 1.5).

Using soluble additives, common strategies are based on high salinity and enzymatically active environments that influence the (pre)nucleation and growth behavior of $CaCO_3$.[17,30] The additional interactions of the additives with the solute can influence nucleation and growth stability, as well as kinetic rates both before and during the process. For instance modifications with entropic, steric, or energetic effect, enhance the nucleation and growth of a specific polymorph.[66] The inhibition of a growth face due to selective adsorption directs the final crystal habit.[67,68] Moreover, chiral acidic amino acids have been demonstrated to induce chiral hierarchical vaterite structures (Figure 1.5 A).[69]

Methods that use insoluble additives are inspired by stereochemical recognition and electrostatic matching found.[29] In nature, this can involve large biomolecules with functional groups forming templates that direct nucleation and growth.[70,71] These functional groups may vary in terms of charge density, acidity, or polarity.[72] A synthetic adaptation of this approach involves patterning self-assembled monolayers (SAM) on metal films.[73] The functional terminal groups within these monolayers enable the direction of local nucleus aggregation, resulting in spatial distribution and orientation of crystallographic planes within the SAM (Figure 1.5 B).

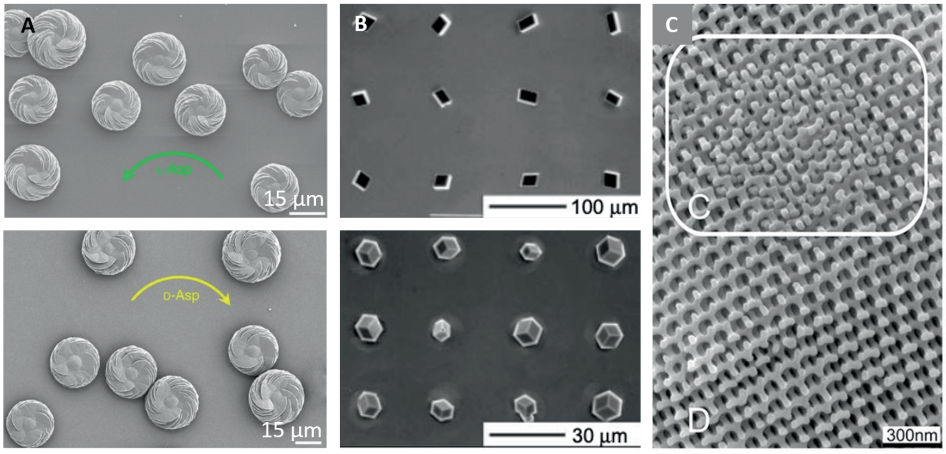

Figure 1.5: Result of different modification strategies to direct $CaCO_3$ growth. SEM images of A) vaterite grown in L- or D-Asp yielding chiral toroids spiral in the counterclockwise direction (green arrow, top image) or clockwise direction (yellow arrow, bottom image), respectively. B) Ordered two-dimensional arrays of single calcite crystals controlled by the micropatterned SAMs (top image regions of $HS(CH_2)_{22}OH$ on Au, and bottom image regions of $HS(CH_2)_{11}SO_3H$ on Pd). C) Example of the replication of the full double $CaCO_3$ gyroid (a region with double networks is marked by C and a single network region is marked by D). Copied from (A) [69], (B) [73], and (C) [74].

The last category concerns the architectural environment of biomineralization. In nature, the crystallization process is often regulated in tight volumes or confinements, as seen in viruses and hollow capsules.[75] Synthetic microfabrication techniques yield what are known as "crystal hotels" and defined nano-sized molds,[76] in which several strategies can be employed to direct crystallization. For instance, by stabilizing the amorphous precursor phase in the confined space, these systems enable the production of large single calcite crystals with predefined crystallographic orientation,[77] which can even be leveraged to create gyroid morphologies (Figure 1.5 C).

Expanding on these approaches, further developments in biomineralization control can be found in numerous studies that applied combinations of methods. Examples include high-pressure environments with additive control to direct the size, morphology, and orientation of $CaCO_3$ crystals,[78] or polymer-mediated growth with a layer-by-layer deposition of organic films to mimic nacre-like materials.[79]

The control and understanding of $CaCO_3$ systems have undeniably made significant progress and precise control over nucleation is attainable concerning location, orientation, and 2D and 3D morphology, even with the potential for achieving single or multiple crystallinity. However, despite the successful implementation of many strategies, control remains constrained by either a global and dynamic or a local and static effect. As a result, achieving spatiotemporal control in these synthetic systems continues to be challenging and necessitates the development of new principles.

1.4 MCO_3/SiO_2 architectures

One of the few inorganic mineralization systems that can grow complex shapes extending beyond their crystallographic symmetries is the synthetic co-precipitation of nanocrystalline earth alkali metal carbonates (MCO_3, with M= Ba^{2+}, Sr^{2+}, Ca^{2+}) with amorphous silica (MCO_3/SiO_2).[80,81] This system produces micrometer-sized architectures with shapes ranging from coral, vase, and stem-like forms to helices and leaf-like sheets[82,83] (Figure 1.6). These structures exhibit optical properties such as waveguiding and polarization, and they can be further transformed in composition through shape-preserving ion exchange reactions, enriching the system with a variety of functional compositions.[84–86] Gaining spatiotemporal control over this system has the potential to enhance our understanding of the underlying principles of self-assembly mechanisms in nature and can open new pathways to functional materials. In this section, we will discuss the general synthesis, strategies for manipulation, and their applications.

General Synthesis of MCO_3/SiO_2 architectures

The MCO_3/SiO_2 architectures are polycrystalline nanocomposites consisting of aligned elongated orthorhombic MCO_3 nanocrystals (60-90% atomic weight) embedded in a silica matrix (10-40% atomic weight).[87] They were discovered by Garcia-Ruiz in the 1970s, who called them biomorphs due to their life-like shapes. Their hierarchical order is believed to form through the activation and inhibition of MCO_3 and silica formation in an acid-regulated feedback loop, far from thermodynamic equilibrium.[88,89] This loop begins with the formation of crystalline MCO_3, typically due to the diffusion of CO_2 from the air in an alkaline aqueous medium containing MCl_2 (5-50 mM) and Na_2SiO_3 (7-11 mM). Subsequently, the released protons in this reaction activate silica formation, inhibiting further growth of the MCO_3 but simultaneously inducing the new formation of MCO_3 nanocrystals:

$$M^{2+} + CO_2 + H_2O \rightleftharpoons MCO_3 + 2\,H^+ \tag{1.9}$$

$$SiO_3^{2-} + 2\,H^+ \rightleftharpoons SiO_2 + H_2O \tag{1.10}$$

The newly formed MCO_3 crystals align with the *c*-axis of the already grown crystals, further assembling into life-like shaped architectures.

This co-precipitation is highly sensitive to the reaction conditions and requires the precipitation of both components in the right ratio. A change in the reaction conditions quickly results in a different morphology. So far, we can identify two main growth modes based on pH:[83] one at high pH (around 11-12), favoring MCO_3 over silica precipitation, where the active growth front of the architectures expands outwards toward the bulk, yielding coral-vases and stem-like structures. The second mode, at lower pH (between 10-11), enhances silica solubility over MCO_3, resulting in the growth front moving away from the bulk and producing spiraling single or double helical-shaped structures. A third growth regime could be defined, where silica does not precipitate, but only $BaCO_3$ crystals form, highlighting the crucial role of silica.

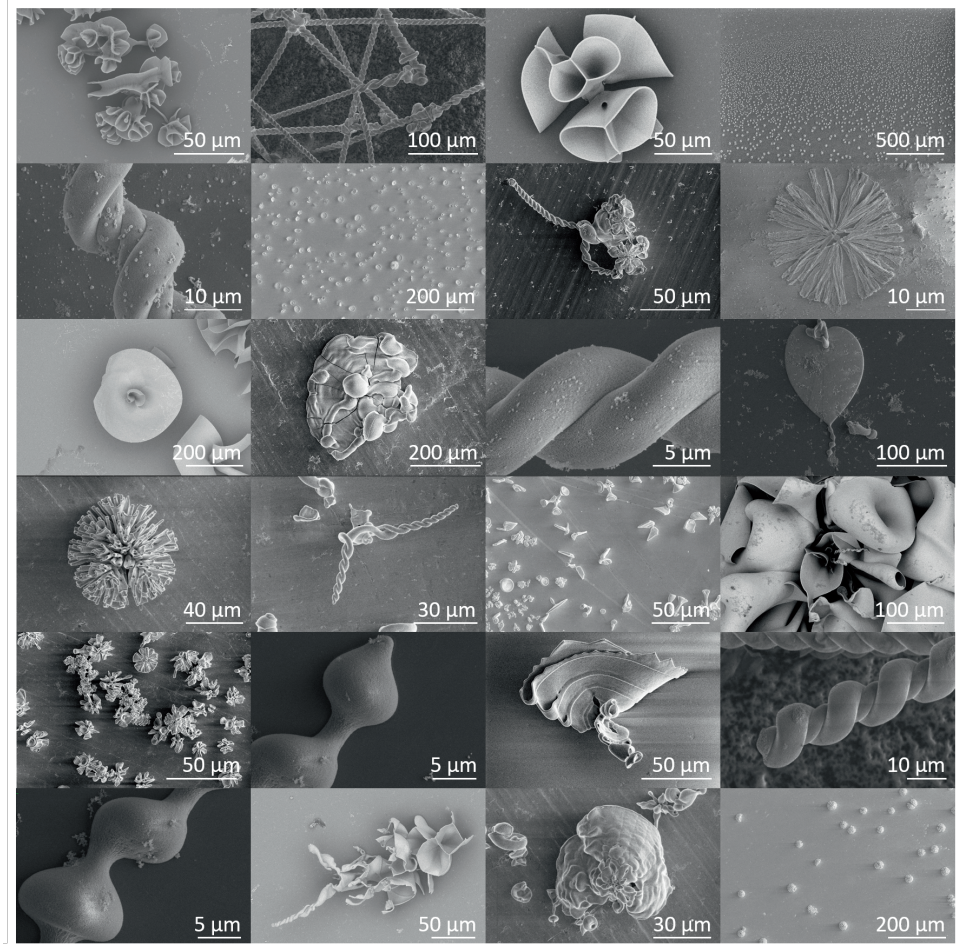

Figure 1.6: Overview of MCO_3 / SiO_2 architectures grown at various crystallization conditions.

Strategies for shape modifications

To gain a deeper understanding and a better control over this system, various strategies have been developed to modify the co-precipitation. Most of these strategies involve global variations in the growth conditions, such as changes in pH,[83] precursor concentrations,[81,90] CO_2 influx,[83] additives,[91] and temperature.[92] These alterations in the synthesis parameters influence the precipitation rates and, consequently, the morphology of the resulting structures. For example, introducing a temporary influx of CO_2 leads to the thickening of the growing structure (Figure 1.7 A), an initial high Ba^{2+} concentration yields highly bifurcated floral shaped structures (Figure 1.7 B), a higher temperatures result in the formation of thinner, rapidly growing trumpet-like structures (Figure 1.7 C), and an addition of additives, such as metal ions doping, has been found to suppress growth (Figure 1.7 D).

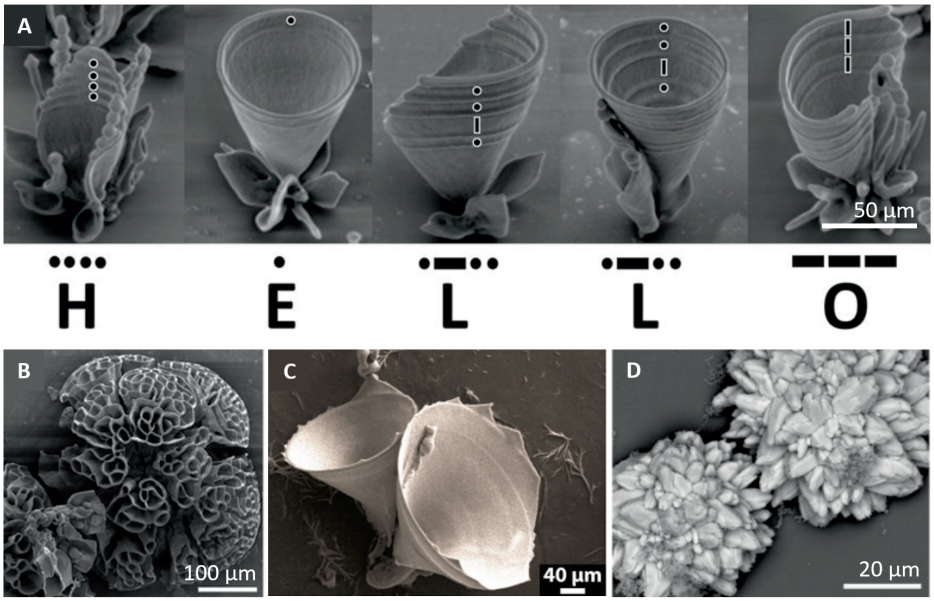

Figure 1.7: Results of modified growth conditions to manipulate the $BaCO_3/SiO_2$ structure's morphology. SEM images of structures grown with A) temporary influx of CO_2, B) high concentrations of Ba^{2+} (500 mM $BaCl_2$), C) high temperature (45°C), and D) doped with Ca^{2+} (0.5 mM). Copied from (A) [83], (B) [81], (C) [92], and (D) [91].

In contrast, local adjustments to the growth conditions have been explored to a lesser extent. In this context, variations in the growth substrate are the main focus. Here, we find methods that influence the position of nucleation through surface confinements such as trenches,[93] substrate patterning with photoresist,[94] and topographical adjustments using top-down lithography.[95]

Functionalization of MCO_3/SiO_2 architectures

To enhance the functionality of these structures, studies have primarily focused on modifying their composition (Figure 1.8). There are two main strategies employed: the 'build-in' principle[96–99] and the

use of shape-preserving ion-exchange reactions.[84,86,100,101] In the 'build-in' principle, the original MCO_3 nanorods remain intact but are enhanced with additional groups during or after the growth process by adjusting the silica content (Figure 1.8 A, B). For example, one approach involves incorporating a pH-sensitive dye, enabling the analysis of pH-dependent feedback loops.[97] In another study, researchers demonstrated the incorporation of light-switchable spiropyran derivatives to create a magnetized biomorphic microcarrier system.[98]

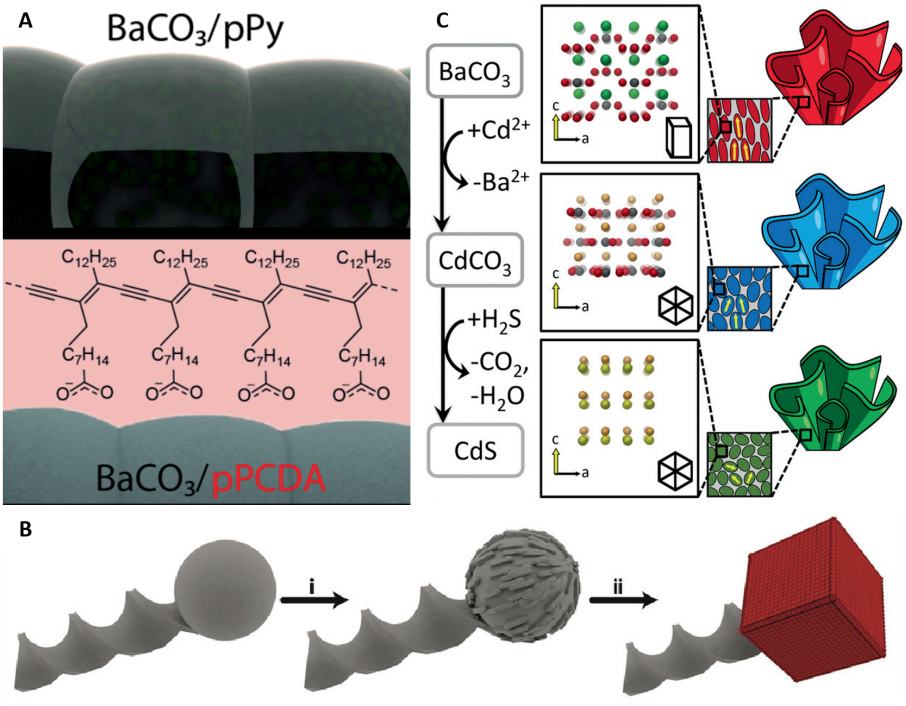

Figure 1.8: Functionalization methods of the $BaCO_3/SiO_2$ structures. Schematic and light microscope image of A) the 'build-in' principle, B) post surface modification, and C) ion exchange reaction conversion. Copied from (A) [99], (B) [96], (C) [86].

Conversely, ion exchange reactions involve a complete conversion of the chemical composition (Figure 1.8 C). Effectively replacing the $BaCO_3$ nanocrystals introduces additional properties to the structure. In this approach, the competitive reactivity of ions facilitates the exchange of composition, while the silica matrix helps maintain the original shape.[84] A notable example include the conversion of $BaCO_3/SiO_2$ coral-like architectures into catalytic Co_3O_4/SiO_2 structures,[100] which even exhibited improved performance in terms of selectivity and activity compared to conventional catalysts. Other postfunctionalizations with ion conversion of these architectures yield optoelectronic semiconducting perovskite,[84] various catalytic compositions and magnetic and electronic functionalized materials.[86,101]

The MCO_3/SiO_2 co-precipitation can thus be tailored in terms of shape and composition while maintaining the hierarchic complexity inherent in self-assembly. Combining this with their intrinsic optical properties, the system offers an exciting opportunity to explore the fabrication of photodirectable structures that can be chemically modified post-assembly. However, realizing this potential requires dynamic and localized control of chemical gradients, as opposed to the current static and global methods. Such approach with spatiotemporal control will enable precise guidance for both nucleation and growth, facilitating the assembly of materials based on user-defined designs.

1.5 Light-controlled self-assembly

Precise dynamic control over local environments is crucial for steering the nucleation and growth of crystals according to user-defined designs with new functionalities. External stimuli that are precisely tunable in space and time offer the potential to gain such dynamic control. Especially light is a promising and effective tool, because it is clean, precise, and versatile.[22,23,102–104] Furthermore, the remote and on demand tunability in intensity and wavelength enables to selectively target a process in a non-invasive manner. In this section we discuss how photochemical and laser-based methods are used and developed for self-assembly systems and how this is currently implemented for biorelevant crystals.

Photochemically driven self-assembly

A photochemical reaction is a chemical reaction that is initiated or driven by the absorption of photons.[105] These reactions involve the excitation of molecules or atoms from their ground state to higher energy states when they absorb photons with resonating energy. The excited species formed during this process can undergo various chemical transformations, leading, for instance, to changes in acidity,[106] polarity,[107] isomerization,[108] or even the loss of functional groups,[109] thereby selectively enabling chemical reactions in the excited state.

To utilize photochemical reactions to direct self-assembly systems, it is necessary for the system to exhibit photosensitivity. In non-photoresponsive self-assembly systems, photosensitivity can be introduced by attaching photo-responsive molecules as functional ligands to the self-assembling components (Figure 1.9).[23,103] Commonly used molecules with efficient photosensitivity include diarylethene-based imines,[110] azobenzene derivatives,[111] and spirospiran species,[112] whose excitation energy corresponds to (deep) ultraviolet (UV) light. For example, azobenzene photoswitches are used in colloidal crystals, where the photosensitive molecules are attached to nanoparticles.[113] When these systems are irradiated with light, it induces colloidal aggregation or repulsion, resulting in the formation of organized superstructures. Another instance of light-induced superstructure organization is seen in the photoconfigurational changes of spiropyran-based molecules.[114] In this case, illumination triggers photodimerization, causing a dimer to form between two nanoparticles. Furthermore, in liquid crystal systems, the attachment of photoswitchable ligands has been shown to enable switching between different crystal phases.[115]

Alternatively, photochemistry can also be employed indirectly. In this case, the environment responds to light irradiation, and the self-assembling components respond to the photochemically changed environment. A clear example is a photoswitchable host-guest inclusion complex of an azobenzene derivative by cyclodextrins. Here the photoisomerization of azobenzene derivatives in combination with the binding affinity of cyclodextrin controls light-responsive aggregation and dispersion behavior of nanoparticles.[116] Another example is the deprotonation of nanoparticle-bound ligands. In this scenario, pH-sensitive ligands can be activated by photo-acids or bases that change acidity in the excited state.[22,117]

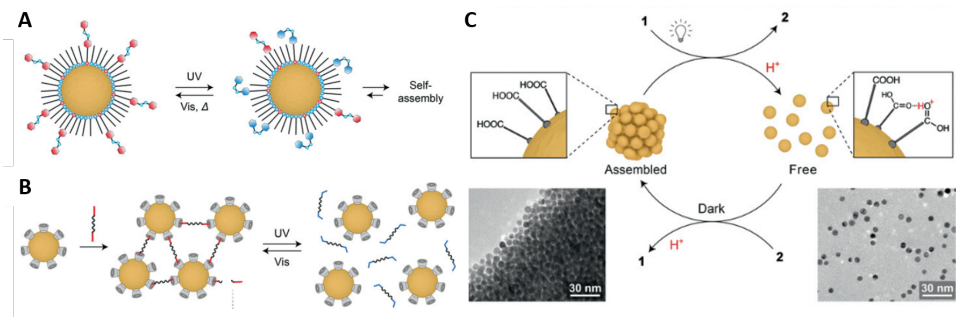

Figure 1.9: Light-induced organization of colloidal superstructures. Schematics of using A) photoisomerization with azobene derivate, and B) photoswitchable host-guest inclusion complex with azobenzene and cyclodextrins. Schematic and SEM images of C) (de)protonation of nanoparticle-bound ligands using photoacids. Images copied from [23], which reproduced them from (A) [113], (B) [116], and (C) [22].

Light-induced nucleation and growth of biorelevant mineralization

Light-directed crystallization of biorelevant minerals holds the potential to deepen our understanding of complex self-assembly processes and simultaneously offer a new pathway for creating innovative materials with advanced functionalities. However, research on light-induced nucleation and growth of biorelevant mineral crystals, utilizing photochemistry to achieve precise spatiotemporal control over the process, remains limited at present.

There are several reasons why this field is relatively unexplored.[118] Most of all, the direct implementation of photochemistry in aqueous solutions is challenging as most developments have been focused on aromatic compounds, which have limited water solubility,[119,120] restricting the available options or necessitating extensive modifications that may compromise their efficiency. Moreover, biorelevant mineral crystal building blocks are mostly not photosensitive and attaching photosensitive compounds is challenging, thereby hindering the application of direct use of photoreactive compounds. Furthermore, pure mineral growth exhibits a high sensitivity to the surrounding environment. Therefore, photoreactive compounds could easily disrupt the crystallization process.[26,30,121]

An example of a study that demonstrates the initial steps in light-induced mineral crystallization with photochemistry involves the use of a photobase to raise the pH of the growth solution.[122] In this case, the photobase Malachite green carbinol base (MGCb) is used, that releases a hydroxide ion in its excited state. Using this principle, the work demonstrates the formation of $CaCO_3$ and ZnO-films upon bulk

irradiation of UV light.

Laser induced crystallization

Besides photochemical, the use of light to initiate crystallization systems is also explored to be used in a non-photochemical manner.[25,123,124] These processes involve light, primarily utilizing a laser source, but they differ from traditional photochemical reactions since the light is not strongly absorbed by the solute or solvent to initiate a chemical change (Figure 1.10). A rudimentary classification of these studies distinguish three main categories.[25] 1) Optical laser trapped crystallization, where continuous lasers are used to create local supersaturation due to electromagnetic interactions.[125,126] 2) High intensity laser induced crystallization, where femtosecond pulsed lasers are employed, reaching energy densities high enough to generate an optical breakdown, plasma formation, vaporization, or melting.[127] triggering rearrangement and nucleation.[128,129] And lastly 3) non photochemical laser induced nucleation, where the peak intensity of unfocused laser pulses appears to locally enhance the nucleation probability.[123,130,131]

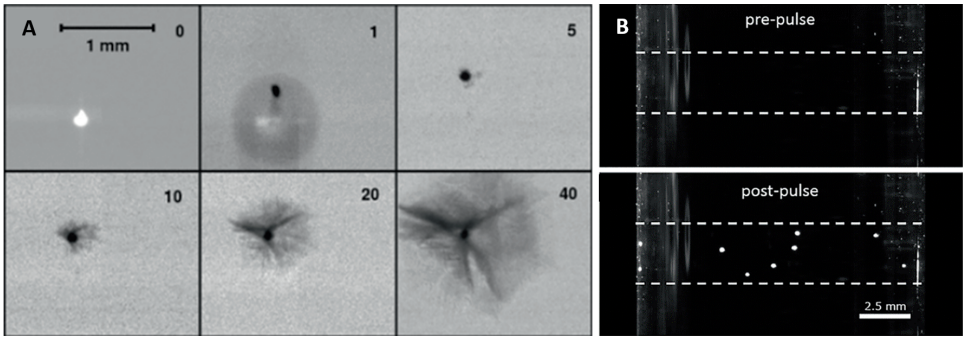

Figure 1.10: Non-Photochemical Laser Induced Crystallization. Light microscope images of A) ice with 8 ns laser irradiation inducing optical breakdown (the energy at the focus spot is 2 mJ), and B) NH_4Cl with single 1064 nm laser pulse in an unfiltered solution (top before and bottom approximately 1.6 s after). Copied from (A) [129], and (B) [131].

Although laser-induced methods have been demonstrated for a variety of compounds, including metal halides (KCl, KBr), small organics (urea, glycine), and macromolecules (lysozymes),[25] the underlying principles remain unclear, the control achieved typically has a resolution above the micrometer scale, and the methods often rely on advanced laser setups.[124] These challenges make it difficult to extend these techniques systematically to the unexplored field of biorelevant minerals.[25,130]

Harnessing light for controlling biorelevant crystallization holds promise. Yet, while efforts are being made in creating water-soluble photoreactive compounds and instances of crystallization induced by lasers are increasingly emerging, a deeper understanding and the formulation of novel principles are essential to effectively apply this approach in the domain of biorelevant minerals.

1.6 In this thesis

Controlling self-assembly processes presents a fundamental scientific challenge with practical implications for the development of next-generation advanced materials. Such control has the potential to revolutionize materials design, allowing for autonomous assembly when possible and precise manual intervention when necessary. Among the various strategies developed for achieving control over crystallization, light-induced crystallization, whether non-photochemical or photochemical, stands out as a promising method. The following chapters explore new approaches where light is employed to achieve spatiotemporal control over self-assembly of biorelevant crystals, focusing primarily on the versatile nanocomposites ($BaCO_3/SiO_2$) and abundant biorelevant minerals.

Chapter 2: We investigate a photochemical approach for gaining local and dynamic control over the reaction conditions of the self-assembling $BaCO_3/SiO_2$ nanocomposites. By utilizing a custom-built optical setup, carbonate is generated photochemically using ultraviolet light patterns to influence the precipitation of $BaCO_3/SiO_2$ nanocomposites in situ. The study explores how photogenerated precursors, crystallization processes, and diffusion mechanisms can be exploited for dynamic and localized control over chemical gradients. These insights allow for three levels of control: (1) positioning individual and large fields of composites, (2) sculpting the composites' contours, and (3) dynamically steering self-assembly by synchronizing the light spot's movement.

Chapter 3: We further delve into the principle of using locally generated carbonate gradients through photochemistry to direct the co-precipitation of $BaCO_3/SiO_2$ nanocomposites. We investigate whether modulating the UV light intensity to create local carbonate gradients can influence different growth modes and patterns, providing a deeper understanding of morphological development. The research shows that subtle modulations in UV light intensity can guide the morphological development of the $BaCO_3/SiO_2$ nanocomposites, demonstrating three levels of control: (1) switching between growth modes to form different structures, (2) dynamically transitioning between growth modes within a single structure, and (3) refining sculpting within a single growth mode.

Chapter 4: We propose a new strategy for sculpting different chemical compositions into complex user-defined architectures. We develop a hybrid approach that combines subsequent light-controlled self-assembly of $BaCO_3/SiO_2$ architectures with post-process complementary ion conversion enabling the integration of different compositions with assigned locations while preserving shape. This control is leveraged in three ways: (1) conversion of light-patterned and contoured architectures, (2) positioning architectures with different compositions next to each other, and (3) integrating different compositions into a single architecture.

Chapter 5: We introduce the use of resonant near-infrared (NIR) laser heating to induce the crystallization of pure biorelevant minerals with precise spatiotemporal control, without the need for special crystallization media or additives. NIR light is shown to enable extremely fast (millisecond) local heating of water, promising precise spatiotemporal control over the crystallization of retrograde soluble minerals. By modulating NIR light intensity, the research demonstrates control over various aspects: (1) laser drawing of MCO_3 crystals with micrometer resolution, (2) positioning single $CaCO_3$ crystals

with specific polymorphisms next to each other, and (3) extending the general principle to enable the growth of Ba-Sr-$CaCO_3$ crystals next to each other, as well as single crystals of calcium phosphate and strontium sulfate.

Chapter 6: We explore the potential of two-photon absorption in governing nucleation and growth processes with precise three-dimensional spatial control. Two-photon absorption, being a non-linear process, requires an exceptionally high peak intensity. This unique demand allows the phenomenon to selectively occur within the focal spot of a laser. We investigate the feasibility of inducing photodecarboxylation of ketoprofen within a micron-sized focal spot using a ps-pulsed 532 nm laser setup. We systematically screen chemical parameters to optimize the precipitation into $BaCO_3/SiO_2$ nanocomposites. We leverage our insights to achieve precipitation at micrometer resolution and controlled *z*-directional growth from an *x,y*-plane. Additionally, we demonstrate the feasibility of ion exchange conversion for the precipitation and discuss further steps necessary to enhance and refine this pioneering principle.

Chapter 7: We comprehensively reflect on our research endeavors, including a brief description of discontinued projects. We briefly encompass the technical and chemical requirements to implement light into biorelevant crystallization systems. Our culmination lies in a conclusive summary, gathering insights gained throughout the research process and give thought to the significance of this work. Moreover, we venture into the future, providing recommendations for potential new research avenues where our methods could prove instrumental.

Chapter 2

Light-controlled nucleation and shaping of self-assembling nanocomposites

Abstract

Controlling self-assembly of nanocomposites is a fundamental challenge with exciting implications for next-generation advanced functional materials. Precursors for composites can be generated photochemically, but limited insight in the underlying processes has hindered precise hands-on guidance. In this study, light-controlled nucleation and growth is demonstrated for self-assembling composites according to precise user-defined designs. Carbonate is generated photochemically with UV light to steer the precipitation of nanocomposites of barium carbonate nanocrystals and amorphous silica ($BaCO_3/SiO_2$). Using a custom-built optical setup, the self-assembly process is controlled by optimizing the photogeneration, diffusion, reaction, and precipitation of the carbonate species, using the radius and intensity of the UV-light irradiated area and reaction temperature. Exploiting this control, nucleation is induced and the contours and individual features of the growing composite are sculpted according to micrometer-defined light patterns. Moreover, moving light patterns are exploited to create a constant carbonate concentration at the growth front to draw lines of nanocomposites with constant width over millimeters with micrometer precision. Light-directed generation of local gradients opens previously unimaginable opportunities for guiding self-assembly into functional materials.

This chapter is based on Bistervels, M. H., Kamp, M., Schoenmaker, H., Brouwer, A. M., & Noorduin, W. L. (2022). Light-Controlled Nucleation and Shaping of Self-Assembling Nanocomposites. *Advanced Materials*, 34 (5), 2107843.

2.1 Introduction

Precise control over biotic and abiotic self-assembly processes is of fundamental interest with practical impact for simple and scalable routes toward complex 3D architectures with advanced functionalities.[18,21,23,38,132–135] A simple and highly versatile bioinspired self-assembly process is the co-precipitation of barium carbonate nanocrystals and amorphous silica into nanocomposites ($BaCO_3/SiO_2$).[80–83,87] In short, carbonate ions trigger the precipitation of $BaCO_3$, which in turn causes the polymerization of SiO_2in an acid-regulated feedback loop. This co-precipitation can yield a wide diversity of 3D shapes such as corals, vases, and helices. Already, post-synthesis functionalization and ion-exchange reactions of such architectures have enabled shape-preserving conversion into chemical compositions with photovoltaic, magnetic, and catalytic performance.[84,86,99–101,122,136,137] Moreover, rudimental patterning and shaping of these composites has been demonstrated by modulating the reaction conditions either dynamically and globally, or statically and locally, leading to similar shapes, but not yet following exact user-defined designs. Unlocking the full potential of this self-assembly approach will require the ability to control chemical gradients both dynamically and locally—instead of statically and globally—for precisely guiding both nucleation and growth to guide assembly according to user-defined designs.

From this perspective, photochemical reactions offer attractive possibilities for modulating local gradients.[23,122,138] Specifically, the photochemical generation of carbonate via photodecarboxylation of ketoprofen (KP) can onset precipitation of $BaCO_3/SiO_2$ composites,[138] but precise control over nucleation and growth, let alone assembly according to user-defined designs, is not possible yet. In particular, it remains unclear how the intricate interplay between photogenerated precursors, crystallization, reaction, and diffusion processes affect self-assembly.

Based on fundamental insights in the roles of reaction and diffusion rates, we here study the spatiotemporal photogeneration of carbonate for light-controlled nucleation and growth of $BaCO_3/SiO_2$ composites. By controlling reaction temperature, light intensity, and other crystallization conditions such as surface free energies, we position single composites in preassigned locations, sculpt fine details and contours, and command the assembly of lines over millimeters with micrometer precision, thus introducing assembly with unprecedented spatiotemporal control.

2.2 Results and discussion

To demonstrate the concept, we develop a custom-built optical setup that enables motorized spatiotemporally controlled irradiation with UV light and in situ monitoring of the process (Experimental Section 2.4, Figure 2.1). From the topside of the setup, user-defined UV patterns are generated, while from the bottom side the process is monitored in real-time using optical microscopy. Inside the setup, a temperature-controlled quartz-covered reaction cell is placed containing a precursor solution of 20 mM$BaCl_2$, 9 mM Na_2SiO_3, and 2–10 mM KP (Figure 2.1). The surfactant dodecyltrimethylammonium bromide (DTAB) (20–100 mm) is added to the precursor solution to mitigate the undesired precipitation of the water-insoluble benzophenone-like photoproduct.[139]

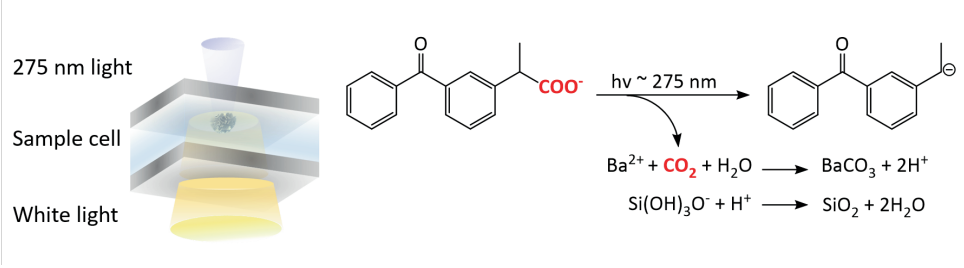

Figure 2.1: Concept of light-controlled generation of local gradients. Photodecarboxylation of ketoprofen (KP) drives the co-precipitation of $BaCO_3/SiO_2$ nanocomposites. To illustrate the concept, the proportions of the generic nanocomposite are enlarged compared to the representation of the sample cell and UV irradiated area.

We screen how the light intensity and radius of irradiation area—and thereby the generation of carbonate—determine the nucleation rate of $BaCO_3/SiO_2$. We irradiate the reaction cell with a conventional UV light of 275 nm to facilitate rapid photodecarboxylation with high quantum yield, while limiting the penetration depth due to the high absorbance coefficient of KP at 275 nm for high spatial resolution in the third dimension.[139] For high light intensity (100 µW mm^{-2}) with a spot size of 250 µm radius, we observe the first nucleation of $BaCO_3/SiO_2$ composites on the quartz cover, which acts as a substrate, within 10 s (Figure 2.2). Upon further irradiation, nucleation continues but at a diminishing rate, as carbonate is also consumed in the growth of the already-nucleated composites. For intermediate light intensity (50 µW mm^{-2}), carbonate is generated at a slower pace, delaying the onset of the first nucleation to 15 s. Nevertheless, we observe a similar trend of nucleation and growth behavior, albeit slower. For even lower light intensity (20 µW mm^{-2}), the onset of nucleation only starts at 45 s, after which almost no additional nucleation is observed. These results show that higher light intensities result in higher rates of nucleation, which can be explained by the increased rate of photodecarboxylation of KP. Therefore, the nucleation rate can be controlled by the light intensity.

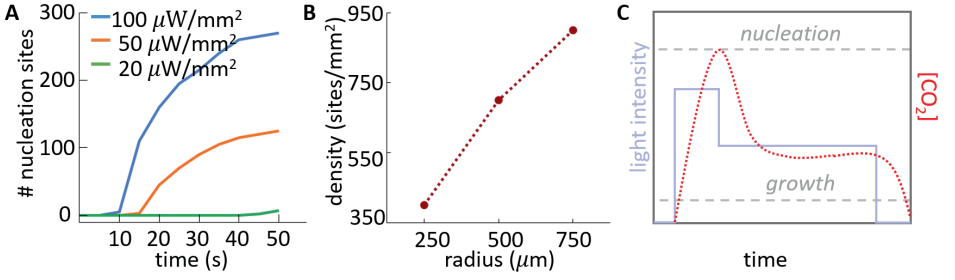

Figure 2.2: Screening of nucleation rate upon light irradiation. A) Number of nucleation sites as function of time for different light intensities confirming that the nucleation rate is proportional to the light intensity. B) Nucleation density at t= 25 s increases as a function of the irradiated area for radii of 250–750 µm at constant light intensity (100 µW mm^{-2}), suggesting slower accumulation of carbonate for smaller irradiated areas. The dashed line is given as a guide to the eye. C) Schematic for modulation of the UV light intensity enables separation of nucleation and growth.

The time-dependent local carbonate concentration is also influenced by the size of the irradiated area. For larger irradiation areas not only more carbonate is generated in total, but we also realize that

the loss of carbonate, due to diffusion away from the light spot, becomes less pronounced. Indeed, increasing the spot size results in a higher nucleation density (Figure 2.2 B). From this result, we can deduce that smaller irradiation areas will require a higher light intensity to locally achieve a sufficient carbonate concentration to induce nucleation. Therefore, tuning both the UV light intensity and the irradiation area provide direct control over local carbonate concentration to induce nucleation and growth of $BaCO_3/SiO_2$ composites.

We exploit the freedom to control the irradiation area and light intensity to separately control nucleation and growth of self-assembling composites. Specifically, we apply high intensity light pulses that kickstart controlled nucleation, followed by more lengthy low intensity lighting that controls growth out of these nuclei (Figure 2.2 C). To demonstrate the principle, we leverage these insights to achieve the following levels of light-controlled self-assembly: 1) spatial positioning of individual composites, 2) contouring and sculpting of individual composites, and 3) dynamic steering.

To demonstrate 1) light-controlled nucleation and growth, we aim to nucleate a single coral-shaped composite in the irradiated area using single light spots. We initially focus a rather large UV light spot (500 µm radius) on the substrate and use low light intensity (5 µW mm^{-2}) to probe the intensity that is needed to induce nucleation at a slow nucleation rate (Figure 2.3). No nucleation occurs within 15 min, indicating there is not enough carbonate generated to induce nucleation. When we increase the light intensity (10 µW mm^{-2}), we observe nucleation of the first $BaCO_3/SiO_2$ composite in the UV-irradiated area within a minute. To prevent new nucleation but still allow growth, we directly reduce the local carbonate generation below the threshold of nucleation by reducing the UV light intensity back to 5 µW mm^{-2} and continue growth for 90 min before stopping the experiment (Figure 2.3 and appendix A Movie 1). Subsequently, scanning electron microscopy (SEM) confirms the formation of a single coral shaped composite inside the reactor, demonstrating that real-time dynamic light-controlled photodecarboxylation enables nucleation and growth of a single composite inside a well-defined irradiated area.

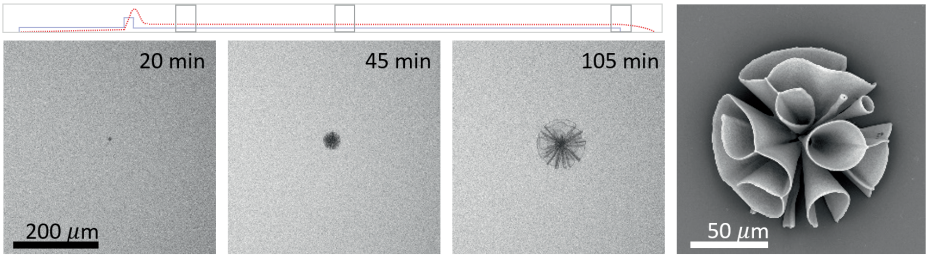

Figure 2.3: Light-controlled nucleation and growth. Optical microscopy time-laps series and SEM micrograph of the resulting single $BaCO_3/SiO_2$ coral-shaped composite by dynamically modulating the light intensity between a nucleation and growth regime, as indicated in the schematic above. Grey squares indicate the moments in time of the given time-lapse series.

Our local control over nucleation and growth can be exploited for successively positioning different composites next to each other with micrometer spatial control. To show our spatial control of local growth, we position a helix and a coral-shaped composite together. First, we decrease the radius of the

light spot to 150 µm to improve the spatial resolution. We compensate for a smaller irradiation area by increasing the light intensity for 30 s to 100 µW mm^{-2} to generate sufficient carbonate for rapid nucleation. Subsequently, we dim the light intensity to 10 µW mm^{-2} for 190 min to maintain growth. Using a precursor solution adjusted to pH 10.8, this procedure enables us to induce the formation of a single helical-shaped structure positioned in the irradiated area (Figure 2.4 A and appendix A Movie 1).

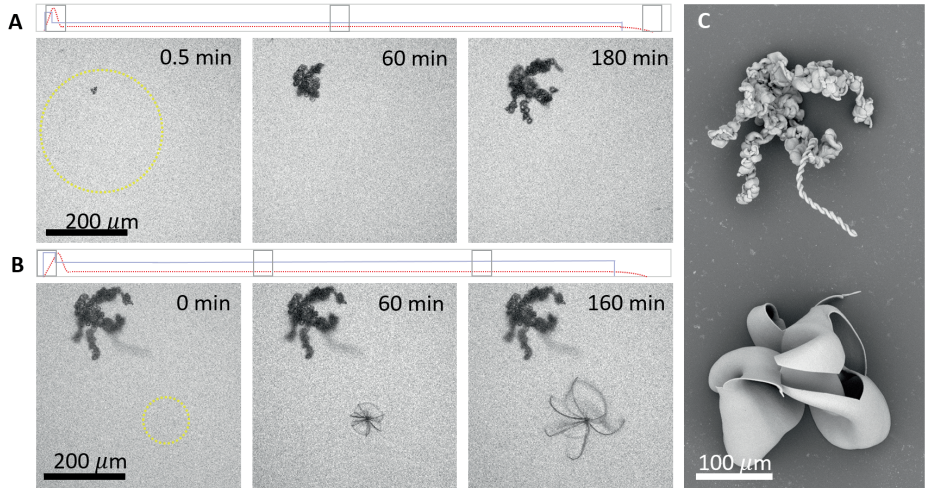

Figure 2.4: Light-controlled nucleation and growth of a helical and coral shaped structure next to each other. A) Optical microscopy time-laps series with corresponding light scheme, and SEM micrograph of light-controlled sequential nucleation of helical- and B) coral-shaped composite in preassigned locations, the yellow circles indicate the location of the UV light spots. Grey squares indicate the moments in time of the given time-lapse series. C) SEM of the resulting ensemble of the helical- and coral-shaped composite.

We position the second composite precisely next to the already grown helical-shaped composite and reduce the light spot size to a radius of 50 µm. To demonstrate our control in time, we insert a fresh precursor solution in the reactor cell with a pH of 11.8 and obtain a coral-shaped composite by modulating the light intensity from 500 µW mm^{-2} for 10 s to 10 µW mm^{-2} for 270 min (Figure 2.3 B, C and appendix A Movie 1). Hence, spatiotemporal control over the carbonate generation with micrometer resolution offers the versatility for sequentially positioning predefined shapes in precisely assigned locations.

Patterns that project arrays of light spots offer exciting opportunities for initiating nucleation of multiple composites simultaneously. To this aim, we project a hexagonal photomask pattern with spots of 45 µm radius and 300 µm spacing (Figure 2.5). As expected, we observe that upon irradiation nucleation occurs inside the light spots, but we also observe nucleation in-between the irradiated areas, presumably due to carbonate diffusion away from the spots. Based on insights from nucleation theory,[63,73,140] we regain spatial control by first randomly positioning submicrometer sized calcium carbonate seeds on the substrate to lower the surface free energy. To induce quick nucleation of $BaCO_3/SiO_2$ corals in the light patterns, we shortly irradiate for 2 min with high light intensity (100 µW mm^{-2}). Subsequently, we turn off the light for 2 min to avoid the buildup of high carbonate concentrations in-between the

spots. Then, we switch on the UV light but with lower intensity (20 µW mm^{-2}) to continue growth. Following this approach, we control the precipitation of large hexagonal patterns of coral shapes that exclusively form in the irradiated areas (Figure 2.3 B). These results highlight that controlling both the local carbonate concentration and the surface free energy of the substrate enable precise positioning of multiple nuclei simultaneously.

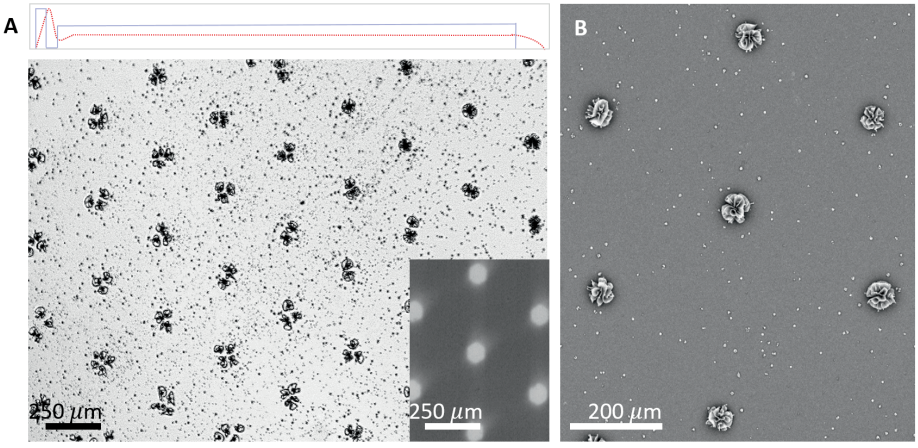

Figure 2.5: Light-controlled nucleation and growth using a photomask. A) Optical microscopy photo of $BaCO_3/SiO_2$ coral shapes that are positioned in accordance to a hexagonal pattern of UV light spots (inset) that is projected using a photomask. B) SEM of the $BaCO_3/SiO_2$ coral shapes positioned in a light-controlled hexagonal pattern, with micrometer-sized $CaCO_3$ crystals that are randomly positioned to lower the surface free energy of the quartz substrate for rapid nucleation inside the UV light spots.

To demonstrate 2) light-controlled contouring and sculpting of individual parts of a single composite structure, we study how the boundary of the light pattern defines the growth for a selection of geometrically shaped light patterns such as triangles, circles, and squares (Figure 2.6). After observing nucleation, we lower the light intensity to maintain growth (> 12 h). In the first hours of growth, we observe that the growth front proceeds isotropically outward with a constant growth rate of ≈ 0.4 µm min^{-1} (Figure 2.6 A,B and appendix A Movies 2). Approaching the boundaries of the light pattern, the nanocomposite structure curls up perpendicular to the substrate to continue growing within the contours of the irradiated area where carbonate is generated. These results suggest that—despite diffusion—the carbonate concentration outside the light area is not sufficient for further growth. Thus, by balancing photogeneration, precipitation, and diffusion of carbonate species, we restrict the growth front to stay precisely within the boundaries of the irradiated area.

We investigate how the reaction temperature can be exploited to define the growth in more complex light patterns containing concave as well as convex corners, such as crosses (Figure 2.6 C and appendix A Movie 2). As expected, for convex corners the growth front stays within the boundaries of the light pattern at 20°C. However, for the concave corners, carbonate diffusion from the neighboring irradiated areas results in the growth front breaching the boundary of the light pattern. To mitigate the resulting loss of resolution, we increase the reaction temperature from 20 to 40°C to deliberately control the balance between the carbonate precipitation and diffusion rate. We observe that the nucleation rate

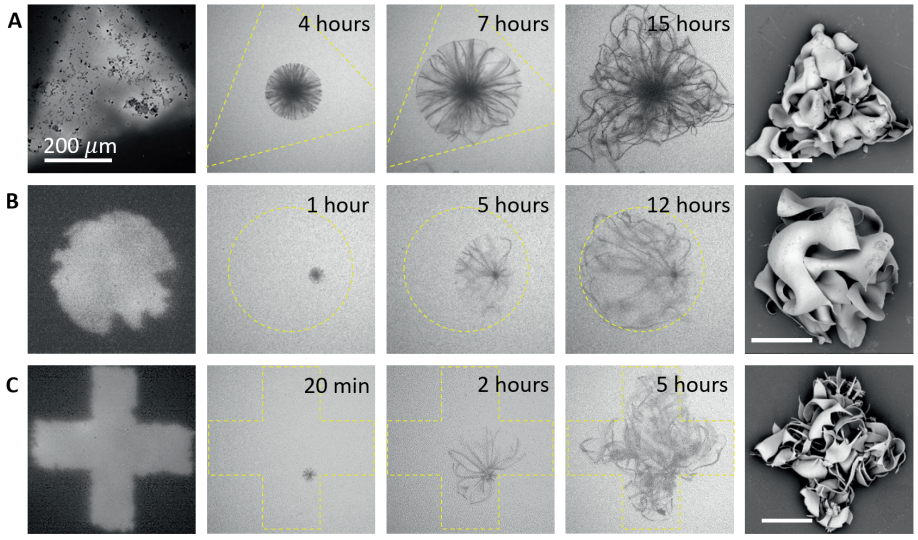

Figure 2.6: Contouring and shaping of individual nanocomposites. All $BaCO_3$/silica composites grow within the irradiated light area for A) triangular- and B) circular-, and C) cross-shaped pattern that is projected on the substrate (left column) as indicated by the yellow dotted line in the time-lapse (middle column) and is confirmed by SEM (right column). Precipitation follows the contours of the light pattern by curling up toward the irradiated area. Concave corners require an elevated reaction temperature of 40°C. All scale bars represent 200 µm.

decreases due to a higher diffusion rate of the released carbonate. To compensate for this higher diffusion rate, we double the light intensity from ≈ 50 µW mm^{-2} at 20°C to ≈ 100 µW mm^{-2} at 40°C to induce nucleation within seconds in the irradiated area of the cross pattern. As a result of the elevated temperature and higher light intensity, we observe that the composite grows with increased rate due to the faster precipitation of barium carbonate and silica.[83,141] Moreover, we find that small deviations in increase or decrease of the light intensity lead to rapid new nucleation or a complete stop of growth, respectively. Importantly, we observe that the growth front now follows the contours of the irradiated area with micrometer precision even for concave corners (Figure 2.6). The subtle balance between the precipitation rate and carbonate diffusion can thus be optimized by modulating the reaction temperature and photogenerated carbonate release to precisely guide self-assembly following the contours of user-defined light-patterns.

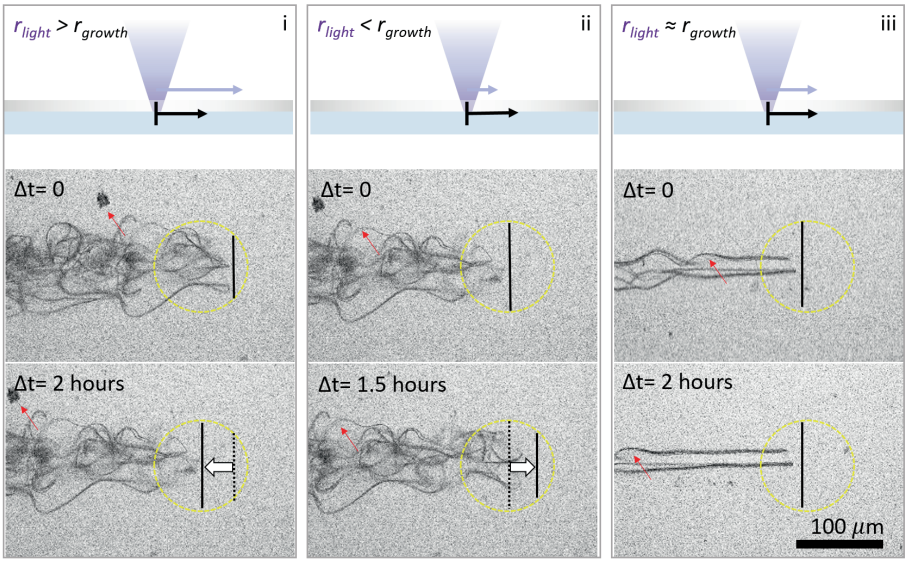

Figure 2.7: Dynamic light patterns for drawing composite lines. Schematic drawing and optical microscope time lapse series for i) $r_{light} < r_{growth}$, ii) $r_{light} > r_{growth}$, and iii) $r_{light} \approx r_{growth}$ showing tapering, broadening, and growth with constant width respectively. The yellow circle indicates the position of the UV light spot (50 µm radius), the black solid and dashed line indicate the position of the growth front present and previous position respectively, and the white arrow indicate the shift of the growth front relative to the light spot. Red arrows indicate features on the substrate that illustrate the movement of the substrate relative to the light spot.

Finally, we demonstrate 3) dynamic steering of self-assembling composites. Our light-mediated control over nucleation and growth opens up the opportunity to steer the self-assembly of nanocomposites using dynamic light patterns, akin state-of-the-art photolithography techniques. To explore this potential, we dynamically move light patterns to "draw" precipitation into lines. We first initiate nucleation of a coral-shape in a 50 µm radius light spot with 500 µW mm^{-2}. Subsequently, we lower the UV light intensity to 20 µW mm^{-2} and move the light spot ahead of the growth front using the motorized stage with velocity r_{light} (Figure 2.7). As expected, the non-irradiated side of the composite stops growing completely. In contrast, the irradiated side—where carbonate is photogenerated—continues growing with a shape and rate r_{growth} which dependents on the growth front's spatial location relative to the irradiated area. We find three clear regimes (Figure 2.7 i–iii). For $r_{light} > r_{growth}$, the composites first continue to grow in the direction of the light spot, but the growth front tapers, until it completely stops due to a limited concentration of carbonate (Figure 2.7 i). For $r_{light} < r_{growth}$, the composite overtakes the light spot until it reaches the boundary of the light, (Figure 2.7 ii). Consequently, the shape of the composite develops in a waving pattern, which we explain by the different carbonate concentrations over the area that results in broadening, bifurcating and curling up of the growth front. For $r_{light} \approx r_{growth}$, the growth front of the composite remains at the same position relative to the light spot and therefore experiencing a constant concentration of carbonate to yield a regular line with constant width (Figure 2.7 iii). Based on these insights, we precipitate a nanocomposite line with $r_{light} \approx r_{growth}$ of 30 µm width which is more than 2 mm long (Figure 2.8 and appendix A Movie 3), hence demonstrating the level of control that can be achieved by matching the rate of the light spot that generates carbonate

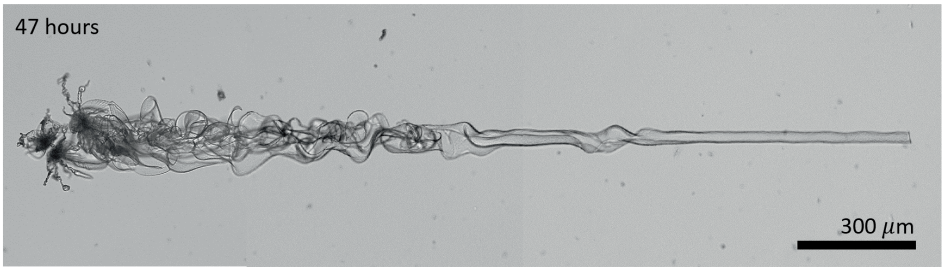

Figure 2.8: Millimeter-sized nanocomposite directed by dynamic light patterns. Optical microscope photograph of the millimeter-sized nanocomposite directed for 47 h by the moving light beam grown with different r_{light}, resulting in a waving growth front (left side of structure) until $r_{light} \approx r_{growth}$ is found, where a constant local carbonate concentration results in a constant line width (right side of structure).

with the rate of precipitation that consumes carbonate.

2.3 Conclusion

In summary, we here introduce light-controlled nucleation and shaping of self-assembling $BaCO_3/SiO_2$ nanocomposites. We find that guiding of the self-assembly is possible when all essential reaction, diffusion, and crystallization processes are properly balanced. We foresee that further refined reaction control is possible using three-dimensionally controlled light patterns—for instance achievable using two-photon techniques—while diffusion and crystallization may be further optimized using gels and surface chemistries such as self-assembled monolayers, respectively. We anticipate that the rate of self-assembly and control over the microscopic structure can be greatly optimized by modifying the local reaction conditions, in particular the reaction temperature and light intensity. Additionally, understanding and tailoring of the internal nanoscopic structure, in particular the ordering of the nanocrystals, will be essential to gain further control over the microscopic form and enable light-directed assembly of more complex shapes.

Importantly, the insights presented here can directly be applied to control nucleation and growth in a broad range of carbonate salts, including widely-studied calcium carbonate salts and precursors for perovskite semiconductors, and similar photochemical reactions may also be possible for other precipitation reactions. Furthermore, the biocompatibility of Ketoprofen opens up the perspective to manipulate and even control biomineralization processes in-vivo using light patterns.

Compared to traditional photolithography resins, nanocomposites offer unprecedented versatility for post-fabrication modification. Already shape-preserving ion-exchange reactions have been developed toward a wide pallet of chemical compositions including perovskites, metals, and metal chalcogenides.[84,86,99–101,122,136,137] Therefore, the here-demonstrated light-controlled assembly strategies give unique independent control over shape and composition which directly impacts our access to user-defined chemical compositions with desirable optic, catalytic, electronic, magnetic, and photovoltaic functionalities. The power of our strategy is that it enables full leveraging of the precision and

control of photolithography techniques with the versatility and simplicity of bioinspired self-assembly. Hence these results forge a genuine collaboration with self-assembly processes: simple hands-off autonomy when possible, and precise hands-on command when necessary.

2.4 Experimental

Preparation of $BaCO_3/SiO_2$ Composites

Typically, the precursor solution was prepared dissolving 6.3 mg (3 mM) KP (Fluorochem) and 87.5 mg (30 mM) DTAB (VWR) in an 8 mL aqueous solution containing 10.6 mg (11 mM) sodium metasilicate (Na_2SiO_3) (Sigma Aldrich). Brief sonication was used to enhance the dissolution of KP. In another vial, 49.5 mg barium chloride dihydrate ($BaCl_2{\cdot}2H_2O$) (Sigma Aldrich) was dissolved in 2 mL degassed water (100 mM). The final growth solution was obtained by adding the KP-DTAB-Na_2SiO_3 solution to the $BaCl_2$ solution. The final growth solution (20 mM$BaCl_2$, 9 mM Na_2SiO_3, 2.5 mMKP, and 25 mM DTAB) was directly injected in a closed sample cell, made of two quartz substrates and a Viton® spacer (2–3 mm, 1.3–1.9 mL volume). All solutions were kept under nitrogen during preparation to avoid any uptake of carbonate species from the air. For the use of higher concentrations KP, a concentration ratio of 1:10 KP:DTAB was used. After growth with the help of UV-light irradiation, the substrates were disassembled in degassed water and carefully washed with acetone. SEM imaging was carried out using an FEI Verios 460.

Preparation of $CaCO_3$ Patterned Substrates

The solution for the calcium carbonate patterning was prepared by dissolving 2.5 mg KP together with 25 mg DTAB in 8 mL degassed water. Sonication was used to enhance the dissolution of KP. In another vial, 22.5 mg calcium chloride dihydrate ($CaCl_2{\cdot}2H_2O$) was dissolved in degassed water and added to the KP-DTAB solution. The solution was adjusted to pH 11.5 with a NaOH solution, which was freshly made under nitrogen to avoid any uptake of CO_2 from the air. The final solution (15 mM$CaCl_2$, 2.5 mMKP, 25 mMDTAB) was injected into the sample cell and irradiated for 2 min with the 275 nm UV light with high intensity (100 µm mm^{-2}). After irradiation, the substrates were washed with degassed water, acetone, and isopropanol and dried with nitrogen.

Home-Built UV-Irradiation Microscopy

In the home-built setup used for the photodecarboxylation process, three main parts could be identified: the photolithography part, the sample holder stage, and the imaging part. In the irradiation part, the light of a 275 nm mounted LED (Thorlabs M275L4, 80 mW output power) was collected by a lens (Edmund Optics UV–vis CTD 84–337, focal length (f) = 20.0 mm). Custom-made photomasks were placed after the collector lens and a light pattern was projected with the help of two UV anti-reflection coated plano-convex lenses (Thorlabs LA4148-UV, f = 50.0 mm) on the sample. To enhance the definition of the projection, a field-aperture iris (Thorlabs SM1D12CZ) was used. To control the light intensity, neutral density (ND) filters (Thorlabs NDUV-B), were used, as well as adjustments of the LED driving current. The sample holder stage consisted of a custom-made temperature cell on top of a motorized translation table. The temperature was controlled by a bath and circulation thermostat (Huber CC-K6). Motion

control was provided by piezo inertia actuators (Thorlabs PIAK10) that had a typical step size of 20 nm. In the imaging part, a cold white light mounted LED (Thorlabs MCWHL5) was collected by an aspheric lens (Thorlabs ACL2520U-DG6-A, f = 20.0 mm). A 10:90 beamsplitter (Thorlabs BSN10R) directed the light through a 10×/0.30 magnification objective (Nikon Plan Fluor) to the sample. The reflected images were collected with the same objective lens and transmitted through the beamsplitter. With help of a tube lens (Thorlabs AC254-200-A-ML), images were recorded by a CMOS camera (Basler Ace acA1920-40gc).

Chapter 3

Light-controlled morphological development of self-organizing bioinspired nanocomposites

Abstract

Nature's intricate biominerals inspire fundamental questions on self-organization and guide innovations towards functional materials. While advances in synthetic self-organization have enabled many levels of control, generating complex shapes remains remains difficult. Specifically, controlling morphologies during formation at the single micro/nanostructure level is the key challenge. Here, we steer the self-organization of barium carbonate nanocrystals and amorphous silica into complex nanocomposite morphologies by photogeneration of carbon dioxide (CO_2) under ultraviolet (UV) light. Using modulations in the UV light intensity, we select the growth mode of the self-organization process inwards or outwards to form helical and coral-like morphologies respectively. The spatiotemporal control over CO_2 photogeneration allows formation of different morphologies on pre-assigned locations, switching between different growth modes—to form for instance a coral on top of a helix or vice versa, and subtle sculpting and patterning of the nanocomposites. These findings advance the understanding of these versatile self-organization processes and offer new prospects for tailored designs of functional materials using photochemically driven self-organization.

This chapter is based on Bistervels, M. H., Hoogendoorn, N. T., Kamp, M., Schoenmaker, H., Brouwer, A. M., & Noorduin, W. L. (2024). Light-controlled morphological development of self-organizing bioinspired nanocomposite. *Nanoscale*, 16, 2310 - 2317.

3.1 Introduction

Control over mineralization is essential for organisms to organize simple building blocks into complex morphologies with tailored functionalities.[1,5,6,8,9,14] For instance, biominerals comprised of calcium carbonate or calcium phosphate such as observed in mollusk shells,[3] skeletons,[2,142] and microlenses,[4] can exhibit diverse morphologies that go beyond their crystallographic symmetries optimized in shape to fulfil specific mechanical, structural, or optical functions.[143] Inspired by such examples, a wide range of synthetic self-organization strategies have been developed that are focused on morphological control.[16,19,38,144–149]

From this perspective, the nanocomposite morphologies that form during co-precipitation of barium carbonate ($BaCO_3$) nanocrystals with amorphous silica (SiO_2) are promising (Figure 3.1).[80,81,83,87,89,91,150] This bioinspired reaction yields a wide diversity of shapes and symmetries such as vases, helices and coral-like forms that can be further sculpted and patterned by controlling the reaction conditions.[82,90,92,94,151] These morphologies show optical properties such as waveguiding and polarization.[85] Moreover post-process surface functionalization,[96–98] and ion exchange reactions have been developed towards a wide range of chemical compositions to introduce optoelectronic,[84,152] catalytic,[100] and magnetic[86] functionalities with preservation of the initial morphology. Control over the morphology is essential for these functionalities: e.g. the helical shape turns nanocomposites into circular optical polarizers, while the coral-like forms offer large macroscale surfaces for maximum accessibility of the reagents and products that boosts catalytic performance.[85,86,100]

Recently, more refined control over the precipitation of these mineral composites was achieved by local generation of carbonate using ultraviolet (UV) light-patterns (Figure 3.1 B).[153] Specifically, photodecomposition of the organic molecule ketoprofen releases carbon dioxide (CO_2) , which in turn can onset the co-precipitation of $BaCO_3$ and SiO_2. Until now, light-induced morphological development of $BaCO_3/SiO_2$ has been focused on when and where carbonate is generated. What has not been explored, is if the morphological development can be steered by how much carbonate is generated.

So far, morphological development has been controlled between two growth modes: i) growth away from the bulk solution to form sheets, globular structures and helices, which happens at the lower pH limit (ca. 10.8-11.3) and increases SiO_2 precipitation; ii) growth towards the bulk solution to form stems, vases and coral-like forms, which occurs at higher pH (ca. 11.8-12) and favors precipitation of $BaCO_3$. Moreover, simple modulations in chemical conditions such as CO_2 modulations already enable further patterning and sculpting of these shapes which can be further positioned into hierarchical tectonic architectures.23 The $BaCO_3$ precipitation rate is directly determined by the concentration of CO_2. Since the CO_2-concentration can be controlled photochemically, this suggests that growth modes and patterns may be selected by modulating the light intensity (Figure 3.1 C).

Motivated by these insights we here steer the co-precipitation of $BaCO_3/SiO_2$ nanocomposites by modulating the UV light intensity (I_{UV}) to generate local CO_2 concentrations via photodecarboxylation. We demonstrate three levels of control: (1) switching between growth modes to form separate helical and coral-like structures; (2) dynamic transitioning between growth modes within a single structure; and

(3) refined sculpting and patterning within one growth mode of a single structure. These results provide further insight in the role of reactions rates on morphological development of these nanocomposites and open opportunities for tailoring self-organization towards bespoke designs of functional materials.

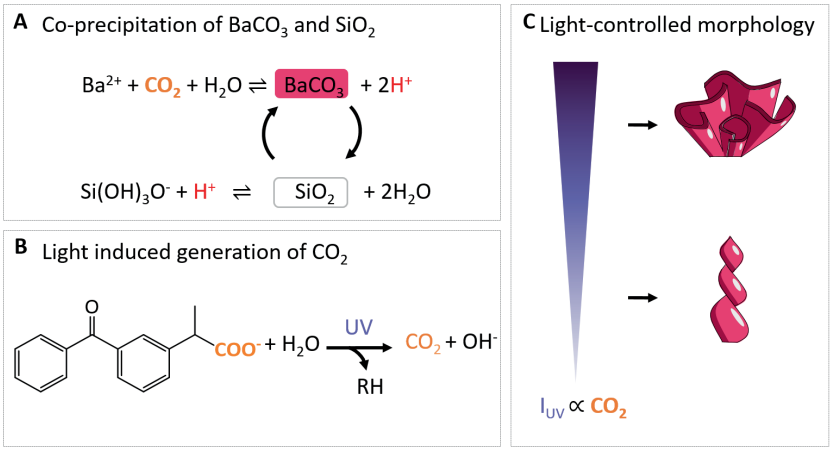

Figure 3.1: Light-controlled shaping of $BaCO_3/SiO_2$ nanocomposites. A) CO_2 induces the acid-regulated co-precipitation of $BaCO_3$ and SiO_2. B) Light-induced photodecarboxylation of ketoprofen into photoproduct RH and CO_2.[154] C) Hypothesis for CO_2 regulated morphological development in different growth modes. High I_{UV} results in high CO_2 production such that $BaCO_3/SiO_2$ composites grow outwards to the bulk solution in coral-like forms, while low values of I_{UV} yield less CO_2 such that growth occurs inwards away from the bulk solution to form helices.

3.2 Results and discussion

Optical setup for light-controlled precipitation

Based on our previous work,[153] we design an optical set-up that enables UV irradiation with spatiotemporal control while simultaneously monitoring the resulting mineralization process (Figure 3.2). For the UV-irradiation, we select a light emitting diode (LED) with a wavelength of 275 nm or 365 nm, which are close to the absorption maximum of ketoprofen.[139] Using a photomask and two lenses, the UV light can be focused in a light spot with a minimum radius up to 10 µm to irradiate a precursor solution in a reaction cell. The reaction cell—comprising two quartz plates that are separated by a Viton® spacer—is positioned into a motorized and temperature-controlled sample holder. To monitor the mineralization process, an optical microscope containing a white LED, objective, and CMOS camera is positioned opposite to the UV-irradiation side.

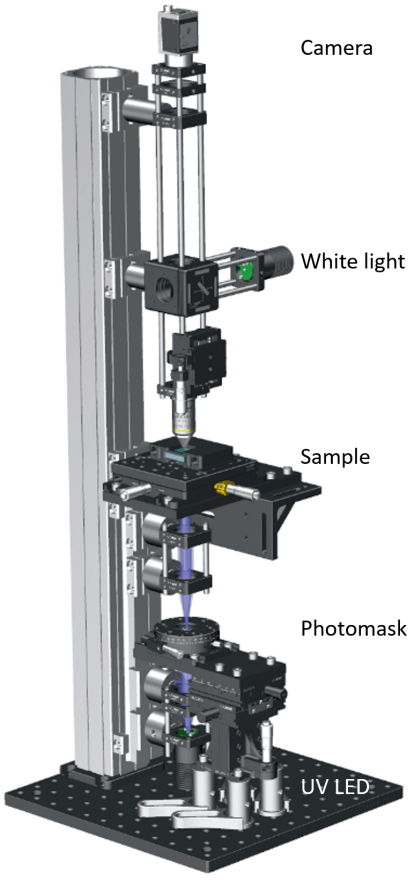

Figure 3.2: Optical setup in which UV light is focused on the reaction cell filled with the precursor solution to photochemically release CO_2. Using white light, the process is monitored in-situ.

Light-controlled switching between growth modes

We investigate if modulations in the UV light intensity I_{UV} can determine the morphologies of the nanocomposites (Figure 3.3). We fill the reaction cell with a precursor solution containing barium chloride (20 mM $BaCl_2$), sodium metasilicate (9 mM Na_2SiO_3) ketoprofen (5 mM), and dodecyl trimethylammonium bromide (50 mM DTAB, a surfactant that is added to dissolve the photoproduct of ketoprofen). Using 0.1 M HCl we lower the pH of the solution to 10.9, which in previous experiments typically resulted in the formation of helices.[153] Nucleation is induced by irradiating the precursor solution at high I_{UV} of 100 µW mm^{-2} for 6 seconds (UV spot has a 250 µm radius). When the first nuclei are observed within the illuminated area, we lower I_{UV} to 10 µW mm^{-2} (255 min) to enable growth while avoiding further nucleation (Figure 3.3 A). As expected, we observe the formation of helical architectures, which is consistent with the typical growth in solutions of this relatively low pH (Figure 3.2 B, C).

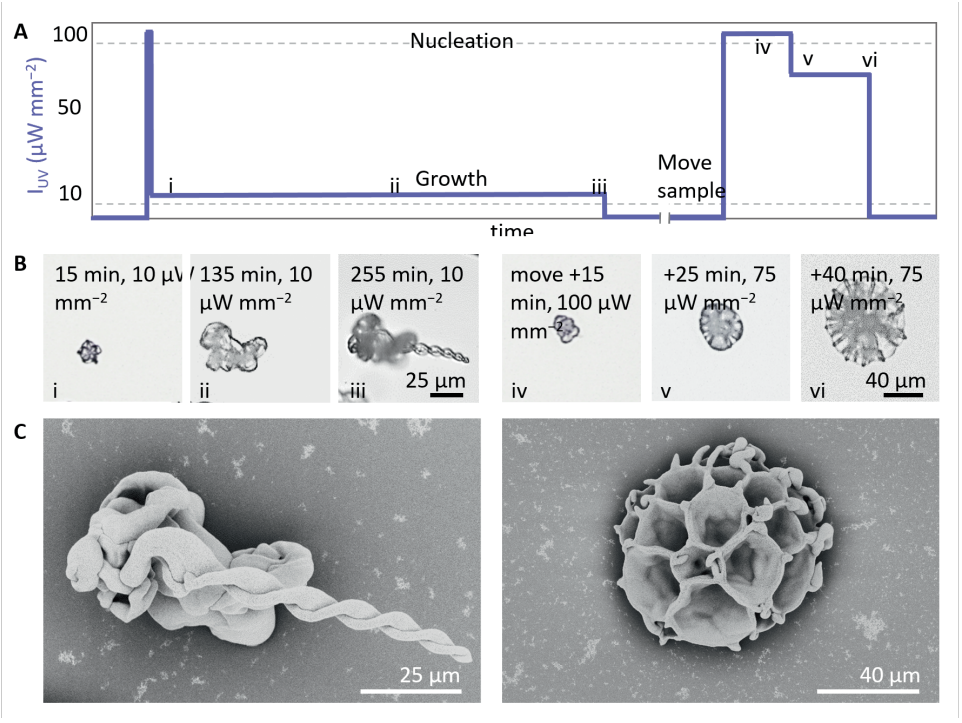

Figure 3.3: Light-controlled switching between helical and coral-like growth modes. A) Applied I_{UV} schedule to yield a helix (left), and in a different location, a coral (right): i) nucleation is induced at high I_{UV}, ii) growth at low I_{UV}, and iii) stopping the precipitation by switching of I_{UV}. After moving the sample cell to a new position, this illumination schedule is repeated: iv) nucleation at high I_{UV} v) growth at slightly lower I_{UV}, v) stopping precipitation by switching off I_{UV}. The proportions of time are indicative and not to true scale. B) Timelapse of in-situ optical microscope images showing the growth of a helix at low I_{UV}, and growth of a coral at high I_{UV}, the indices correspond the indices in (A). C) SEM images of the helical (left) and coral-like (right) form that are grown at low and high I_{UV} respectively.

We hypothesize that growth at higher I_{UV} results in a higher precipitation of $BaCO_3$, which in turn facilitates the formation of coral-like forms even though the low pH of the bulk solution typically favors the formation of helical shapes. To test this hypothesis, we move the sample to irradiate a new location in the reaction cell and induce new nucleation by increasing the I_{UV} to 100 µW mm^{-2} for 20 minutes. We continue growth by lowering I_{UV} to 75 µW mm^{-2} (20 min). This light intensity is 7.5 times higher than the previously used I_{UV} for growing the helical structure, but sufficiently low to avoid undesired nucleation (Figure 3.2 A). We observe the formation of a coral-like architecture (Figure 3.2 B, C). Because I_{UV} is much higher, more CO_2 is generated and consequently the coral grows faster than the helix. Replicating the experiment consistently yields characteristic helical shapes for low values of I_{UV} (5-10 µW mm^{-2}) and coral-like shapes for high values of I_{UV} (50-75 µW mm^{-2}), independently of the previous growth mode (appendix B, Figure B.1 and B.2). Scanning electron microscopy (SEM) images of the corresponding morphologies confirm the development of the helical and coral-like forms. In addition, repeatedly switching between both growth modes is possible and consistently yields coral-like shapes for high I_{UV} and helices for low I_{UV} (appendix B, Figure B.2). During this switching, we do find a reduction of the nucleation rate over time, which we contribute to depletion of the precursor solution, accumulation of

photoproduct, and oligomerization of silica. To compensate for this reduction in nucleation rate, we increase the photogeneration of CO2 by increasing the I_{UV}. Hence, modulations of I_{UV} enable switching between growth modes (Figure 3.2 C).

Switching growth modes within a single structure

The morphology of the growing composite is to a large extend independent of the underlying shape. This suggests that it may be possible to switch between different growth modes within a single structure by modulating I_{UV} (Figure 3.4). To explore this refined control over morphological development, we prepare a precursor solution (20 mM $BaCl_2$, 9 mM Na_2SiO_3, 5 mM ketoprofen, 50 mM DTAB, pH 10.9). We initiate nucleation (100 µW mm^{-2}, 18 s, 150 µm radius) and subsequently grow a coral shape at high I_{UV} (75 µW mm^{-2}) (Figure 3.4 A). Once the coral shape is formed after 20 min (Figure 3.4 B and appendix B Figure B.3 and Movie 1), we decrease I_{UV} to 10 µW mm^{-2}, the regime where we expect helical growth since less CO_2 is generated. We continue growth in the helical growth mode for longer (ca. 130 min). Due to the lower concentration of CO_2 most of the active growth sites on the coral shape stop growing as they become passivated with silica.[81,88] The parts that continue growing bend towards each other, which is characteristic for precipitation in the helical growth mode. Inspection with SEM confirms that at the initial irradiation at high I_{UV} a coral grows, which continues in helical growth upon decreasing of I_{UV} (Figure 3.4 C).

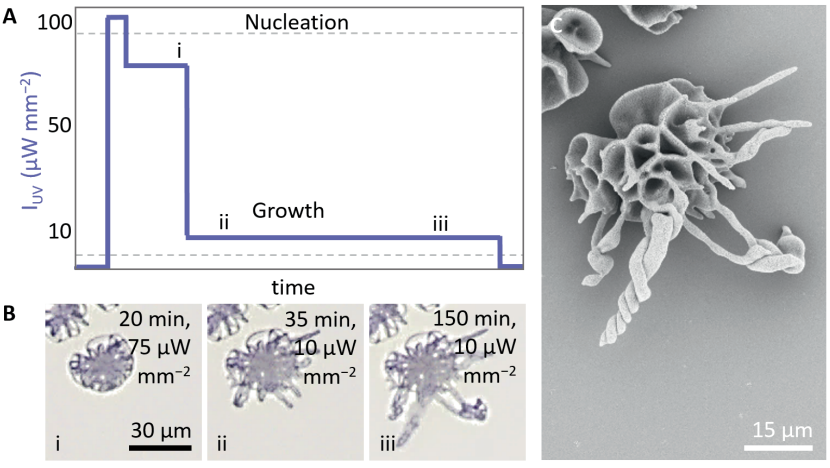

Figure 3.4: Light-controlled switching from a coral to helical growth growth modes within a single structure. A) Indicative I_{UV} schedule for switching from i) coral to ii-iii) helical growth. B) Timelapse of in-situ optical microscope images showing the switching from a coral growth into helical forms. C) SEM of the resulting structure. The figures show a zoom in of the illuminated area, for a complete overview see appendix B, Figure B.2.

To transition from helical growth to corals, we reverse the light intensity schedule (Figure 3.5 A). We prepare a precursor solution (20 mM $BaCl_2$, 11 mM Na_2SiO_3, 5 mM ketoprofen, 50 mM DTAB, pH 11.3). After nucleation at high I_{UV} (100 µW mm^{-2}, 25 s, 250 µm radius), we induce helical growth at low I_{UV} (10 µW mm^{-2}, 110 min). Subsequently, we increase the CO_2 concentration by increasing I_{UV} to 100 µW mm^{-2} (30 s), followed by I_{UV} to 50 µW mm^{-2} (35 min) to move into the coral growth mode. Indeed, time-lapse

microscopy (Figure 3.5 B and appendix B Movie 2) and SEM (Figure 3.5 C) confirm that at low I_{UV} initially a helix forms, that subsequently transitions into a coral like form at high I_{UV}. In addition, repeatedly switching between both growth modes is possible and consistently yields coral-like shapes for high I_{UV} and helices for low I_{UV} (appendix B, Figure B.2). During this switching, we do find a reduction of the nucleation rate over time, which we contribute to depletion of the precursor solution, accumulation of photoproduct, and oligomerization of silica. To compensate for this reduction in nucleation rate, we increase the photogeneration of CO_2 by increasing the I_{UV}. Modulations in I_{UV} thus enable direct switching between growth modes within a single structure.

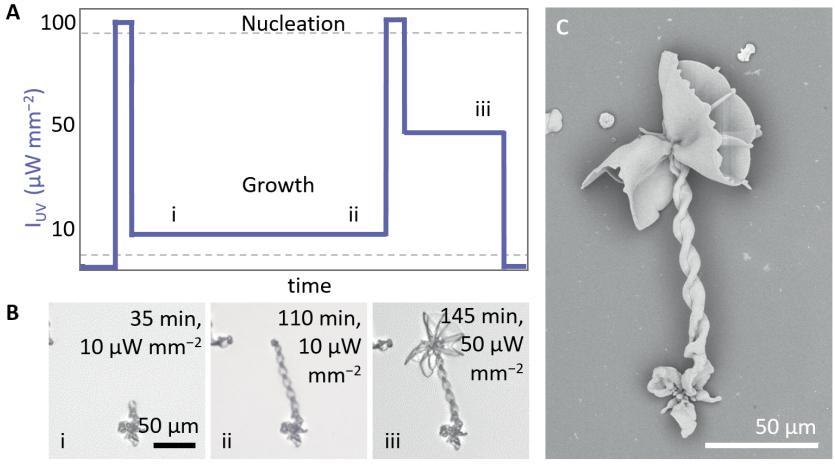

Figure 3.5: Light-controlled switching from a helical to coral growth modes within a single structure. A) Indicative I_{UV} schedule for switching from i-ii) helical to iii) coral growth. B) Timelapse of in-situ optical microscope images showing the switching from growth a helix into a coral. Indices correspond with the indices in I_{UV} schedule. C) SEM of the resulting structure. The figures show a zoom in of the illuminated area, for a complete overview see appendix B, Figure B.3.

Light-controlled sculpting and patterning

The sensitivity of the co-precipitation process towards modulations in the CO_2 concentration offers the opportunity for light-controlled shaping within a growth mode. We exemplify this capability by sculpting an architecture within the coral growth mode according to a user-defined pattern (Figure 3.6). In previous research it was already shown that CO_2 pulses in the bulk solution can result in sculpting and patterning.23 We now investigate if local generation of CO_2 still enables such control.

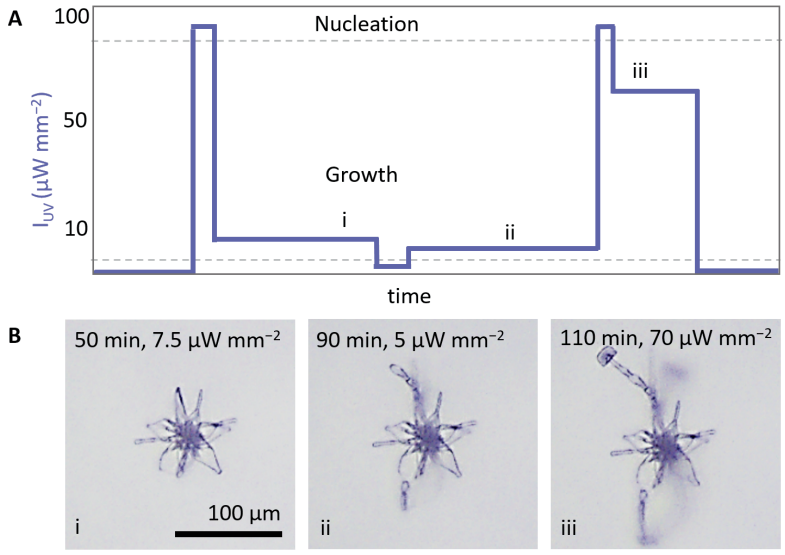

Figure 3.6: Dynamic light modulation for refined sculpting within a growth mode. A) Indicative I_{UV} schedule. B) Timelapse of in-situ optical microscope images of growing architectures, showing i) initial growth of a coral shape followed by ii) the narrowing of the growth front to give stems at reduced I_{UV}, that subsequently iii) open in vase-like shapes upon increasing I_{UV}, indices correspond the with the indices in illumination schedule.

To demonstrate sculpting, we first induce nucleation (I_{UV} = 100 µW mm^{-2}, 3 s, 250 µm radius) and growth of a coral-like structure in a precursor solution (20mM $BaCl_2$, 9 mM Na_2SiO_3, 2.5 mM ketoprofen, 25 mM DTAB, pH 11.5). Once a coral form grows (I_{UV} = 7.5 µW mm^{-2}, 55 min), we adjust the carbonate supply by reducing I_{UV} (2 µW mm^{-2}, 3 min), resulting in the development of thin stems. To prevent complete passivation of growth sites by silica, we slightly increase I_{UV} (5 µW mm^{-2}, 45 min), and achieve a balance between carbonate supply and consumption such that stem growth is sustained. Then, we boost the local CO_2 concentration and thereby trigger the splitting of the stems by applying a high intensity pulse (100 µW mm^{-2}, 4 s). During the splitting, the nanocrystals arrange with a wider splay, which results in an increase of the surface (Figure 3.7). Importantly, even though initially this high light intensity initially was also used to induce nucleation, now no new nucleation is observed as the already active growth sites deplete the local CO_2 concentration. Finally, growth is continued at lower I_{UV} (70 µW mm^{-2}) for 10 minutes to continue growth into vase-like forms, showing that dynamic modulations in light-intensity enable formation of complex forms (Figure 3.7).

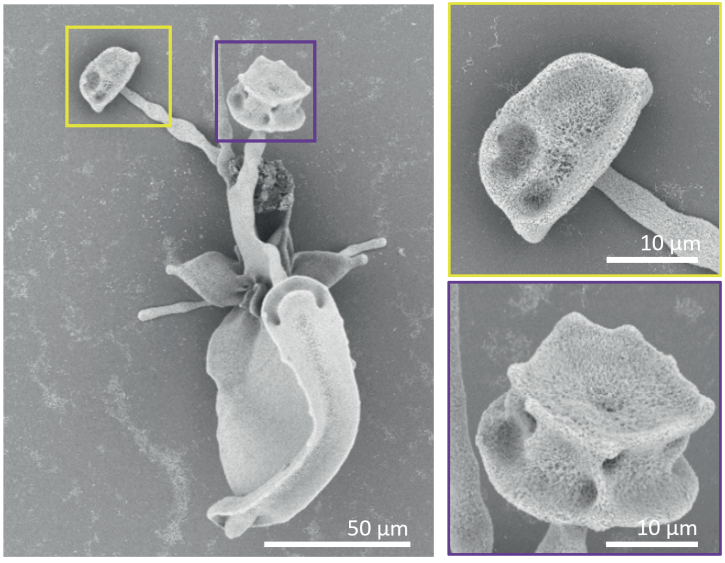

Figure 3.7: SEM images of the grown structure by dynamic light modulation for refined sculpting within a growth mode.

We demonstrate patterning by forming equidistantly spaced bands on a structure. To this aim we perform short rhythmic modulations in I_{UV} using a 365 nm UV light to illuminate a small area of 100 µm radius (Figure 3.8). We prepare a precursor solution (20mM $BaCl_2$, 9 mM Na_2SiO_3, 5 mM ketoprofen, 50 mM DTAB, pH 11.5). We induce nucleation using a high I_{UV} for 5 seconds (175 µW mm^{-2}) and enable growth for 75 minutes at low I_{UV} (15 µW mm^{-2}). To selectively enable growth on one side, we maintain the UV spot on one side of the growth front by moving the sample stage with a pace that matches the growth rate of the architecture (Figure 3.8 B). To form equidistantly spaced bands, we take advantage of the fact that the growth rate is approximately linear in time. To form a band, we apply a short 5 second pulse in I_{UV} (175 µW mm^{-2}) and subsequently enable 12 minutes of growth with I_{UV} back to the original low I_{UV} (15 µW mm^{-2}) before we apply another two sets of 5 seconds high I_{UV} (175 µW mm^{-2}) followed by 12 minutes low I_{UV} (15 µW mm^{-2}). This rhythmic light schedule of three short pulses equally paced in time results in three well-defined bands equally distanced in space (Figure 3.8 C), hence demonstrating the spatiotemporally control that can be achieved over self-organization.

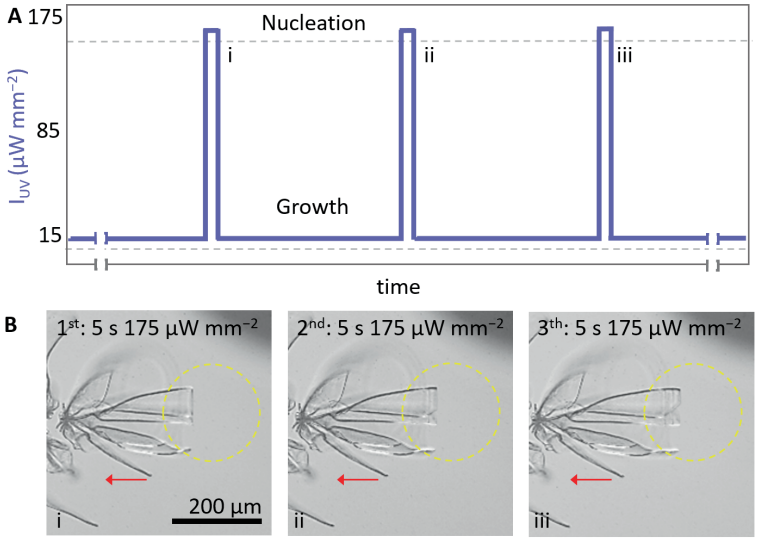

Figure 3.8: Dynamic light modulation for rhythmic patterning. A) Selection of the indicative I_{UV} schedule, in which three short periods of 5 second pulses of high I_{UV} (365 nm) with 12 minutes of low I_{UV} is used to pattern a growing structure. B) Timelapse of the growing structure after each pulse of high I_{UV}. The dashed yellow circle represents the UV spot. The red arrow indicates the direction in which the sample is moved. Indices corresponds with indices in (A).

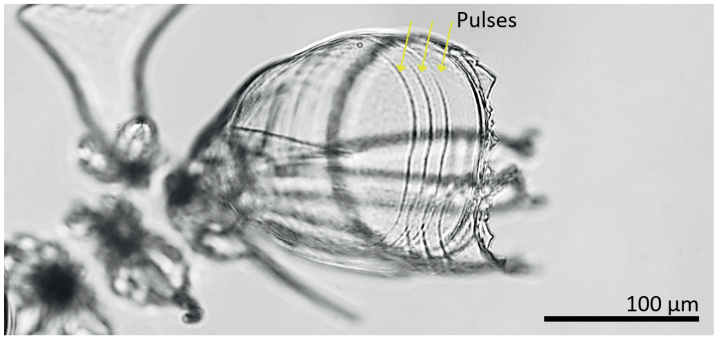

Figure 3.9: Light microscope image of grown structure by dynamic light modulation for rhythmic patterning. The yellow arrows indicate the moments of pulses in I_{UV}.

Mechanistic insights in co-precipitation reaction

Our results provide insights in the formation mechanism of $BaCO_3/SiO_2$ nanocomposites. In well-studied configurations of $BaCO_3/SiO_2$ co-precipitation,[81,83] CO_2 diffuses from the air into the reaction solution. In such open systems, switching from helical to coral growth typically requires an increase of the pH from 11 to 12. Increasing the pH from 11 to 12 results in an approximate tenfold increase in CO_2 that is taken up from the air into the solution.[155] In contrast, in the closed reaction cell that we study here, CO_2 is only generated photochemically in the solution. Although we are not able to determine the exact concentration of CO_2 that is generated, we find an approximate tenfold increase in I_{UV} results in switching from helices to corals. Hence both in open and closed systems an approximate tenfold increase in either CO_2 uptake or I_{UV} is required to switch from helical to coral growth modes, which emphasizes the importance of the CO_2 concentration in the morphological development.

The controlled local photochemical generation of CO_2 also gives insights into the role of the solution pH and silica polymerization during the co-precipitation. In open systems CO_2 diffusion from the air results in notable acidification of the bulk solution (typically from pH 11.8 to pH 11.5 in 2 hours). This acidification not only reduces the CO_2 uptake from the air, but also induces the polymerization of silica species. The resulting silica oligomers can act as slow-diffusing species that buffer the locally acid environment around the reaction front where the co-precipitation occurs.[81,82,90] In the closed reaction cell, CO_2 is only generated near the precipitating structures, and therefore we observe no significant change in the pH of the bulk solution. Consequently, in the closed system we need to either systematically lower the pH of the bulk (pH 10.5-10.9) or increase the silica content in the solution to access both growth modes. These findings imply that both the silica polymerization and the CO_2 concentration determine the morphological development. Overall, these findings emphasize the intricate interplay between the various components in this self-organization processes and highlight how photochemical processes can help to disentangle these processes for gaining mechanistic understanding.

3.3 Conclusion

In this study, we show how photogeneration of CO_2 can steer the morphological development of $BaCO_3/SiO_2$ nanocomposites. With simple modulations in the light intensity, we steer the balance in the precipitation rates to switch between different growth modes, such that helical and coral-like forms can be developed in separate structures next to each other, or integrated into single structures. Moreover, we demonstrate that rational modulations in the photogeneration of CO_2 enable local sculpting and patterning of structures within a single growth mode by decorating corals with thin stems that subsequently open as vases and applying rhythmic patterning. This refined level of control provides mechanistic insights and expands the possibilities for steering self-organization processes into user-defined shapes.

We foresee that these results can also impact the development of carbonate-silica nanocomposites as a platform for functional materials. Such artificial self-organization processes are still rare. However, we envisage that light-modulations can be used to steer the self-organization of components in a desired shape, after which complete chemical modification with preservation of the original morphology is possible by ion-exchange. These shape-preserving ion-exchange reactions already give access to a

vast and continuously growing library of chemical compositions, which currently provide conversion routes to more than fifty different chemical compositions including perovskites, metal chalcogenides and metals. Moreover, the catalytic, photochemical or electronic functionalities of these bioinspired architectures have already been used, for instance as catalysts for the dry reforming of butanol at low temperatures and the Fischer Tropsch reaction with tunable product distribution.[84,86,152,156,157] We also project that other self-organization processes such as Liesegang-inspired patterning or chemical gardens can be controlled using light-driven reactions.[156,158,159] As next step, integration of these self-organization and conversion principles are currently being developed.

3.4 Experimental

Preparation precursor solution

Typically, the precursor solution is prepared by dissolving 12.6 mg (6 mM) ketoprofen (KP) (Fluorochem) and 175.0 mg (60 mM) DTAB (VWR) in an 8 mL aqueous solution containing 10.6 mg (11 mM) sodium metasilicate (Na_2SiO_3) (Sigma Aldrich). Two minutes of sonication is used to enhance the dissolution of KP. In another vial, 49.5 mg barium chloride dihydrate ($BaCl_2{\cdot}2H_2O$) (Sigma Aldrich) is dissolved in 2 mL degassed water (100 mM). The final precursor solution is made by adding the KP-DTAB-Na_2SiO_3 solution to the $BaCl_2$ solution. The precursor solution (20 mM $BaCl_2$, 9 mM Na_2SiO_3, 5 mM KP, and 50 mM DTAB) is directly injected in a closed sample cell, made of two quartz substrates and a Viton® spacer (2–3 mm, 1.3–1.9 mL volume). All solutions are kept in nitrogen during preparation to avoid any uptake of carbonate species from the air. For higher concentrations KP, a concentration ratio of 1:10 KP:DTAB is used to assure that both KP and the photoproduct remain dissolved.

Preparation reaction cell

The reaction cell is composed of a custom-made holder that has two quartz slides and a Viton® spacer (2–3 mm, 1.3–1.9 mL volume). The substrates are plasma cleaned for 10 minutes. Injection of the precursor solution is performed using a syringe with needle by puncturing through the Viton® spacer.

UV-light irradiation

To induce photodecarboxylation, the sample is irradiated using UV-light irradiation of 275 nm and 365 nm and a radius of 100-250 µm. Selection of the light intensity dependents on the concentration of precursors, absorption wavelength, illumination area, and initial pH.

UV-irradiation Microscope

In the custom-built setup used for the photodecarboxylation process, we identify three main parts: the photolithography part, the sample holder stage, and the imaging part. In the irradiation part, a lens (Edmund Optics 84–337, focal length f = 20.0 mm) collects the light from a 275 nm mounted LED (Thorlabs M275L4, 80 mW output power) or a 365 nm mounted LED (Thorlabs M365L3, 1290 mW output power). The UV light intensity (I_{UV} in µW mm^{-2}) is determined by collecting the UV light on a handheld power meter (Thorlabs PM160T) and dividing the recorded power by the area of the sensor.

Custom-made photomasks are placed after the collector lens and a light pattern is projected with the help of two UV anti-reflection coated plano-convex lenses (Thorlabs LA4148-UV, f = 50.0 mm) on the sample. To control the light intensity, neutral density (ND) filters (Thorlabs NDUV-B) are used, as well as adjustments of the LED driving current. The sample holder stage consists of a custom-made temperature cell on top of a motorized translation table. The temperature is controlled by a bath and circulation thermostat (Huber CC-K6). Motion control is provided by piezo inertia actuators (Thorlabs PIAK10) that had a typical step size of 20 nm. In the imaging part, a cold white light mounted LED (Thorlabs MCWHL5) is collected by an aspheric lens (Thorlabs ACL2520U-DG6-A, f = 20.0 mm). A 10:90 beamsplitter (Thorlabs BSN10R) directs the light through a 10X/0.30 magnification objective (Nikon Plan Fluor) to the sample. The reflected images is collected with the same objective lens and transmitted through the beamsplitter. With help of a tube lens (Thorlabs AC254-200-A-ML, f = 200.0 mm), images are recorded by a CMOS camera (Basler Ace acA1920-40gc).

Post-process analysis

For post-process analysis, After growth with the help of UV-light irradiation, the substrates of the reaction are disassembled by immersing the cell is disassembled in degassed water byand carefully loosening separating the substrates from the spacer. The substrates are slowly pulled out of the water, while sprinkled with acetone, and subsequently dried to air. SEM imaging of the substrates is performed using an FEI Verios 460.

Chapter 4

Compose and convert: Controlling shape and chemical composition of self-organizing nanocomposites

Abstract

Organizing the right material at the right place has the potential to revolutionize bottom-up assembly of functional architectures. Despite tremendous progress, this is still difficult in particular because control over chemical composition and morphology are typically inherently entangled. Here a two-step strategy is introduced based on self-organization and conversion reactions to shape a wide selection of chemical compositions into user-defined designs. First, photogeneration of CO_2) induces precipitation of nanocomposites of barium carbonate nanocrystals and amorphous silica ($BaCO_3$/SiO_2) with control over shape and location following arbitrary illumination patterns. Second, the resulting nanocrystals are converted by sequential ion exchange into a wide pallet of chemical compositions, while the original shape is preserved. By considering thermodynamic stability and chemical reactivity, orthogonal conversion reactions are designed for sequentially positioning nanocomposites of different metal chalcogenide semiconductors next to each other. Based on these strategies, different compositions are integrated into the same hybrid architecture, and the functionality potential is demonstrated by forming a light-emitting perovskite semiconductor that is embedded into an optical waveguide. Combining light-controlled self-organization and shape-preserving ion-exchange reactions offers exciting opportunities for shaping up materials.

This chapter is based on Bistervels, M.H., van der Weijden, A., Kamp, M., Schoenmaker, & Noorduin, W. L. (2024). Compose and convert: Controlling shape and chemical composition of self-organizing nanocomposites. *Advanced Functional Materials*, 2403715, 1-7.

4.1 Introduction

Organizing the right chemical in the right place is at the core of how organisms steer mundane materials into biominerals with remarkable functionalities.[1,3,5–8,142,160,161] While biological processes select building blocks based on evolutionary cues, human-designed self-organization processes can tap into a much wider catalogue of materials that include synthetic compositions with semiconducting, optoelectronic or catalytic properties. Driven by these insights, already many bioinspired processes have been developed to emulate, extend and exceed the performance of biominerals.[12–16,19,20,27,38,162] Nevertheless, despite these successes it remains challenging to achieve independent control over where and in which shape chemical compositions of choice can be sculpted, as the control over shape and chemical composition are traditionally inherently entangled.

We here propose a two-step assembly/conversion strategy to shape desired chemical compositions following predetermined designs (Figure 4.1). In the first step, photodecarboxylation of ketoprofen under ultraviolet (UV) light (275-365 nm) generates carbonate (CO_2), which steers the acid regulated co-precipitation of barium carbonate ($BaCO_3$) nanocrystals and amorphous silica (SiO_2) into a nanocomposite according to light-controlled patterns (Figure 4.2 A). In the second step, ion exchange reactions convert the nanocrystals in the nanocomposite while preserving the original morphology and fine features of the original form (Figure 4.2 B). Even more refined and complex control over shaping of different compositions may be possible by developing orthogonal conversion reactions such that consecutive cycles of assembly/conversion can yield complex rationally designed hybrid architectures. In principle, the here proposed strategy should enable independent control over both the shape and chemical composition of user-defined architectures.

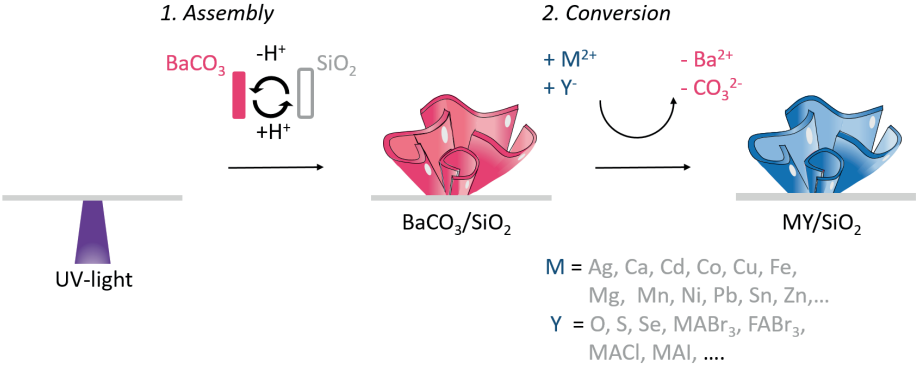

Figure 4.1: Assembly/conversion strategy for controlling shape and chemical composition of self-organizing nanocomposites. UV-irradiation triggers the assembly of $BaCO_3$ nanocrystals and an amorphous SiO_2 matrix into a nanocomposite $BaCO_3/SiO_2$ into light-controlled shapes. Subsequently, the chemical composition of the nanocrystals is converted via a cascade of ion-exchange reactions, into a selection of more than fifty compounds, including metal chalcogenides and perovskites (MA = methyl ammonium, FA = formamidinium).

Our strategy is inspired by previous work on precipitation and conversion reactions of bioinspired

$BaCO_3/SiO_2$ nanocomposites.[80,82,83,87–90,93,150] These nanocomposites form during the acid-regulated precipitation of $BaCO_3$ nanocrystals and amorphous SiO_2. By modulating the precipitation conditions, a wide diversity of complex shapes can be rationally designed. For instance, nanocomposites with stem-, vase- and coral-like shapes can be formed at a pH of ca. 12, while helices and leave-like shapes can be formed at a pH of ca. 11. These shapes can be further sculpted, patterned and hierarchically organized by modulating the reaction conditions e.g. CO_2 concentration, temperature, pH during the growth to stack for instance coral forms on helices, or create landscapes with stems that open into vases.[83] Moreover, photogeneration of CO_2 has been developed to control the precipitation process following UV light patterns (Figure 4.2).[153,163,164] Once these nanocomposites are formed, we have shown that the chemical composition of $BaCO_3/SiO_2$ nanocomposites can be converted by performing cat- and anion exchange reactions, with preservation of the initial shape and fine details.[84,86,97–101,165,166] Importantly, these conversion reactions are to a large extent independent of the initial shape of the nanocomposite such that the shape and chemical composition are disentangled and independently controllable. By now an extensive catalogue of conversion pathways has been developed to more than 50 different chemical compositions including many metal chalcogenides, metals, and perovskites. The semiconducting, optoelectronic and catalytic properties of these compositions have been used to achieve a range of functionalities such as catalysts with tunable selectivity.[84,86,100] However, up to now it has remained unclear if these photochemical precipitation processes and conversion reactions can be combined, let alone if highly selective orthogonal assembly/conversion routes can be developed for consecutive organization of arbitrary chemical compositions in user-defined and functional hybrid architectures.

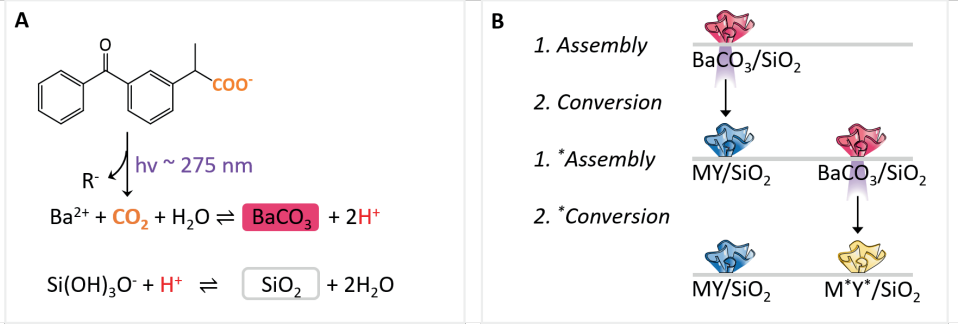

Figure 4.2: A) Photodecomposition of ketoprofen results in CO_2 generation which in turn onsets the co-precipitation of $BaCO_3$ and SiO_2. B) Orthogonal assembly/conversion schemes enable positioning and integration of different chemical compositions into user-defined architectures such that for instance a first assembly/conversion into MY/SiO_2 remains unreactive during the sequential assembly/conversion of another $BaCO_3/SiO_2$ shape into M^*Y^*/SiO_2.

Motivated by these insights, we here demonstrate that a range of light schemes can be used for precipitating nanocomposites on preassigned locations, shaping complex contours, and drawing arbitrary-shaped lines, all of which subsequently can be converted into a range of metal chalcogenide semiconductors with preservation of microscopic shape and fine details. Moreover, based on the thermodynamic stability and chemical reactivity of different compositions, we design orthogonal conversion pathways to sequentially position nanocomposites of different chemical compositions next to each other. Finally, we show how different compositions can be integrated into the same hybrid architecture and form a light-emitting perovskite semiconductor that is embedded into an optical waveguide to

demonstrate the functionality potential of this assembly/conversion strategy.

4.2 Results and discussion

We test the compatibility between ion exchange reactions and photo-induced self-organization. To this aim we combine different light schemes for controllable self-assembly with different types of conversion reactions (Figure 4.2). We show three levels of control over semiconductor sculpting by forming an array of coral-shaped cadmium selenide (CdSe), a triangle of cobalt oxide (Co_3O_4), and a line of manganese sulfide (MnS).

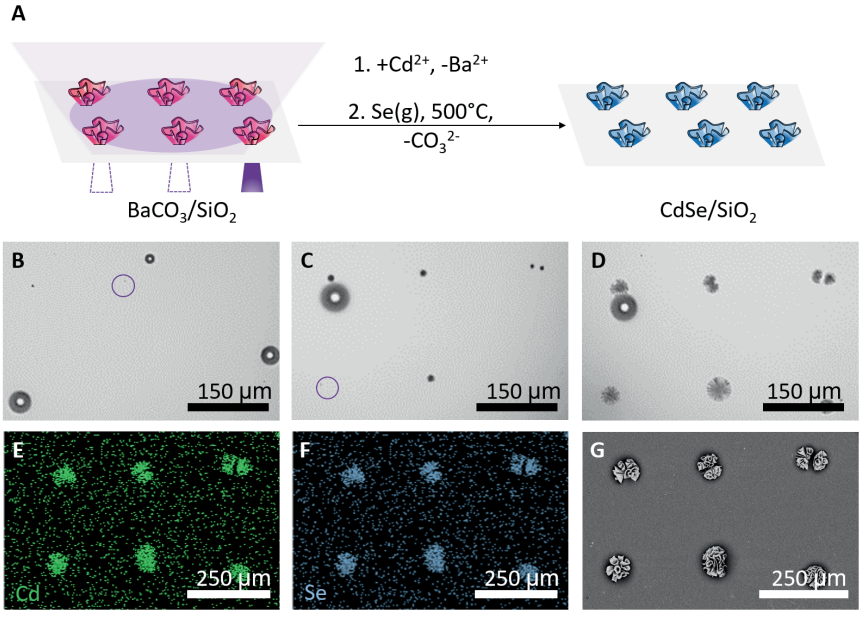

Figure 4.3: Shape-preserving chemical conversion of light-controlled $BaCO_3/SiO_2$ nanocomposites. A) reaction scheme towards an array of six $CdSe/SiO_2$ coral-shapes. B-D) Optical microscopy time-lapse showing sequential positioning of coral shapes using UV spot (indicated with purple circle). E-G) EDS SEM of cadmium (Cd) and selenium in resulting coral shapes.

We position an array of CdSe coral shapes on preassigned locations by photo-controlled co-precipitation of $BaCO_3/SiO_2$ nanocomposites. To this aim, we create a gradient of carbonate that is too low for nucleation yet sufficiently high for growth. We achieve this by illuminating an area with a radius of 250 μm using low intensity 365 nm UV light with a long penetration depth to photogenerate CO_2. Subsequently, we induce nucleation with a short burst of 275 nm UV light with a short penetration depth in a 50 μm radius inside the area irradiated by 365 nm. We achieve this by first illuminating an area with a radius of 250 µm using low intensity 365 nm UV light through the objective to photogenerate

CO_2. Subsequently, we induce nucleation with a short burst of 275 nm UV light that is projected in a 50 µm radius through two lenses from the opposite side inside the area irradiated by 365 nm. Within 15-35 seconds, we observe the formation of a small coral-like form in the area that is illuminated by the 275 nm UV-light (Figure 4.3 A-D, see supplementary information appendix C for details). We repeat this short burst of 275 nm UV light at five other locations to create an array of six coral-shaped nanocomposites on preassigned positions. Note that for each nanocomposite we adjust the light-intensity, as during the experiment precursor depletion, photoproduct accumulation, and silica oligomerization change the conditions such that longer and stronger UV light irradiation is needed to locally generate sufficient CO_2 for nucleation and growth.

We convert this array of coral shapes from $BaCO_3$ into CdSe. Following previously developed methods,[100] we first perform cation exchange of barium to cadmium by immersing the array in a solution containing cadmium ions (50 mM). Subsequently, we perform anion exchange of carbonate to selenium (Se^{2-}) by exposing the array to selenium gas. Energy Dispersion Spectroscopy (EDS) is consistent with complete conversion of $BaCO_3$ to CdSe, while Scanning Electron Microscopy (SEM) shows excellent preservation of the three-dimensional (3D) shape and fine features (Figure 4.3 E-G).

To form a triangular shaped architecture composed of Co_3O_4, we project a triangle light pattern of 275nm (75 $\mu W/mm^2$) and induce nucleation and growth (Figure 4.4 A-D, see appendix C for details). After 5.5 hours we observe a $BaCO_3$-SiO_2 architecture with the contours of the geometric light pattern. The $BaCO_3$ nanocrystals are converted into Co_3O_4 in two steps. First, we exchange barium for cobalt to yield the triangle shape made of basic cobalt carbonate (see appendix C for details). Second, we form the desired Co_3O_4 by heating the nanocomposite in air at 540°C (Figure 4.4 A, E, see appendix C). During the conversion the crystal lattice volume would theoretically shrink with ca. 17%. We find indeed that the structure visibly shrinks, but that it remains completely intact with all fine features preserved (Figure 4.4 F-G).

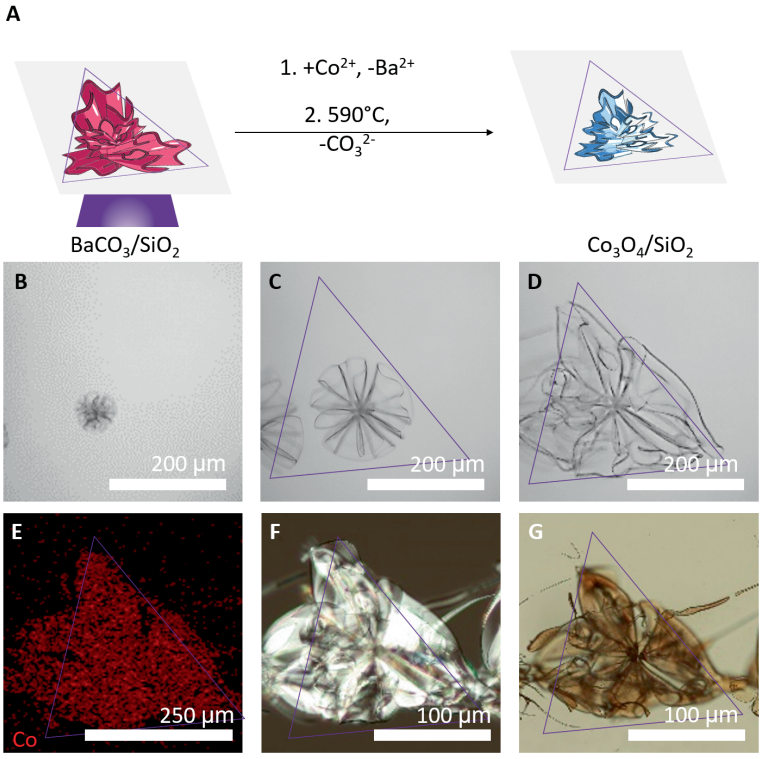

Figure 4.4: A) Reaction scheme towards a Co_3O_4/SiO_2 triangle. B-D) Optical microscopy time-lapse showing the formation of a triangle-shaped nanocomposite within the triangle shaped UV-pattern (indicated in purple). E) EDS SEM map showing cobalt (Co). F) Optical polarization microscopy of the original $BaCO_3/SiO_2$ form. G) Optical microscopy of the converted Co_3O_4/SiO_2 form that is shrunken.

We explore the versatility of light schemes that can be used in combination with ion-exchange. From this perspective, it is particularly interesting to combine UV-induced local photogeneration of CO_2 with near-infrared (NIR) induced local heating. Since for increasing temperatures the precipitation rates of $BaCO_3$ and SiO_2 increase, this local heating can speed up the precipitation and thereby refine the resolution, while the smaller feature sizes may enable steering the precipitate in curves.[153] However, local heating can also enhance crosslinking of the SiO_2 matrix, which in turn may potentially hinder subsequent ion-exchange reactions.[86] To investigate this scenario, we precipitate a nanocomposite line-shape using local heating and subsequently converting this line into a manganese sulfide (MnS) semiconductor.

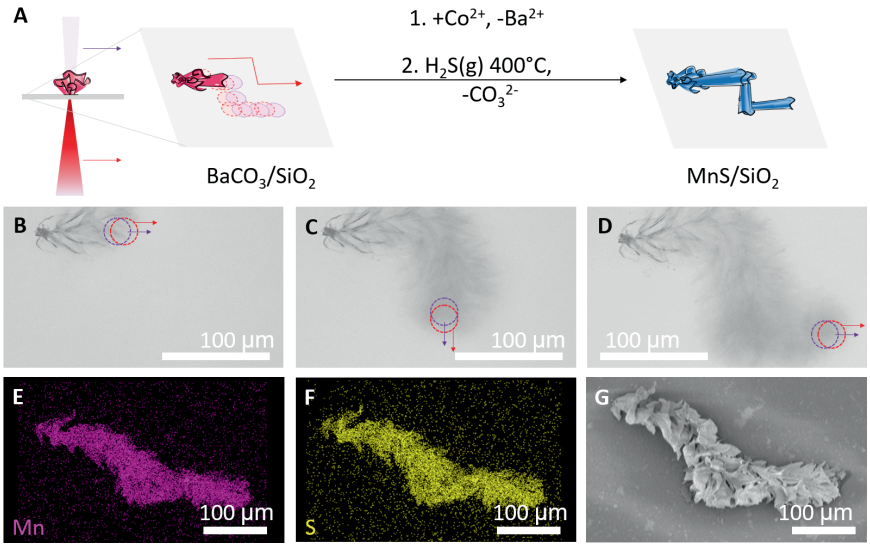

Figure 4.5: A) Reaction scheme for MnS/SiO_2 line. B-D) Optical microscopy time-lapse showing precipitation following a moving UV and IR spot (depicted in purple and red respectively). E-G) EDS SEM analysis showing manganese (Mn) and sulfide (S) in the resulting line-shape.

To investigate this scenario, we precipitate a nanocomposite line-shape by combining a 365 nm UV LED via the objective and a 1435 nm NIR laser diode via two lenses from the opposite site to locally generate CO_2 and heat the solution respectively. By modulating the light intensity (Figure 4.5 A-D, see appendix C for details), we draw an arbitrarily shaped line. To demonstrate the achievable fidelity, we make two 90 degree turns. Subsequently we convert the line into MnS, following previously developed conversion reactions.[86] Even though the local heating may induce further crosslinking of the SiO_2 matrix, we find that the $BaCO_3$ nanocrystals straightforwardly undergo ion exchange to manganese carbonate ($MnCO_3$), which subsequently convert to MnS upon exposure to hydrogen disulfide gas (H_2S). EDS and SEM of the resulting structure shows that the curvatures of the corners have changed—likely due to the mechanical forces that are exerted during the shrinking of the crystal lattice volume during the conversion. Nevertheless, we still find complete conversion (Figure 4.5 E-G, see appendix C for more details), showing that the conversion reactions and different light-schemes are compatible.

This compatibility opens the opportunity for sequential series of photo-induced self-organization and conversion reactions such that for instance, an array of different chemical compositions can be positioned on predetermined locations next to each other. However, such sequential series can only be performed using orthogonal reaction pathways to avoid that earlier formed structures do not undergo ion exchange. To develop such orthogonal reaction pathways, we realize that in water the solubilities of metal carbonates are orders of magnitude larger than those of metal chalcogenides. Consequently, metal carbonates may be prone to undergo ion exchange under conditions in which metal chalcogenides remain unreactive, which may facilitate sequential orthogonal cation-exchange pathways.

To test the concept of such orthogonal cation-exchange pathways, we position coral-shapes of three different semiconductor compositions next to each other (Figure 4.6). To form the first coral shape, we photochemically induce the precipitation of a coral-like shape. We convert the $BaCO_3$ into silver carbonate (Ag_2CO_3), which subsequently reacts to silver oxide (Ag_2O) under heating at 120°C in a nitrogen atmosphere (Figure 4.6 A,B, see appendix C for details). Following a similar photochemical scheme, we position a second coral shape next to the first one. Importantly, the precision of the photochemistry allows us to avoid precipitation on the earlier formed Ag_2O coral, while the low reactivity of Ag_2O prevents undesired ion-exchange with the carbonate and barium ions in the solution. After growing the second coral-shape, we convert it to $MnCO_3$, followed by thermal decomposition to Mn_2O_3 at 540°C in an aerobic atmosphere, thereby simultaneously reducing the silver oxide coral shape to metallic silver (Figure 4.6 A,C). Finally, a third coral shape is precipitated, equidistantly spaced next to the Ag and Mn_2O_3 corals. This coral is converted via basic cobalt carbonate into CO_3O_4, while leaving the earlier formed corals intact (Figure 4.6 A,D). EDS analysis confirms that only trace amounts of cross exchange has occurred, hence demonstrating that orthogonal sequences of photoinduced precipitation and cation-exchange reactions are possible (Figure 4.6 B-E).

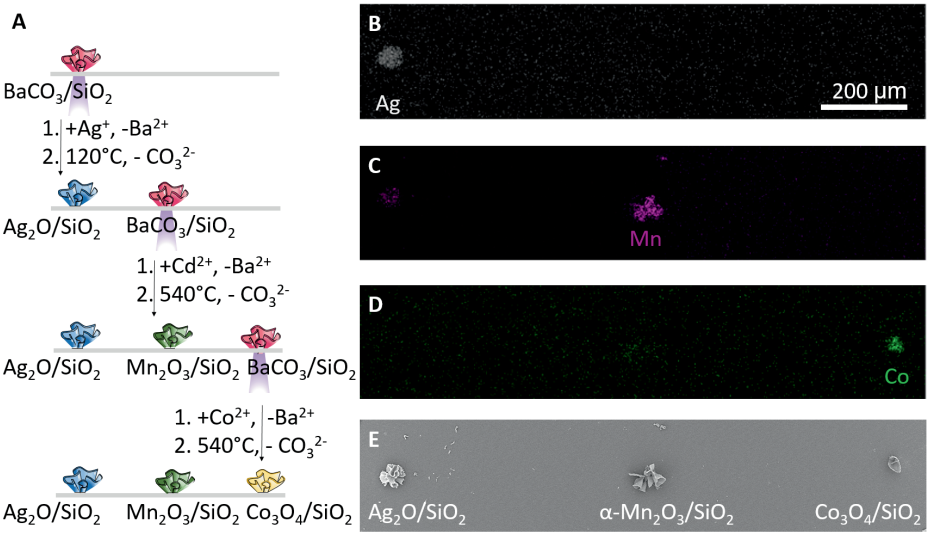

Figure 4.6: Orthogonal conversion reactions for positioning multiple chemical compositions. A) Reaction scheme for orthogonal cation exchange towards an array of Ag_2O/SiO_2, Mn_2O_3/SiO_2, and Co_3O_4/SiO_2 coral shapes. B-E) EDS-SEM analysis of the resulting structures showing selective cation exchange to B) silver (Ag); C) manganese (Mn); and D cobalt (Co).

While orthogonal cation exchange pathways can be designed based on thermodynamic stability, we find that orthogonal anion conversion pathways can be rationally planned following chemical reactivity. Specifically, we realize that many metal carbonates react towards metal sulfides at temperatures and partial H_2S pressures for which metal selenides remain unreactive for anion exchange. Moreover, many metal carbonates react to metal oxides at temperatures at which metal sulfides and selenides

remain unreactive. This suggests that orthogonal pathways for different anion reactions may be feasible.

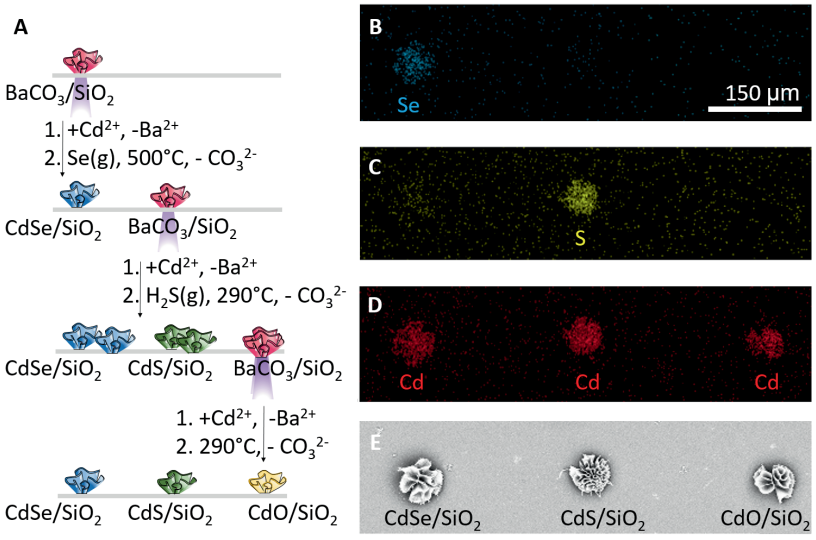

Figure 4.7: A) Reaction scheme for orthogonal anion exchange towards an array of $CdSe/SiO_2$, CdS/SiO_2, and CdO/SiO_2 coral shapes. B-E) EDS-SEM analysis of the resulting structures showing selective anion exchange to B) selenium (Se); C); sulfide (S); and D) cation exchange to cadmium (Cd). Note that oxide does not show up on EDS.

We exploit this insight by designing a pathway of orthogonal anion reactions to position coral shapes of cadmium selenide (CdSe), cadmium sulfide (CdS) and cadmium oxide (CdO) (Figure 4.8 A). We position a first coral shape and convert this coral to CdSe (Figure 4.8 A,B). We position a second coral shape next to the first one, and again convert this shape to $CdCO_3$. Subsequently these shapes are exposed to H_2S gas at 290°C. Under these reaction conditions, the CdSe remains unreactive, while EDS shows complete conversion of the $CdCO_3$ to CdS (Figure 4.8 A,C). Finally, we position a third coral shape at equidistant spacing of the already formed CdS and CdSe coral shape. Again, the $BaCO_3$ in the coral is converted into $CdCO_3$ and then heated to 290°C, which results in the conversion to CdO while leaving the CdS and CdSe structures unreacted. Hence, orthogonal anion reaction pathways can be designed by judiciously selecting sequences of reaction conditions.

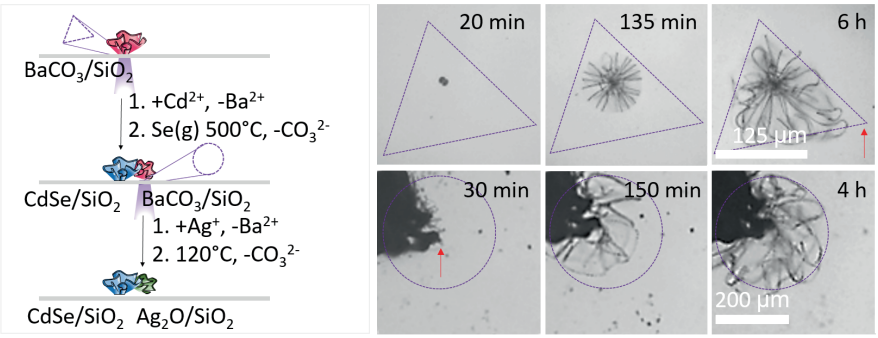

Figure 4.8: Integration of different compositions within a single nanocomposite. A) Reaction scheme for integration of Ag_2O/SiO_2 circle and $CdSe/SiO_2$ triangle shape via light-controlled assembly and orthogonal conversion reactions. B) Optical microscopy time-lapse showing the assembly of the triangle shape. C) Optical microscopy time-lapse showing the assembly of the circle shape after conversion of the triangle into $CdSe/SiO_2$. The red arrow in B and C indicates the same location.

The combination of spatiotemporal control over self-organization and orthogonal shape-preserving conversion reactions presents the opportunity for the creation of hybrid materials in which different nanocrystals of preselected chemical compositions are integrated within a single nanocomposite (Figure 4.9). We exploit these insights to form an integrated hybrid structure composed of a CdSe triangle and Ag circle (Figure 4.9 A-D). Using a photomask, we first induce growth of a triangular nanocomposite, which we convert to CdSe (see appendix C).

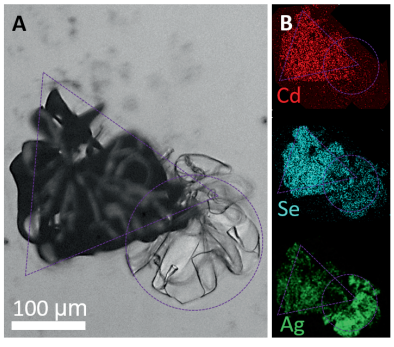

Figure 4.9: A) Optical microscopy image after conversion of the Ag_2O/SiO_2 circle and $CdSe/SiO_2$ triangle. B) EDS-SEM map showing confirming Cd and Se in the triangle and Ag in the circle.

We then project a circular UV-light pattern with a radius of 100 μm on the corner of the triangular shaped CdSe and induce nucleation. We observe new nucleation exclusively on top of the edges of the already grown and converted CdSe triangle, likely because exposed nanocrystals favor nucleation at these locations. We continue growth until the contours of the circle are filled. We subsequently convert the $BaCO_3$ in the circle to $AgCO_3$. Consistent with our orthogonal conversion scheme, the low

solubility product of CdSe prevents conversion of the triangle. Subsequent heating to 120°C results in the conversion of the circle to Ag_2O while the triangle remains CdSe, thus forming a shape-controlled hybrid structure (Figure 4.9 B).

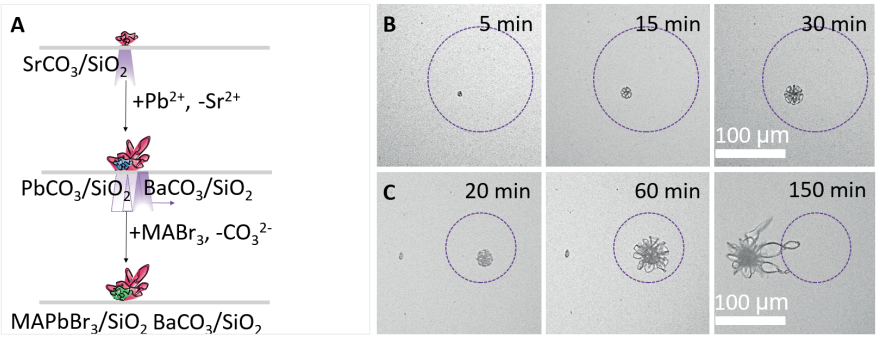

Figure 4.10: A) Reaction scheme for integration of $MAPbBr_3/SiO_2$ coral into an elongated $BaCO_3/SiO_2$ shape. B) Optical microscopy time-lapse showing the assembly of the $SrCo_3/SiO_2$ coral. C) Optical microscopy time-lapse showing the assembly of the elongated $BaCO_3/SiO_2$ structure by moving the UV spot away from the initial coral shape that is converted into $PbCo_3/SiO_2$.

The combination of spatiotemporal control and orthogonal chemistry can be used to integrate synergistic properties within a single architecture with independent control over shape and composition of the separate parts. Building upon our previous work with optical structures,[150] we demonstrate this potential by integrating a light-emitting lead methyl ammonium bromide perovskite ($MAPbBr_3$) semiconductor with a $BaCO_3/SiO_2$ shape that serves as optical waveguide (Figure 4.10). To form the light-source, we induce the nucleation and growth of a small coral-shaped nanocomposite. Instead of $BaCO_3$, we precipitate strontium carbonate ($SrCO_3$). $SrCO_3$ has similar properties as $BaCO_3$, but the smaller crystal lattice facilitates straightforward ion-exchange to perovskite precursor $PbCO_3$. We subsequently focus a 365 nm UV light top of the $PbCO_3/SiO_2$ structure and induce precipitation of $BaCO_3/SiO_2$. After 60 min, we move the UV spot to selectively direct the growth to one side into an elongated shape with a tip. Finally, we immerse the resulting structure into methyl ammonium bromide to convert the $PbCO_3$ into a methylammonium bromide perovskite semiconductor. SEM, EDS, and light microscopy using crossed polarizers confirm that lead is only present in the bottom part while the nanoscopic crystallographic alignment is lost, but the microscopic shape remains preserved (Figure 4.10 C, 4.10 A, see appendix C). The final architecture performs waveguiding of the light emitted from the perovskite core towards the tip of the elongated shape (Figure 4.11 B).

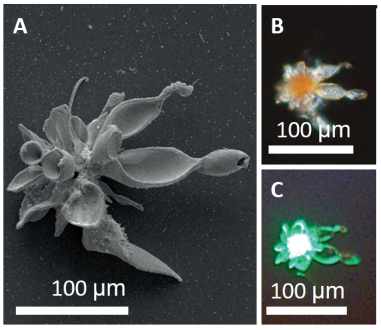

Figure 4.11: A) SEM of the final hybrid $BaCO_3/SiO_2$ composite with integrated light emitting $MAPbBr_3/SiO_2$ core. B) Polarized microscopy image, and C) fluorescence microscopy showing photoluminescence from hybrid $BaCO_3/SiO_2$ with light emitting $MAPbBr_3/SiO_2$ core.

4.3 Conclusion

We here demonstrate how light-driven self-organization processes and ion-exchange reactions can be combined to gain independent control over shape and composition. This two-step assembly/conversion strategy allows us to position, sculpt and hierarchically organize a wide range of metal oxides, metal sulfides and perovskites in user-defined designs. Complex hybrid architectures and landscapes of preassigned pallete can be formed by consecutively assembling and converting nanocomposites using orthogonal reaction pathways with independent control over shape and composition of each component.

Our assembly/conversion strategy takes advantage of fundamental features of self-organization. In traditional synthesis processes shape and composition are inherently entangled such that for each composition a new method is required to control the shape. In contrast, in our assembly/conversion strategy the self-organization process autonomously generates and orders nanoscopic building blocks. Because of this inherent nanostructure, these architectures subsequently can be converted into a wide catalogue of chemical compositions compositions independent of their initial shape. The nanocrystals offer enhanced chemical reactivity while the nanocomposite layout helps transport of reactants and offers mechanical stability to preserve the initial shape.

By decoupling the control of shape and composition, our multistep self-organization strategy gives spatiotemporal control over where which chemical composition is positioned. Photochemical reactions provide hands-on control over positioning and shaping, while orthogonal conversion pathways enable integration of different chemical compositions independent of their shape in sequential steps for the synthesis of complex hybrid components. This work adds to an expanding collection of self-organization strategies that have been coined non-covalent synthesis.[167,168] Akin to organic chemistry—in which covalent bonds are rationally designed at molecular scale using for instance protection groups, reactive centra and reaction cascades, we here are learning how non-covalent interactions can be precisely controlled at nano and microscale via multistep reaction pathways to shape, convert, orient and

construct increasingly complicated components and devices.

Indeed, we foresee that further control over the assembly/conversion scheme is possible. In particular, for the assembly step two-photon or light-sheet illumination schemes may offer refined control over the self-organization in three spatial dimensions. Moreover, for the conversion step, the continuously growing catalogue of conversion pathways[84,86,100,101,152,157,165]—which currently provide routes to more than fifty different chemical compositions including perovskites, metal chalcogenides and metals, that have desirable catalytic, photochemical or electronic functionalities—can be further expanded and refined.

Beyond these co-precipitation reactions, we anticipate that other self-organizing systems such as Liesegang inspired patterns and chemical gardens can be controlled using this assembly/conversion strategy.[152,156–159,169] Specifically, we believe that light induced chemical conversion can be developed, akin to classical photography techniques, to pattern different chemical compositions into preformed substrates. Also, assembly/conversion strategies can leverage the complexity and seemingly effortless control biomineralizing organisms. These conversion routes can already be used to convert biomineralized skeletons.[84,165,170,171] We foresee that biomineralization processes can be influenced and steered using light patterns using for instance IR.[163] These opportunities highlighting new pathways for advanced and functional components, with refined hands-on control when needed, and effortless self-organization when possible.

4.4 Experimental

Preparation precursor solution

Typically, the precursor solution is prepared by dissolving 6 mg (6 mM) ketoprofen (KP) (Fluorochem) and 87 mg (70 mM) DTAB (VWR) in an 4 mL aqueous solution containing 5.5 mg (11 mM) sodium metasilicate (Na_2SiO_3) (Sigma Aldrich) with the help of brief sonication. In another vial, 24.5 mg barium chloride dihydrate ($BaCl_2{\cdot}2H_2O$) (Sigma Aldrich) is dissolved in 2 mL degassed water (100 mM). The KP-DTAB-Na_2SiO_3 solution is added to the $BaCl_2$ solution to obtain the final precursor solution (20 mM $BaCl_2$, 9 mM Na_2SiO_3, 5 mM KP, and 56 mM DTAB). The final precursor solution is directly injected in a closed sample cell, made of two quartz substrates and a Viton® spacer (3 mm, 1.2 mL volume). To avoid any uptake of carbonate species from the air, all solutions are kept in nitrogen during preparation. In all precursor solutions, a minimum concentration ratio of 1:10 KP:DTAB is used to assure that both KP and the photoproduct remain dissolved.

Post-process analysis

After growth with the help of UV light, the sample cell is disassembled in degassed water and the substrates are carefully washed with acetone. SEM imaging is carried out using a FEI Verios 460. Raman spectroscopy is performed using a confocal Raman microscope (WITec, Alpha 300 R) with an EMCCD detector (Andor, Newton, DU970P-BVF-355). A 532 nm laser with a diffraction grating of 600 g mm^{-1} is used for excitation. The spectra are each 20 times averaged with an integration time of 1 s.

UV-irradiation Microscope

The custom-built setup used to induce nucleation and growth of the $BaCO_3/SiO_2$ nanocomposites, contains four main sections: two irradiation parts, a sample holder stage, and an imaging part. The two irradiation parts are placed opposite from each other, both another side from the sample holder stage. One irradiation part is placed below the sample holder stage and can switch between irradiation of 275 nm UV LED light or irradiation of a 1435 nm NIR laser diode. For the UV LED irradiation, a lens (Edmund Optics 84–337, focal length (f) = 20.0 mm) collects the light from a 275 nm mounted LED (Thorlabs M275L4, 80 mW output power). Custom-made photomasks placed after the collector lens are used to projected the light with the help of two UV anti-reflection coated plano-convex lenses (Thorlabs LA4148-UV, f = 50.0 mm) on the sample. For the NIR irradiation, the light of a fiber coupled 1435 nm laser diode (Alcatel A1948FBG, 180 mW output power) is collimated by a plano-convex lens (Thorlabs LA1422, f = 40.0 mm) and refocused with another plano-convex lens (Thorlabs LA1422, f = 40.0 mm) on the sample. The second irradiation part is placed above the sample cell holder and consist of a 365 nm mounted LED (Thorlabs M365L3, 1290 mW output power) light. After passing a photomask, the UV light is collimated with an uncoated N-BK7 plano-convex lens (Thorlabs LA1422, f = 40.0 mm) and guided via a dichroic mirror (Thorlabs DMLP425R, long pass (lp) 425 nm) through a 10X/0.30 magnification objective (Nikon Plan Fluor) to focus the light on the sample. The sample holder stage consists of a custom-made temperature cell, controlled by a bath and circulation thermostat (Huber CC-K6), on top of a motorized translation table, provided by piezo inertia actuators (Thorlabs PIAK10). The imaging part contains a cold white light mounted LED (Thorlabs MCWHL5) and is placed above the 365 nm LED. The light is collected by an aspheric lens (Thorlabs ACL2520U-DG6-A, f = 20.0 mm) and guided by a 10:90 beamsplitter (Thorlabs BSN10R) to the same pathway as the 365 nm light, passing the dichroic mirror and the 10X/0.30 magnification objective to the sample. The reflected light is collected with the same objective lens and transmitted through the beamsplitter. A tube lens (Thorlabs AC254-200-A-ML, f = 200.0 mm), focuses the light on a CMOS camera (Basler Ace acA1920-40gc) for imaging. The light intensities of the UV LEDs and the NIR laser diode are controlled by neutral density (ND) filters (Thorlabs NDUV-B), as well as by adjustments of the driving current of the drivers (Thorlabs LEDD1B and Thorlabs CLD1015 for the LEDs and the laser diode, respectively). A handheld power meter (Thorlabs PM160T) is used to determine the used light intensity (I_{UV} in $\mu W\ mm^{-2}$), where the recorded power of the collected UV light is divided by the area of the sensor.

Conversion reactions

See appendix C for details.

Chapter 5

Light-driven nucleation, growth, and patterning of biorelevant crystals using resonant near-infrared laser heating

Abstract

Spatiotemporal control over crystal nucleation and growth is of fundamental interest for understanding how organisms assemble high-performance biominerals, and holds relevance for manufacturing of functional materials. Many methods have been developed towards static or global control, however gaining simultaneously dynamic and local control over crystallization remains challenging. Here, we show spatiotemporal control over crystallization of retrograde (inverse) soluble compounds induced by locally heating water using near-infrared (NIR) laser light. We modulate the NIR light intensity to start, steer, and stop crystallization of calcium carbonate and laser-write with micrometer precision. Tailoring the crystallization conditions overcomes the inherently stochastic crystallization behavior and enables positioning single crystals of vaterite, calcite, and aragonite. We demonstrate straightforward extension of these principles toward other biorelevant compounds by patterning barium-, strontium-, and calcium carbonate, as well as strontium sulfate and calcium phosphate. Since many important compounds exhibit retrograde solubility behavior, NIR-induced heating may enable light-controlled crystallization with precise spatiotemporal control.

This chapter is based on Bistervels, M. H., Antalicz, B., Kamp, M., Schoenmaker, H., & Noorduin, W. L. (2023). Light-driven nucleation, growth, and patterning of biorelevant crystals using resonant near-infrared laser heating. *Nature Communications*, 14 (1), 6350.

5.1 Introduction

Controlling crystallization at the right place and at the right time is at the core of how organisms organize minerals into complex architectures with superb performance.[5,9,69,160,172,173] For instance, biominerals of calcium carbonate and calcium phosphate crystallize into hierarchical structures such as dental enamel,[1] nacre for creating materials with high resilience and hardness,[174] and crystallographically well-ordered calcite crystals in starfish tentacles for compounded vision.[4,6,175] Gaining such spatiotemporal control over crystallization offers opportunities for probing, steering, and understanding crystallization phenomena in organisms, and enables the development of artificial materials with advanced functionalities.[3,132,133,176–179] Already, many techniques such as self-assembled monolayers,[65,180] microfluidic devices,[76,181] confined spaces,[182,183] (anisotropic) templates,[63,170,184] topographical substrates,[185,186] or additives,[30,53] have been developed to achieve control over crystallization in either space or time, but controlling both simultaneously remains challenging.[187]

From this perspective light-induced reactions offer the potential to gain spatiotemporal control over crystallization by modulating light intensities with (sub)micrometer resolution and microsecond dynamics.[23,24] Photochemical reactions have been used to control assembly and nucleation of colloidal and mineral systems by using for instance photoswitches,[188,189] photoacids/bases,[22,117] and photodecarboxylation,[153] that steer local interactions or local gradients. However, these photochemical reactions require complicated chemical mixtures of photoreactants, photoproducts, and stabilizing agents such as surfactants; all of which can inflict undesired disturbance of both crystal nucleation and growth.[121] Alternatively, non-photochemical processes have been explored to induce crystallization in solutions, thin films, and glasses.[123,190,191] But the need for complicated pulsed lasers set-ups, special crystallization media, or large minimal irradiation area (typically mm^2) in combination with the inherent stochastic nature of nucleation has so far restricted the application potential and the spatial control.[124] Moreover, the limited understanding of the underlying principle has so far prevented further rational extension of these methods.[130] Unlocking the full potential of light-controlled crystallization processes thus requires a radical new approach to overcome the need for complicated mixtures that disturb crystal nucleation and growth, while at the same time offering generalizable principles with precise spatiotemporal control.

From this perspective, near-infrared (NIR) laser light provides interesting opportunities. NIR laser light enables local heating of water by resonating with the first overtone of the O-H stretch vibration (Figure 5.1), and is routinely used to manipulate biological processes such as protein kinetics and DNA folding,[192,193] and NIR light-triggered release of payload from polymeric capsules.[194] In contrast, we here explore NIR laser light to induce crystallization with precise spatiotemporal control while circumventing the need to use special crystallization media or additives. Our strategy for controlling crystallization using NIR is motivated by two key insights: (i) many biorelevant minerals (e.g. calcium carbonates[195] and calcium phosphates[196]), and many technologically important crystals (e.g. lead halide perovskite semiconductors[197]) exhibit a retrograde solubility, i.e. the solubility of these compounds decreases for increasing temperatures. (ii) NIR laser light has been shown to locally heat up water with 50°C in a 10 micrometer diameter light spot within milliseconds, suggesting great potential for locally increasing the supersaturation and thereby inducing crystallization of retrograde soluble minerals with precise

spatiotemporal control without any need of additives.[193]

Motivated by this analysis, we develop an NIR optical setup to locally induce crystallization of compounds with an inverse solubility. By tuning the crystallization conditions and light settings we demonstrate the following levels of spatiotemporal control in user-defined micrometer patterns for metal carbonates: (1) writing of $CaCO_3$ crystals in microscopic user-defined patterns; (2) refining the resolution for nucleation and growth of single crystals; (3) extending NIR-induced crystallization with spatiotemporal control towards three polymorphs of $CaCO_3$ (vaterite, aragonite, calcite), and other biorelevant carbonate, phosphate and sulfate salts with retrograde solubilities, to demonstrate the generality and sequential control for multimaterial patterning.

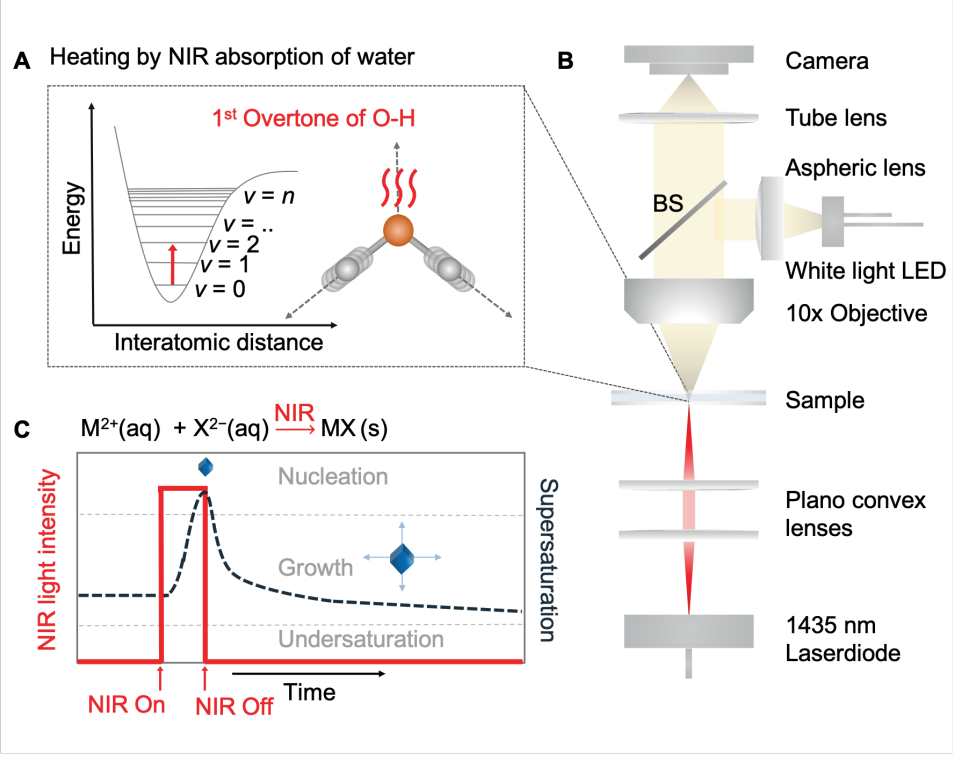

Figure 5.1: Resonant NIR laser heating for light induced crystallization. A) Light absorption of NIR (1435 nm) by the first overtone of the O-H stretch vibration of water results in local heating. B) Optical setup in which NIR laser light is focused on the bottom (ITO coated) glass substrate of a reaction cell filled with the precursor solution to locally induce crystallization. Using white light, the process is monitored in-situ. C) Local heating by NIR light (red line) increases the local supersaturation of salt with retrograde solubility MX (dashed black line) to induce crystallization (blue rhombohedron).

5.2 Results and discussion

Crystallization conditions for NIR laser writing

To control crystal nucleation and growth, we develop a custom-built optical set-up that combines NIR laser light irradiation with in-situ monitoring (Figure 5.1 B, C). For the NIR laser light irradiation, we focus a fiber-coupled high intensity laser diode of 1435 nm (spot radius 15 µm) on a temperature-controlled and motorized reaction cell holder. The reaction cell is composed of two glass substrates, which are a separated by a Viton® spacer. The cell is filled with an aqueous precursor solution containing the desired metal carbonate, and the reaction cell is placed in the sample holder. For in-situ monitoring, we use a conventional white light LED in combination with an objective and CMOS camera opposite from the focal spot.

We quantify the spatial temperature change upon NIR laser irradiation by monitoring the temperature dependent emission of the photoacid 8-hydroxypyrene-1,3,6-trisulfonate trisodium (HPTS) (Methods and appendix D Note D and Figure D.1).[198] We find that the solution temperature increases approximately linearly as function of the NIR laser power (Figure 5.2 A). Moreover, we also observe that the local solution temperature changes within seconds of switching the laser on or off (Figure 5.2 B), while spatial temperature mapping shows that the heating effect remains localized in the direct vicinity of NIR laser spot (Figure 5.2 C).

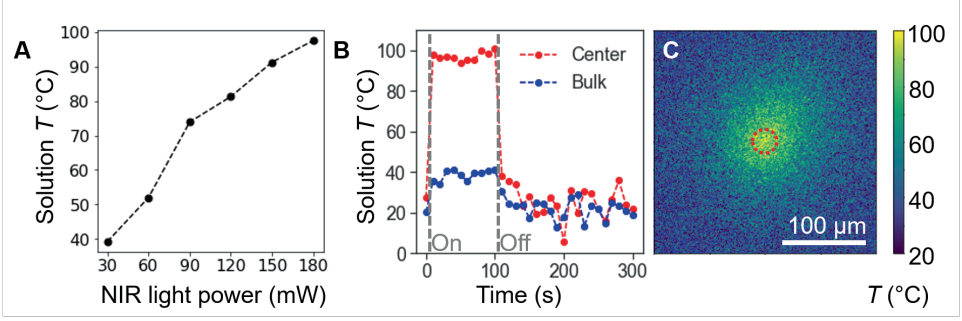

Figure 5.2: Quantification of the spatial temperature change upon NIR laser irradiation. A) Interfacial temperature measurement for a glass substrate, obtained by monitoring the dual-band emission of HPTS, showing the solution temperature in the NIR focal point as function of the incident NIR laser power. B) Solution temperature upon modulation of the NIR power from 0 to 180 mW NIR irradiation over time for the beam center (red dots) and bulk solution measured 150 µm away from the NIR focal point (blue dots). The NIR was turned on and off manually after 10 and 110 s respectively. C) Temperature map around the NIR focal point (indicated by red dashed circle) with 180 mW light intensity (pixel size 0.375 µm). G) Schematic showing that moving the NIR focal spot (red) results in nucleation and growth of a line of crystals with retrograde solubility on an ITO coated glass substrate. H) In-situ optical microscopy time-lapse showing that moving the NIR laser spot induces local precipitation of $CaCO_3$. I) Backscatter SEM image of a NIR laser-written substrate of calcite crystals following a user-defined pattern, with red inset. J) Showing agglomerates of $CaCO_3$ organized in intersecting lines on an ITO-coated substrate.

To locally induce nucleation of $CaCO_3$ within the NIR focal spot, we screen the parameters that determine nucleation. We vary in precursor concentrations, additives and surface free energy and monitor how the solutions react on the NIR laser light irradiation (appendix D, Figure D.2). To prevent nucleation in the bulk solution we increase the nucleation time by adding 100-300 mM NaCl to the precursor

solution, which is known to suppress high nucleation rates by reducing the activity coefficients of the precursor ions.[199] Moreover, to promote local nucleation in the laser spot, we use glass slide coated with indium tin oxide (ITO) that absorbs the NIR laser light (appendix D, Figure D.3) and thereby additionally heats up the substrate precisely in the NIR focal spot. Notably, we observe flow towards the focal spot, which can further support local crystallization by mass transport. Using these insights, we identify an optimum concentration range of calcium chloride salt ($CaCl_2$ 0.5-5 mM), and sodium carbonate salt (Na_2CO_3, 0.5-2 mM) in a pH adjusted solution using sodium hydroxide (NaOH, pH 10.7) that gives a metastable precursor solution, in which crystals nucleate only in the NIR irradiated spot.

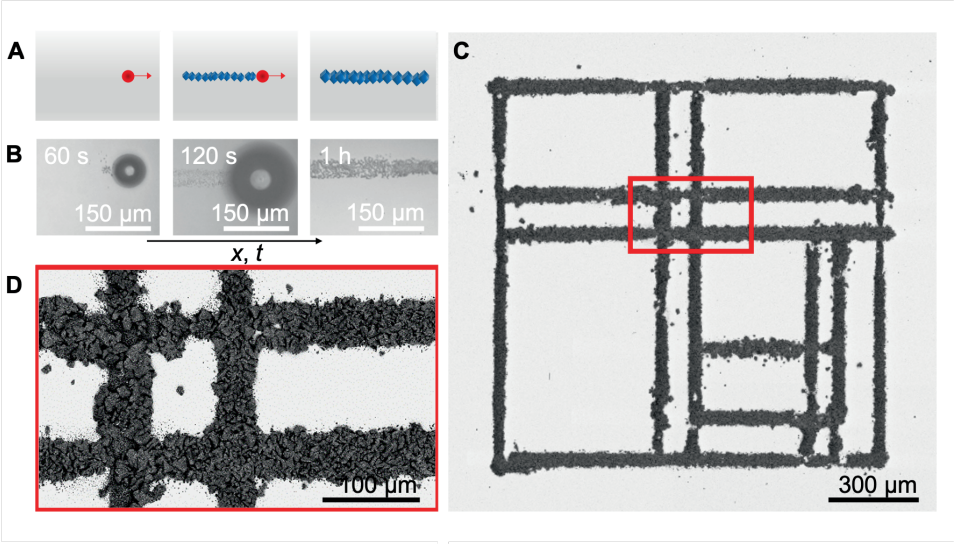

Figure 5.3: Laser writing of crystals with resonant NIR laser heating. A) Schematic showing that moving the NIR focal spot (red) results in nucleation and growth of a line of crystals with retrograde solubility on an ITO coated glass substrate. B) In-situ optical microscopy time-lapse showing that moving the NIR laser spot induces local precipitation of $CaCO_3$. C) Backscatter SEM image of a NIR laser-written substrate of calcite crystals following a user-defined pattern, with red inset. D) Showing agglomerates of $CaCO_3$ organized in intersecting lines on an ITO-coated substrate.

Based on these findings, we laser-write crystals with a moving NIR focal spot on a substrate (Figure 5.3 A, B). We prepare a reaction cell of ITO coated glass substrates containing a precursor solution (1.5 mM $CaCl_2$, 1 mM Na_2CO_3, 200 mM NaCl, pH 10.7). To induce crystallization, we switch on the NIR laser light (> 120 mW) to locally heat up the solution and thereby increase the local supersaturation such that nuclei form in the laser spot. Although not necessary for nucleation, we often observe the formation of gas-bubbles in the NIR spot, likely due to local boiling of water.[194] When the NIR spot is moved away from the nuclei, these nuclei continue growing into typical rhombohedron calcite crystal while no new nuclei form outside of the NIR spot, which confirms that the precursor solution is supersaturated within the metastable zone for nucleation. Using a pace of 17.5 µm s^{-1} and a light intensity of 180 mW for the NIR laser light, we write a line of crystals with a width of 30 µm into an abstract microscopic pattern (Figure 5.3 C, D).

Light-driven nucleation of single crystals

The NIR laser-induced nucleation offers the opportunity to overcome the stochastic nature of crystallization and form a single crystal of $CaCO_3$ in the NIR focal spot (Figure 5.4).

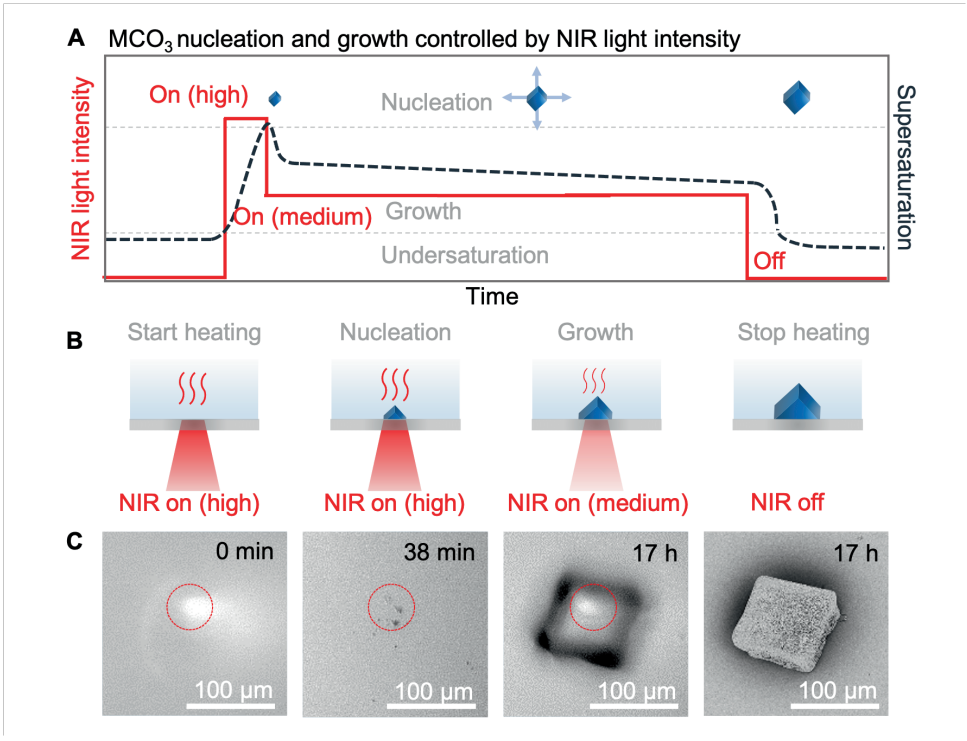

Figure 5.4: NIR laser-induced nucleation and growth of single calcite crystals with spatiotemporal control. A) Schematic for modulation of the NIR laser light intensity enables separation of nucleation and growth of the retrograde soluble carbonate salts (MCO_3). B) Nucleation of a single calcite crystal by modulating the NIR laser light intensity. High NIR laser light intensity is used to induce nucleation. Lowering the NIR laser light intensity allows growth during NIR laser light irradiation of a single calcite crystal while avoiding new nucleation. C) In situ optical microscopy time-lapse of a growing single calcite in the NIR focal spot (indicated by red dashed lined circle), and SEM of the final crystal.

To achieve this precise resolution, we deliberately lower the nucleation rate by preparing a slightly undersaturated precursor solution (1 mM Na_2CO_3, 0.5 mM $CaCl_2$, pH 10.7) and equilibrate for two days to suppress undesired spontaneous nucleation. Moreover, to lower the local heating upon irradiation, we replace the ITO-coated glass slides of the reaction cell for uncoated glass slides. Using high NIR laser light intensity (180 mW), we induce nucleation in the focal spot after 30 s (Figure 5.4 A-C). We then directly reduce the NIR laser light intensity (120 mW) to prevent undesired formation of new nuclei, while still enabling growth of the single crystal. After 17 h, we observe that the nucleus has grown into a calcite crystal in absence of new nuclei. Turning off the NIR laser stops the growth but is not followed by dissolution (appendix D, Figure D.4), indicating that the precursor solution is indeed only slightly undersaturated. Balancing the NIR laser light intensity and solution concentrations thus enables nucleation and growth of a single calcite crystal with spatiotemporal control.

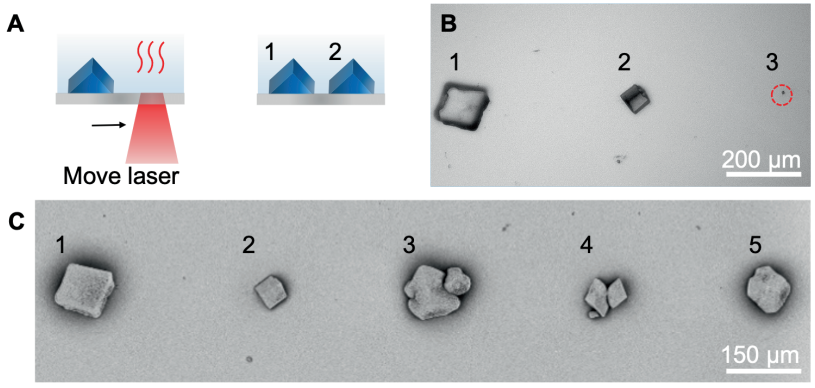

Figure 5.5: Succesive NIR laser-induced nucleation and growth of single calcite crystals with spatiotemporal control. A) Schematic of moving the NIR focal spot on the substrate. B) Optical microscope image of successive nucleation of single calcite crystals, with different sizes dependent on their irradiation (appendix D, Movie D), indicated by numbers 1–3. C) SEM image of resulting crystals, indicated by numbers 1–5.

We exploit the spatiotemporal control to position multiple crystals next to each other with micrometer precision. To induce the nucleation and growth of a neighboring $CaCO_3$ crystal, we move the NIR focal spot 300 µm next to an already grown single calcite crystal (Figure 5.5 A). Because the precursor solution becomes slightly depleted by precipitation, we observe a trend of longer nucleation times and lower growth rates for later grown crystals. To regain the nucleation and growth rate, we adjust the irradiation time or laser light intensity and sequentially position a line of crystals (Figure 5.5 B, C, appendix D, Movie D), highlighting the level of spatiotemporal control that can be achieved with our NIR pattering strategy.

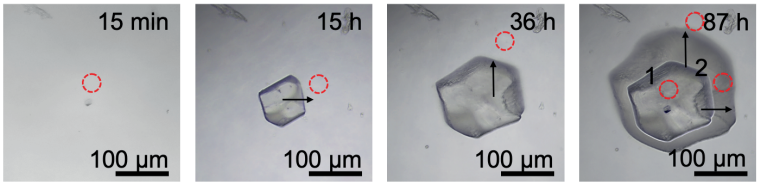

Figure 5.6: Spatiotemporal control over crystal growth of a calcite crystal. After nucleation of calcite (15 min), the NIR laser spot (red dashed circle) is initially moved to the right (15 h) and subsequently to the top (36 h) of the center of the crystal to enhance the growth rate of crystal facets in the direction of the NIR laser spot. Overlay of the timelapse photographs of the asymmetric growing crystal with the positions of the NIR spot at (1) 1 h, (2) 35 h, and (3) 87 h.

The spatiotemporal control over the supersaturation suggests that NIR-induced crystallization may be used to modulate the growth rate of different crystal facets. To explore this potential, we induce the nucleation and growth of a single calcite crystal using NIR irradiation (Figure 5.6). Subsequently, we move the NIR focal spot away from the crystal center to favor the growth in one direction. We observe

that all facets of the crystal continue growing, however the facets in the vicinity of the NIR spot grow significantly faster. Hence, NIR can be used to control the growth rate of different crystal facets and thereby steer the crystal morphology.

Light-driven crystallization of $CaCO_3$ polymorphs

We test whether NIR laser-induced crystallization is compatible with previously developed methods of polymorph control.[199] Although it is well-known that additives and/or heat both can be used to influence the crystal structure of $CaCO_3$, it is unclear if NIR heating in combination with additives enables control over both the position and crystal structure. We examine this potential by growing the three $CaCO_3$ polymorphs calcite, aragonite and vaterite in a triangular pattern (Figure 5.7).

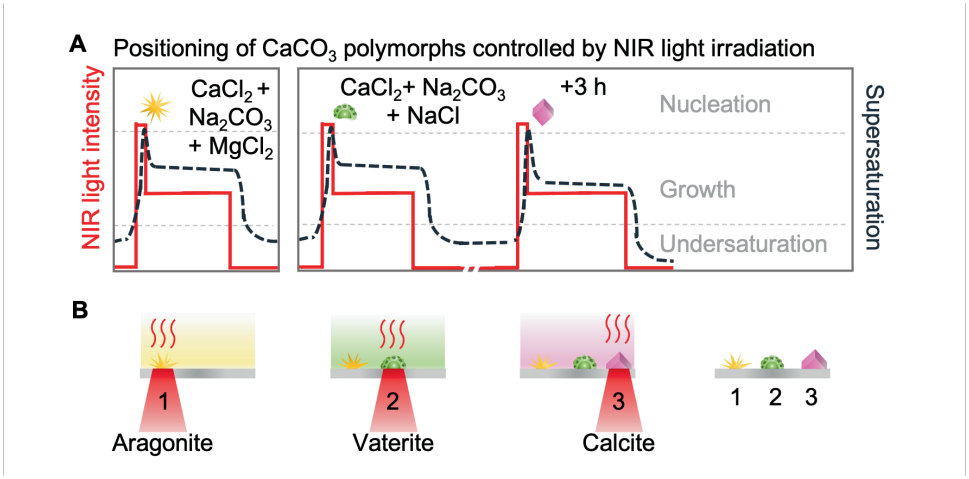

Figure 5.7: NIR controlled positioning of different $CaCO_3$ polymorphs on the same substrate. A) Schematic overview of the NIR light schedule (red solid line) and corresponding supersaturation (black dashed line) using NIR irradiation on a $CaCO_3$ growth solution complemented with $MgCl_2$ or NaCl at different times.B) Modification of crystallization conditions induces nucleation and growth of aragonite (yellow, addition of $MgCl_2$), vaterite (green, addition of NaCl and direct irradiation of freshly prepared precursor solution), and calcite (pink, addition of NaCl and irradiation of 3 h equilibrated precursor solution) with micrometer spacing.

To enable the growth of aragonite, we use $MgCl_2$ as additive, which is known to favor the formation of aragonite, to the $CaCO_3$ precursor solution (2 mM $MgCl_2$, 1 mM $CaCl_2$, 1 mM Na_2CO_3, pH 10.7), and load a reaction cell composed of glass substrates (Figure 5.7 A,B). Indeed, upon irradiation to induce nucleation and growth (5 s 180 mW, 1 h ramping from 80 to 150 mW) we observe needle-like aragonite crystals within the NIR focal spot. Next, we exploit the stability of $CaCO_3$ to first induce the formation of vaterite and subsequently calcite next to the grown aragonite. We refill the reaction cell with a freshly prepared $CaCO_3$ precursor solution (300 mM NaCl, 1.5 mM $CaCl_2$, 1 mM Na_2CO_3, pH 10.7). We enable the nucleation and growth of a single vaterite crystal upon the first NIR laser light irradiation (30 s 180 mW, 30 min, 120 mW respectively). Subsequently, we allow the solution to equilibrate (3 h), after which we reposition the NIR focal spot and induce the nucleation and the growth of a single calcite (2 min 150 mW, 1 h ramping from 90 to 130 mW). Scanning Electron Microscopy (SEM) imaging and Raman spectroscopy confirm that each crystal is completely formed of the desired polymorph (Figure 5.8 A-E

and appendix D Figure D.5).[200] Hence, despite the local temperature gradients we find that additives in the precursor solution can still determine the crystal structure during NIR-induced crystallization, to enable patterning of different single crystal polymorphs with micrometer precision.

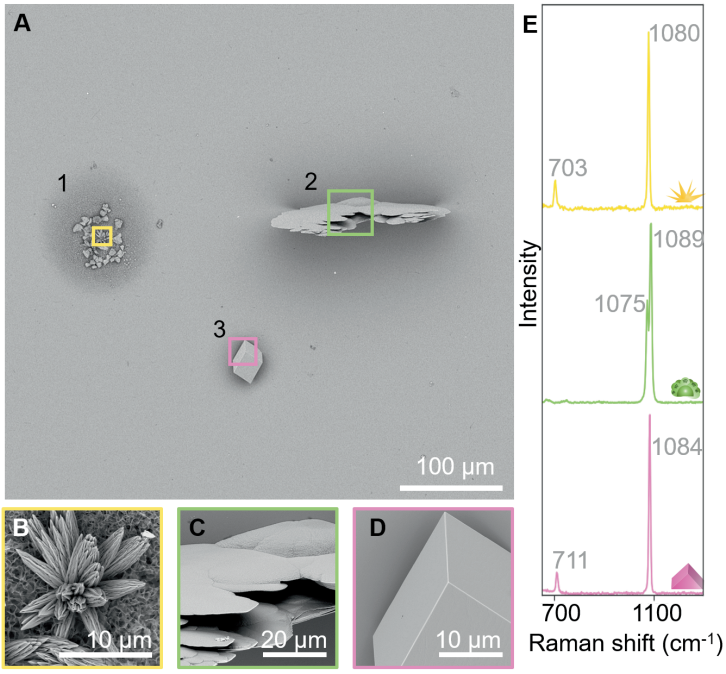

Figure 5.8: Resulting crystals of NIR controlled positioning of different $CaCO_3$ polymorphs on the same substrate. A) SEM image of the three different polymorphs positioned in a triangular pattern. B–D) High magnification SEM images of the three polymorphs. E) Raman spectra of the three polymorphs, as indicated by the corresponding color lining, yellow (aragonite), green (vaterite), pink (calcite), of the SEM images and schematic growth solutions.

Light-driven crystallization of other biorelevant minerals

The principle of resonant NIR laser heating-controlled crystallization can readily be extended to a wide range of other compounds with retrograde solubility. To demonstrate this generality, we position metal carbonate crystals (MCO_3) of barium carbonate ($BaCO_3$), strontium carbonate ($SrCO_3$), and $CaCO_3$—all of which have retrograde solubilities—next to each other on a glass substrate.[195,201,202] Similar to the $CaCO_3$ precursor solution, we identify the optimum precursor concentration range by in-situ monitoring of the precursor solution upon modulation of the NIR laser light intensity (Figure 5.9). Since $SrCO_3$ and $BaCO_3$ spontaneously nucleate rather rapidly, we observe that the nucleation occurs with more stochastic fluctuations. Again, we stabilize the precursor solutions by adding NaCl. To crystallize $BaCO_3$, we fill the reaction cell with the $BaCO_3$ precursor solution (300 mM NaCl, 0.75 mM $BaCl_2$, 0.75 mM Na_2CO_3, pH 10.7) and enable nucleation and growth of $BaCO_3$ upon NIR laser light irradiation (5 min 180 mW, 50 min 180 mW). Subsequently, the reaction cell is flushed with water, and refilled with a $SrCO_3$ precursor solution (75 mM NaCl, 0.5 mM $SrCl_2$, 0.25 mM Na_2CO_3, pH 10.1). We move the NIR

focal spot 300 µm next to the $BaCO_3$ crystals and modulate the NIR laser light intensity to induce nucleation and growth of $SrCO_3$ (2 min 180 mW, 45 min 160 mW). Lastly, the reaction cell is again flushed with water, and refilled with a $CaCO_3$ precursor solution (300 mM NaCl, 1 mM $CaCl_2$, 1 mM Na_2CO_3, pH 10.7) to enable nucleation and growth of $CaCO_3$ 300 µm next to the other side of the $BaCO_3$ crystals (1 minute 180 mW, 1.5 h 50 mW). SEM and Raman spectroscopy confirm the positioning of the three different MCO_3 crystals with micrometer precision (Figure 5.9 B, C, and appendix D Figure D.6).[203]

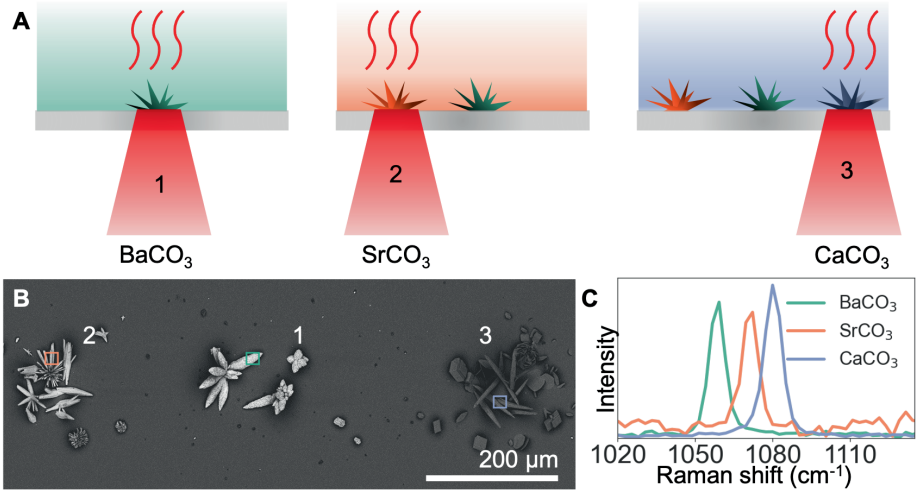

Figure 5.9: Spatiotemporally controlled nucleation of different retrograde soluble crystals using NIR laser light. A) Schematic for NIR-controlled nucleation of $BaCO_3$ (green), $SrCO_3$ (orange), and $CaCO_3$ (purple). B) SEM image of the resulting NIR-induced nucleation of MCO_3 crystals positioned in a line. C) Raman spectroscopy of the MCO_3 crystals in (B), showcasing the counterion-specific shift of the symmetric stretching vibration of carbonate ions.

To combine the different levels of NIR laser-induced controlled crystallization, we laser write a pattern of multiple materials. We first fill a reaction cell composed of ITO-coated glass substrates with a metastable precursor solution (1.5 mM $CaCl_2$, 1 mM Na_2CO_3, 200 mM NaCl, pH 10.7). We laser-write a line pattern of $CaCO_3$ nuclei using 180 mW NIR power and a moving focal spot with a velocity of 17.5 µm s^{-1}, and enable the nuclei to grow into crystals for 24 h. To fill in the framework with $SrCO_3$ crystals, we wash the cell twice with water and refill the reaction cell with a $SrCO_3$ precursor solution (200 mM NaCl, 1 mM $SrCl_2$, 0.5 mM Na_2CO_3, pH 10.7). Upon irradiation of 180 mW and a moving light beam of 8.5 µm s^{-1}, we induce the precipitation of $SrCO_3$ nuclei. Again, we leave the nuclei to grow in the solution for 24 h, and wash the substrate with water and ethanol. SEM with energy dispersion spectroscopy (EDS) mapping shows the hexagonal $SrCO_3$ crystals precisely positioned next to the rhombohedron $CaCO_3$ crystals without any overgrowth (Figure 5.9 D-F), which emphasizes the high spatial control that can be achieved using NIR laser-induced crystallization of multiple materials.

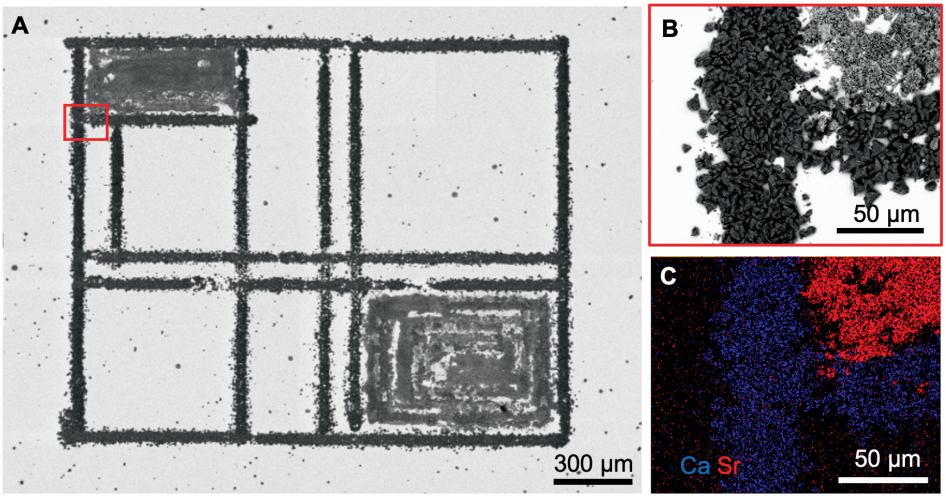

Figure 5.10: Laser-writing of various MCO_3 crystals. A) SEM image of NIR laser-induced drawing of $CaCO_3$ and $SrCO_3$, with B) high-resolution inset, and C) EDS map showing calcium (blue) and strontium (red).

Besides metal carbonates, many other biorelevant minerals such as metal sulfates and metal phosphates exhibit a retrograde solubility,[196,204] hence promising NIR as a more general approach for gaining control over crystallization. We explore this potential by NIR-induced formation of single crystals for two other biorelevant minerals: strontium sulfate and calcium phosphate. For both crystal systems, we modulate the NIR laser power to first induce nucleation at high laser power and subsequently sustain growth of a single crystal while avoiding new nucleation at low laser power. Specifically, for strontium sulfate we use an aqueous precursor solution containing 1 mM $SrCl_2$ and 1 mM Na_2SO_4 and induce nucleation using 3 min NIR irradiation with 180 mW NIR followed by 5.5 h with 130-150 mW to sustain growth (Figure 5.11). For calcium phosphate, we use an aqueous precursor solution of 1 mM $CaCl_2$ and 1 mM K_2HPO_4 and 300 mM NaCl to prevent formation of amorphous precipitate and induced nucleation using irradiation of 1 minute with 180 mW, followed by growth at 3 h with 130-180 mW to sustain growth (Figure 5.12). Raman spectra are in good agreement with the biomineral celestine for strontium sulfate and the bone mineral hydroxyapatite for calcium phosphate. SEM and EDS confirm the formation of single crystals of strontium sulfate and calcium phosphate (Figure 5.11 B-D, 5.12 B-D, and appendix D Figure D.7),[205,206] hence demonstrating the versatility and generality of NIR for inducing crystallization of retrograde minerals with spatiotemporal control.

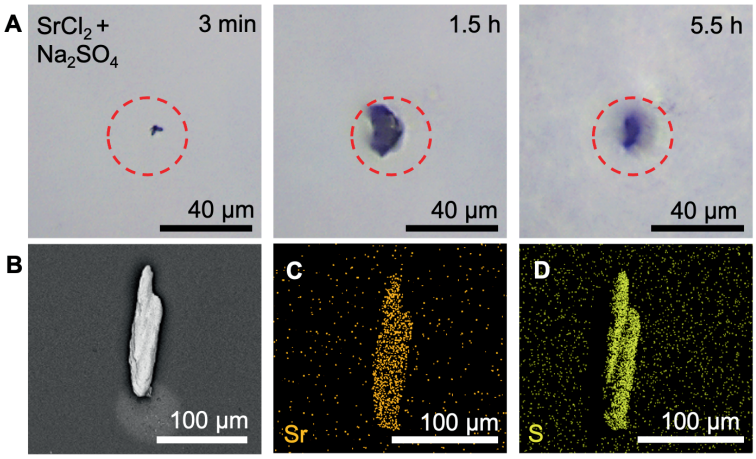

Figure 5.11: Spatiotemporal controlled crystalliozation of retrograde soluble strontium sulfate crystals using NIR laser light. A) Optical microscopy timelapse series showing the nucleation and growth of strontium sulfate with NIR (dashed red circle). B) SEM micrograph of the resulting mineral. EDS maps showing C) strontium (orange), and D) sulfur (yellow).

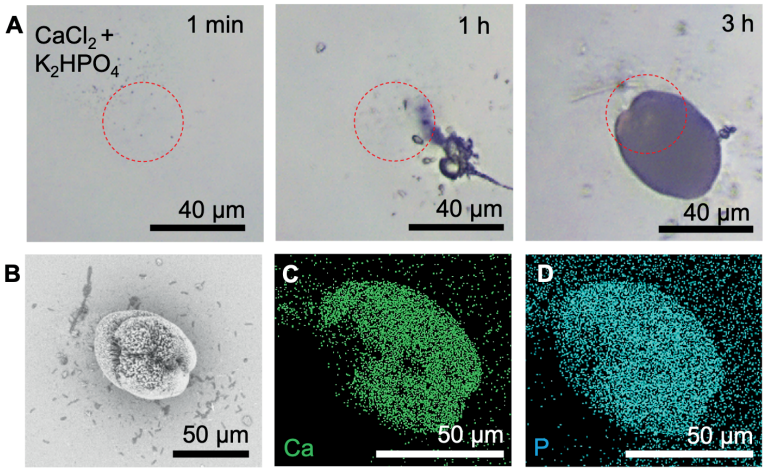

Figure 5.12: Spatiotemporal controlled crystalliozation of retrograde soluble calcium phosphate crystals using NIR laser light. A) Optical microscopy timelapse series showing the nucleation and growth of calcium phosphate upon irradiation with NIR (dashed red circle). B) SEM micrograph of the resulting mineral. EDS maps showing C) calcium (green), and D) phosphor (blue).

5.3 Conclusion

We here introduce resonant NIR laser heating for gaining precise user-defined spatiotemporal control over crystal nucleation and growth of compounds with retrograde solubilities. To demonstrate the proof-of-concept, we tailor precursor solutions and modulation of NIR laser light intensities to pattern various biorelevant retrograde soluble crystals with micrometer precision applied on both chemical composition and polymorphism.

The simplicity and versatility of our strategy makes NIR-induced crystallization accessible and implementable in widely used crystallization techniques. Importantly, control over the concentrations of the precursor solution and dynamic modulation of the light intensity provides a large parameter space for avoiding undesired spontaneous nucleation while also gaining an unprecedented level of spatiotemporal control over both nucleation as well as growth of crystals. In fact, we foresee that exploiting well-established crystallization techniques such as microfluidics, diffusion limiting gels or topographic confinements can even further improve the resolution. Additionally, higher laser powers and narrow focusing may further improve the resolution of the local heating. Furthermore, tuning the NIR wavelength enables resonant heating for a wide range of solvents, which extends the application potential of NIR-induced crystallization towards a broad class of desirable functional materials with retrograde solubility. For example, in case of perovskites, electrical heating already showed promising results for growing single crystals,[197] but the precise spatiotemporal control of NIR-induced crystallization can now be exploited to grow these widely studied semiconductors with exact control over shape and position. We foresee that NIR-induced crystallization may also be uniquely suitable for quantitatively controlling the local supersaturation and studying the role of local heating on crystallization dynamics and chemical reactions with spatiotemporal control. Furthermore, the narrow chemoselective absorption wavelength of NIR may enable synergistic combinations with orthogonal light-induced (photochemical) reactions, akin to double photochemical activation, for control over self-assembly in three dimensions.[207]

The principles presented here can readily be applied to a broad class of crystallization and self-assembling systems. Specifically, biominerals such as the bone component calcium phosphate and most common biomineral calcium carbonate have retrograde solubilities. In addition, NIR light is well-suited for bio-active applications due to its mild energy as compared to UV light,[193] thus opening the opportunity to manipulate mineralization processes in vivo. In artificial systems, we foresee that our optical setup for NIR heating can directly be used to exploit temperature dependent phase separations for light-directed assembly of nanoparticles, e.g. temperature sensitive assembling, into user-defined structures.[208] In addition, the metal carbonate salts that we use for the proof-of-concept can readily undergo ion-exchange reactions to yield a wide range of shape-controlled materials with desirable electronic, optical, and chemical properties such as semiconductors, metals, and catalysts.[86,101] By controlling the patterning of nucleation and growth, our work can also contribute and push boundaries in the area of hierarchical mineralization, which continues to be a major challenge in materials science. For instance, the precipitation of carbonate salts and silica may be directed using NIR defined light patterns to create highly complex microscopic three-dimensional nanocomposites according to exact designs.[150,209] This creates possibilities for steering the assembly of functional components such as optical components for directional emission and synthetic materials for regenerative medicine and

dentistry,[27,210] hence moving towards the magnificent micro- and nanoscopic control that organisms exert to form biominerals with exquisite performance.[13] In conclusion, NIR-induced heating offers unprecedented opportunities for light-controlled bottom-up manufactory of highly functional materials with user-defined control over position, size, shape and crystal structure.

5.4 Experimental

Preparation of precursor solutions

Stock solutions are prepared by dissolving the desired compound in degassed water: calcium chloride dihydrate ($CaCl_2{\cdot}2H_2O$) (Sigma-Aldrich) (28 mg, 19 mL, 10 mM), sodium chloride (NaCl) (Merck) (2340 mg, 80 mL, 500 mM), barium chloride dihydrate ($BaCl_2{\cdot}2H_2O$) (VWR) (25 mg, 10 mL, 10 mM), strontium chloride hexahydrate ($SrCl_2{\cdot}6H_2O$) (Sigma-Aldrich) (27 mg, 10 mL, 10 mM), magnesium chloride hexahydrate ($MgCl_2{\cdot}6H_2O$) (Sigma-Aldrich) (20 mg, 10 mL, 10 mM), sodium sulfate (Na_2SO_4) (Merck) (14 mg, 10 mL, 10 mM), potassium phosphate dibasic (K_2HPO_4) (VWR) (17 mg, 10 mL, 10 mM), and NaOH (VWR, pellets) (4 mg, 10 mL, 10 mM). 10 mM Sodium carbonate (Na_2CO_3) (Sigma-Aldrich) stock solution is prepared by dissolving 21 mg in 20 mL degassed water adjusted with NaOH stock solution to pH 10.7.

Typically, the precursor solution is prepared by freshly mixing 0–1.8 mL 500 mM NaCl stock solution with 150–1500 µL 10 mM MCl_2 stock solution, which then is added to 150–600 µL 10 mM Na_2CO_3, Na_2SO_4 or K_2HPO_4 stock solution. Then the pH is adjusted with 0–150 µL 10 mM NaOH stock solution and the solution is diluted with 0.15–2.55 mL degassed water to have a final total volume of 3 mL. The additive solution ($MgCl_2$) is first diluted with degassed water before added to the MCl_2 solution, which is then mixed with the Na_2CO_3 and NaOH solution to obtain a final total volume of 3 mL. After an equilibration time (0–48 h), the final growth solution is injected in a closed reaction cell, made of two (ITO-coated) glass substrates that were first ozone cleaned (10 min) and a Viton® spacer (2–3 mm spacing, 1.3–1.9 mL volume). After NIR-induced crystallization, the substrates are disassembled in degassed water and carefully washed with ethanol.

Custom-built NIR-irradiation microscopy

In the custom-built setup used for resonant infrared laser heating, three main parts can be identified: the NIR laser diode irradiation part, the reaction cell holder stage, and the imaging part. In the irradiation part, the output light of a fiber-coupled 1435 nm laser diode (Alcatel A1948FBG, 180 mW output power) is collimated by a plano-convex lens (Thorlabs LA1422, focal length (f) = 40.0 mm). After the collimation, the beam is refocused with another plano-convex lens (Thorlabs LA1422, f = 40.0 mm) on the sample. We control the light intensity by adjusting the driving current of the laser diode. The sample holder stage consists of a custom-made temperature cell on top of a motorized translation table. The solution temperature is controlled by a bath and circulation thermostat (Huber CC-K6). Motion control is provided by piezo inertia actuators (Thorlabs PIAK10) that have a typical step size of 20 nm. In the imaging part, the light of a mounted cold white light LED (Thorlabs MCWHL5) is collected by an aspheric lens (Thorlabs ACL2520U-DG6-A, f = 20.0 mm). A 10:90 beamsplitter (Thorlabs BSN10R) directs the light through a 10x/0.30 magnification objective (Nikon Plan Fluor) to the sample. The reflected images are collected with the same objective lens and transmitted through the beamsplitter.

With the help of a tube lens (Thorlabs AC254-200-A-ML), images are recorded by a CMOS camera (Basler Ace, acA1920-40gc).

Raman spectroscopy

Raman spectroscopy measurements are carried out using a confocal Raman microscope (Witec, Alpha 300R) with an EMCCD detector (Andor, Newton, DU970P-BVF-355). Excitation is performed with a 532 nm laser while spectra are collected in a spectrometer, equipped with a diffraction grating with a groove density of 600 grooves mm^{-1}. The spectra are each 20 times averaged with an integration time of 1 s.

Scanning electron microscopy

SEM imaging is performed using an FEI Verios 460.

Temperature measurements

For monitoring spatially-resolved interfacial temperature changes upon NIR laser irradiation, we developed a fluorescence-based experimental method that utilizes the two temperature-dependent emission bands of the photoacid 8-hydroxypyrene-1,3,6-trisulfonic trisodium salt (HPTS) (Sigma-Aldrich) that overlap with the green (G) and blue (B) channels of the CMOS sensor in our transmission microscope, allowing us to monitor their ratios without using a spectrometer. 5 mM HPTS solutions are prepared by dissolving 14 mg HTPS in 2.5 mL degassed water and 2.5 mL 1 M perchloric acid (Sigma-Aldrich). In our setup, we illuminate the solution with a low-intensity 400 nm LED from the same side as the NIR laser diode. We record the resulting fluorescence images with an RGB camera. To evaluate local temperature changes induced by the NIR laser heating, we construct a calibration curve, based on G:B intensity ratios recorded at different NIR heating power levels. To this aim, we heat the HPTS solution in the reaction cell with a bath and circulation thermostat (Huber CC-K6) to 83°C under the illumination of the 400 nm LED and record the RGB channels. Measurements are repeated with the same procedure for a reaction cell build of ITO-coated substrates. To measure the bulk temperature upon long NIR irradiation, a thermocouple is placed ca. 1 mm from the focal spot.

UV/vis/NIR absorption of glass and ITO

Steady-state external transmission measurements are carried out using a LAMBDA 750 UV/vis/NIR spectrophotometer (Perkin Elmer), equipped with a deuterium and tungsten excitation source, an InGaAs detector and an integrating sphere. The absorbance measurements are done for the range of 1000–1600 nm.

Chapter 6

Towards light-controlled nucleation and growth of self-assembling nanocomposites with three-dimensional spatial resolution

Abstract

Functional materials in Nature demonstrate that controlled three-dimensional (3D) self-assembly promises an innovative pathway for designing new artificial materials with desirable functionalities. Recent advancements have already initiated the generation of local gradients via photochemical reactions, but control over 3D morphologies is still challenging. This study explores the potential of non-linear two-photon absorption to gain spatial control over the co-precipitation of $BaCO_3/SiO_2$ microstructures in three dimensions. Using a 532 nm picosecond (ps)-pulsed laser setup, we aim to induce the photodecarboxylation of KP within a submicron focal spot. The laser-driven reaction yields local carbonate species which direct precipitation with unparalleled micrometer resolution. The selective activity in the focal spot enables controlled *z*-directional growth from an *x,y*-plane and the precipitation is amenable to ion exchange. While enhancements in balanced precipitation and structural stability are necessary, these findings underscore the potential for guiding 3D self-assembly, introducing novel perspectives for bioinspired advanced material creation.

6.1 Introduction

Controlled self-assembly processes constitute the fundamental mechanisms by which nature engineers materials with exceptional properties.[5,10,16,160,161,175] Mimicking these processes in synthetic self-assembly offers new routes for designing tailored three-dimensional structures with advanced functionalities.[27,37,183,211] The co-precipitation of $BaCO_3/SiO_2$ nanocomposites yields diverse morphologies such as vases, coral, and helical shapes.[80,83,87,93] Moreover, the resulting nanocomposites are modifiable for optoelectronic, magnetic, and electrical applications through post-functionalization methods such as surface modification[96,97] or ion conversion reactions.[84,86,100] Recent advances in photochemical reactions enable spatial and temporal control over the structure nucleation and growth with controllable light sources.[153,164] However, current control is mainly limited to a two-dimensional spatial plane due to direct light absorption in the solution. Therefore, achieving three-dimensional (3D) control demands innovative light-based techniques that surpass these limitations.

From this perspective, multiphoton induced reactions offer the potential to create an additional spatial dimension of light-controlled processes.[212–215] These reactions dependent on the absorption of two or more photons, enabling an exclusive reactivity in a single point of space. This presents a significant advantage compared to single-photon-induced reactions, where the reaction occurs indiscriminately anywhere within the laser beam. Sequential absorption of dual color wavelengths has been employed to achieve a 3D control of polymerization using photoswitchable photoinitiators. This results in a rapid fabrication of 3D shapes with micrometer resolution (Xolography). However, the necessity for molecular initiators reliant on two wavelengths hampers the extension of these principles to other systems. Alternatively, non-linear two-photon absorption has been investigated in 3D printing of photoresins, hydrogels loaded with nanocolloids, and photochemically adjusted colloidal nanocrystals, leading to the formation of microstructures of inorganic nanomaterials and colloidal nanocrystals.[212,216–220] While these techniques hold promise for aqueous crystal systems, the requirement for photosensitive media creates a complex interplay between photochemical mixtures and biorelevant crystallization. Consequently, achieving 3D light control using multiphoton absorption in crystal systems is recognized as a challenging, yet unexplored and unresolved area.

Drawing inspiration from these principles, we foresee that two-photon light techniques could offer enhanced control over the self-organizing $BaCO_3/SiO_2$ structures (Figure 6.1). Our strategy is driven by two key insights: i) Current 2D control relies on photochemical compounds activated by ultraviolet (UV) light emitted from conventional Light Emitting Diodes (LED) sources. Specifically, the photodecarboxylation of ketoprofen (KP) at 275 nm releases CO_2, creating a localized gradient that governs the co-precipitation.[153,154] ii) Two-photon absorption is a non-linear process demanding high intensities, typically achievable only within the focal spot of pulsed lasers, with negligible light-matter interaction beyond this zone.[215] This suggests that leveraging two-photon absorption of with high intensity 532 nm laser light could facilitate KP decarboxylation with three-dimensional precision, thereby inducing local nucleation and growth of $BaCO_3/SiO_2$ structures. Moreover, further advantages of the two-photon techniques are the low absorption in water and glass of the 532 nm, allowing for deeper penetration in aqueous samples and eliminating the need for specialized UV-optics.

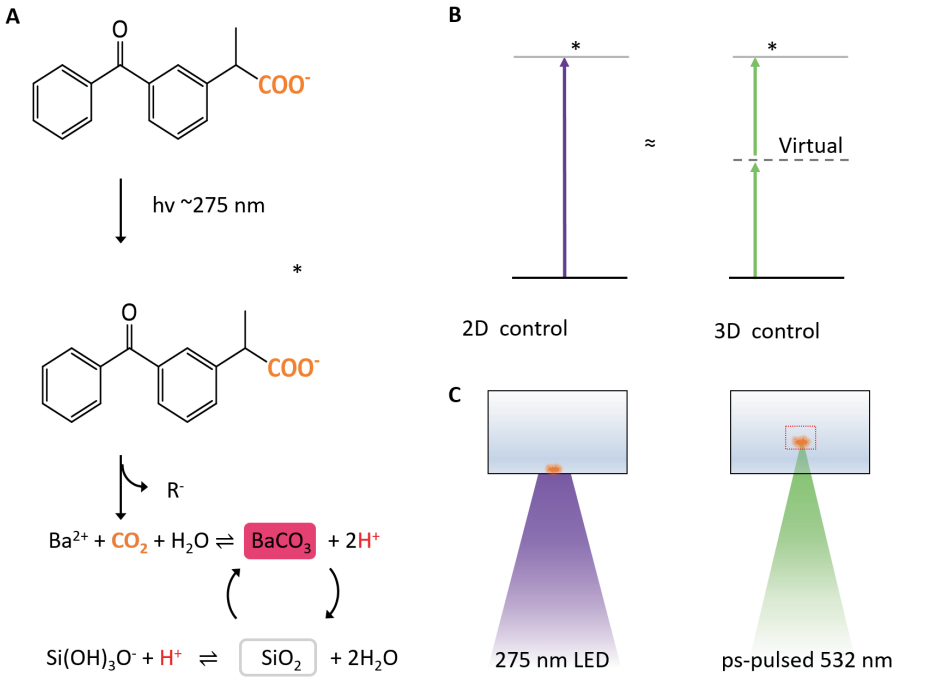

Figure 6.1: Concept of 532 nm laser-induced $BaCO_3/SiO_3$ co-precipitation with 3D spatial control. A) Upon irradiation of 275 nm ketoprofen releases CO_2 in its excited state. CO_2 activates and regulates the co-precipitation in a pH regulated feedback loop of $BaCO_3$ formation and Silica. B) The excitation energy of deep UV light equals the sum of two 532 nm photon via a virtual state. C) Schematic of experimental set-up. Deep UV light is directly absorbed by the solution, while ps-pulsed 532 nm yields only two-photon absorption in the focal spot.

In this study, we set the first steps towards achieving controlled nucleation and growth of $BaCO_3/SiO_2$ architectures in three dimensions, employing picoseconds (ps)-pulsed 532 nm laser light. We first explore the feasibility of inducing nucleation at a specific point in space through two-photon absorption, generating sufficient CO_2 locally, while systematically adjusting solution parameters to optimize precipitation conditions. We then leverage our findings to meticulously laser-draw lines of precipitation, containing partly $BaCO_3/SiO_2$ co-precipitation. Lastly, we demonstrate the opportunities in 3D directed self-assembly by using a moving laser beam, enabling the growth of a tower-shaped structure reaching a height of 175 µm, as well as the potential for converting the precipitation through ion exchange reactions. We anticipate that through further optimization, these results could pave the way for unprecedented developments in the realm of complex material design.

6.2 Results and discussion

To investigate the potential use of two-photon absorption in inducing photodecarboxylation of ketoprofen, we examine two ps pulsed laser set-ups at 532 nm, each varying in pulse duration and repetition rate. We prepare a solution of 20 mM barium chloride ($BaCl_2$), 9 mM sodium metasilicate (Na_2SiO_3), 5

mM ketoprofen (KP), 50 mM dodecyltrimethylammonium bromide (DTAB) and fill a reaction cell that consist of a 500 µm thick glass substrates spaced by a Viton® spacer. For both set-ups, we direct the laser onto the interior surface of the substrate and initiate laser irradiation. With the Teem-Photonics STG-03E-XSX laser that has a pulse energy of 2.5 µJ at a pulse rate of 2 KHz and a pulse length of 350 ps, we observe no activity. Conversely, when employing the frequency doubled Time-Bandwidth Lynx that has a 10000x higher pulse rate (10 MHz) and 1 nJ per pulse and a shorter than 10 ps pulse length, we detect activity in the form of numerous bubbles followed by precipitation. While the peak-power of the Time Bandwidth is lower than the Teem-Photonics laser it is still sufficient to enable the two-photon reaction. The reason no activity is seen with the higher peak power laser is most likely caused by the lower repetition rate and longer pulse length. We also observe that precise focusing and corrections for the glass substrate's thickness are imperative for activity induction within the precursor solution. This emphasizes the importance of the high power density in the laser spot required to trigger non-linear activity in the precursor solution.

We systematically examine the impact of 532 nm laser irradiation on the individual components within the solutions. Employing the 1 nJ, 10 MHz ps-pulsed laser equipped with 60X objective (NA 0.7, ELWD) that yields a focal spot diameter below 1 micron, we introduce various precursor combinations into the reaction cell (appendix E, Figure E.1- E.3). Upon irradiation, we exclusively observe bubble formation in the precursor solution containing KP. In solutions featuring both KP and MCl_2 (where M= Ca^{2+} , Sr^{2+}, or Ba^{2+}), coupled with high pH levels due to the presence of Na_2SiO_3 or adjustment with NaOH, we note substantial precipitation. Conversely, within KP solutions featuring a low pH (< 5) or lacking MCl_2, only a vague residue remains post-irradiation (appendix E, Figure E.4). Consequently, we confirm that the observed activity is primarily attributed to light interaction with ketoprofen and indicates photodecarboxylation.

Using these insights, we aim to enable local precipitation upon ps-pulsed 532 nm irradiation according to a user-defined pattern with micrometer resolution. We fill the reaction cell with a $BaCO_3/SiO_2$ precursor solution (20 mM $BaCl_2$, 9 mM Na_2SiO_3, 2.5 mM KP, and 25 mM DTAB). We focus the laser and start irradiation with full power (Figure 6.2). After we observe bubble formation and subsequent precipitation, we start to slowly move the sample cell. We notice that moving the sample cell too fast causes the precipitation and bubble formation to halt, while pausing the focal spot at one location yields a radial structural growth. Using a pace of approximately 1 µm s^{-1} with two stops (one overnight, one of 6 hours), we laser-draw with a width of 10 µm and achieve radial grown structures with a radius of 30 µm respectively.

We inspect the laser-induced precipitation and structural growth by scanning electron microscopy (SEM) (Figure 6.2 C, D). The precipitated line exhibits a blend of organic photoproducts, $BaCO_3/SiO_2$ co-precipitation, and unidentified shapes. In contrast, the radial structural growth distinctly resembles $BaCO_3/SiO_3$ co-precipitates. Additionally, both structures and the substrate feature extensive additional precipitation akin to previously observed polymerized silica and/or photoproducts.[81] Further analysis using Energy-dispersive X-ray spectroscopy (EDS) measurements demonstrates the presence of Barium in both the drawn lines and structures, accompanied by a notable Chloride content (appendix E, Figure E.5 and Figure E.6). Moreover, the silica content is approximately twice the Barium content in the drawn lines, whereas the EDS measurements report a 1:3 ratio at places in the radial structural growth, typical

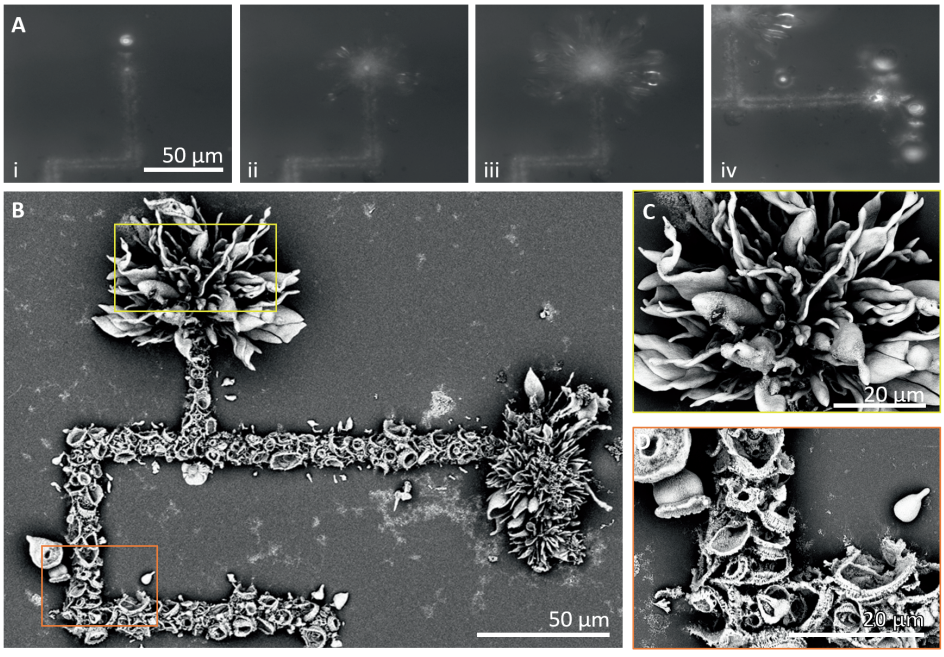

Figure 6.2: 532 nm laser-induced precipitation. A) Timelapse of laser irradiation with i) a moving beam, ii-iii) a static irradiating beam overnight, iv) a moving beam. B) SEM of irradiation, the lines of precipitation are due to a moving beam, the radial structural growth is due to a static irradiating beam with C) and D) insets that are indicated with color boxes in (B).

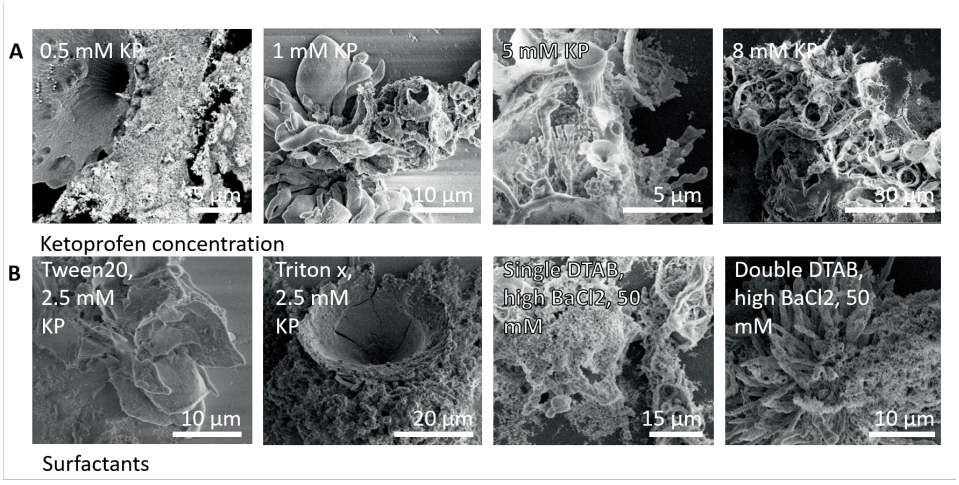

Figure 6.3: Screening of parameters to enhance 532 nm laser-induced precipitation A. Variations in A) ketoprofen concentration, a ratio 1:10 KP:DTAB molar concentration is kept, and B) surfactants.

for co-precipitation. Raman spectra provide a peak at 1058 cm^{-1}, which is characteristic for crystalline $BaCO_3$ (wurtzite),[203] but only for the radial structures grown at static laser irradiation (appendix E, Figure E.5). More to the center of the radial grown structures a strong peak around 830 cm^{-1} appears, which can indicate a silicate form.[221,222] Conversely, spectra from the precipitated line lack these peaks, showcasing instead peaks associated with disordered carbon as a broad band.[223]

The co-precipitation of $BaCO_3/SiO_2$ hinges on delicately balancing precipitation rates of both components and remains sensitive to minor interferences.[83,91] We realize that adjusting the precursor and laser parameters offers a pathway to augment local precipitation and mitigate excessive silica and photoproduct-like precipitates (Figure 6.3). Considering the presence of disordered carbon, which may indicate overly rapid precipitation, our initial strategy involves slowing down the reaction by reducing either the light intensity or the concentration of ketoprofen. Lowering the light intensity using neutral density filters yields some improvement, but rapidly results in no discernible activity (below an absorption (a) of 0.5, logarithmic scale), as the efficiency of these two-photon processes tends to scale with the square of the laser intensity. While varying the ketoprofen concentration, we note minimal effects. Though not optimal, concentrations ranging between 1-2.5 mM facilitate the most effective co-precipitation with fixed beam irradiation. Concentrations exceeding or falling below this range result in increased formation of both unidentified precipitation and excessive silica and photoproduct-like precipitates.

The extensive coverage with side products strongly suggests significant photoproduct formation or silica polymerization. To mitigate this issue, we investigate the efficacy of additional or altered additives and a reduction in silica content. A range of additives, including various cationic and anionic surfactants, radical scavengers, and wetting agents, are examined. Even before irradiation, sodium dodecyl sulfate (SDS) and the wetting agent 3-hydroxy(polyethyleneoxy)propyl heptamethyltrisiloxane,

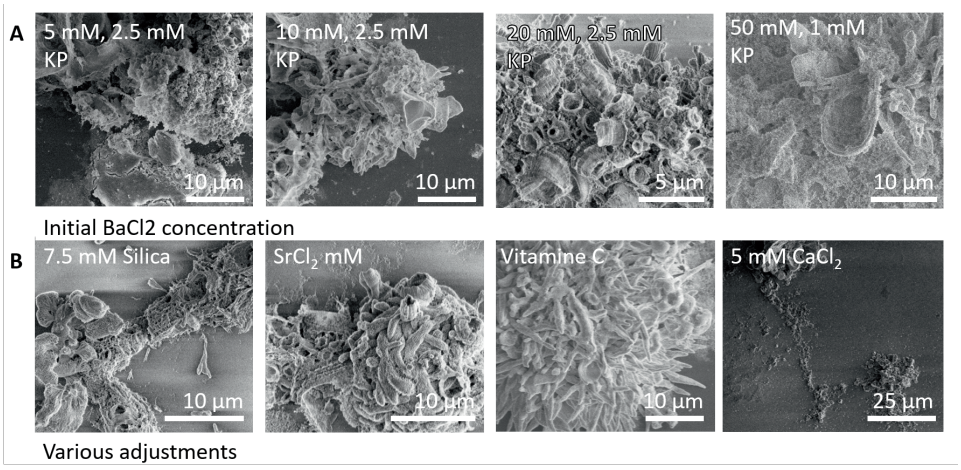

Figure 6.4: Screening of parameters to enhance 532 nm laser-induced precipitation B. Variations in A) variety in MCl_2, additives, silica, and B) initial $BaCl_2$ concentration.

are ruled out due to precipitation occurring in the precursor solution even before irradiation. The addition of Tween20 and Triton-X maintains a stable precursor solution but results in deformed and inhibited co-precipitation in the reference samples when using 365 nm LED irradiation (appendix E, Figure E.7). Subsequently, in the experiment using the 532 nm ps-pulsed laser, these additives fail to exhibit any improvement towards growth of $BaCO_3/SiO_2$ nanocomposites. Similarly, the addition of vitamin C or doubling the surfactant DTAB concentration yields no positive effects. Reducing the silica content maintains the coverage, and even leads to precipitation resembling pure barium carbonate rather than the $BaCO_3/SiO_2$ co-precipitation (Figure 6.4).

Our final attempt to enhance precipitation involves varying the initial $BaCl_2$ concentration. Unfortunately, higher concentrations (35-50 mM) merely exacerbate the coverage of the laser-induced precipitation, likely intensifying silica polymerization. Conversely, concentrations below 20 mM (5 and 10 mM) result in minimal co-precipitation, yielding predominantly unknown structures heavily laden with silica and photoproduct-like precipitates (Figure 6.4).

Despite the presence of unknown structures and covered precipitation, the precipitation induced at the 532 nm focal spot unveils opportunities for three-dimensional controlled self-assembly. To showcase this potential, our objective is to precipitate structures growing from an *x,y*-plane in the *z*-direction (Figure 6.5). We prepare a precursor solution optimized from our previous screening (20 mM $BaCl_2$, 9 mM Na_2SiO_3, 1 mM KP, and 10 mM DTAB, a = 0-0.5), fill a reaction cell equipped with a 1 mm Viton® spacer, and focus the laser on the inner top substrate. Initiating nucleation through irradiation, we allow the precipitation to continue for several minutes. Once a base of precipitation forms, we initiate slow movement of the focal spot downward while ensuring the end of the precipitation remains in focus. This sequential process allows new precipitation to attach to the previous, gradually forming a tower in 3-4 hours. Using SEM, we confirm the tower-like growth to be 175 µm in height and 10 µm in diameter, comprising a blend of unidentified precipitation, $BaCO_3/SiO_2$ co-precipitation, and

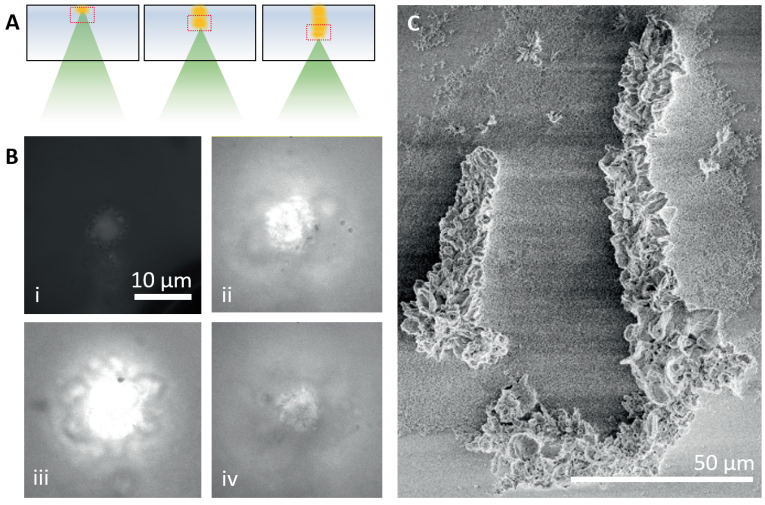

Figure 6.5: Three-dimensional growth with 532 nm laser-induced precipitation. A) schematic of moving laser focal spot with *z*-directional movement. B) Timelapse and C) SEM of the growth with *z*-directional movement of the laser focal spot. D) Schematic of ion conversion to Cadmium carbonate. E) SEM and F) EDS of resulting converted precipitation, cadmium is represented by orange (left) and Chloride is represented by blue (right).

silica and photoproduct-like covering. This achievement marks an initial stride in demonstrating three-dimensional control.

Recent advancements in ion exchange conversion techniques have showcased the potential to transform $BaCO_3/SiO_2$ co-precipitates into a diverse range of compositions. We aim to investigate whether such ion exchange processes are viable with 532 nm laser-induced precipitation (Figure 6.6). Initiating precipitation using a precursor solution (20 mM $BaCl_2$, 9 mM Na_2SiO_3, 1 mM KP, and 10 mM DTA, a = 0-0.5), we guide a moving focal spot, concluding in with static irradiation (overnight, a = 0.5) to create a line in a rectangular pathway, culminating in radial structural growth. Following washing with water and acetone, the induced precipitation on the substrate is directly immersed in a solution of $CdCl_2$ (50 mM) for 20 minutes. Subsequently, after washing the substrate with water and acetone, we analyze the conversion of the precipitation using EDX, which indicates the characteristic signals of Cadmium in the precipitation indicating successful ion exchange (6.6 C). Interestingly, Chloride remains detected within the precipitation. Despite the presence of unknown structures, post-process functionalization demonstrates the feasibility of converting 532 nm laser-induced precipitation via ion exchange.

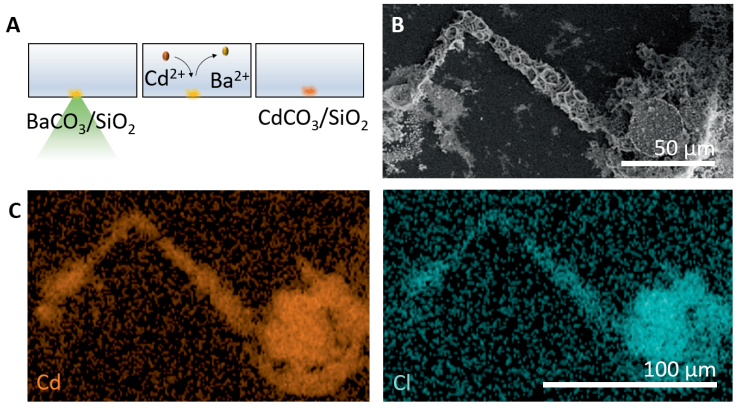

Figure 6.6: Ion-conversion on 532 nm laser-induced precipitation. A) Schematic of ion conversion to Cadmium carbonate. B) SEM and C) EDS of resulting converted precipitation, cadmium is represented by orange (left) and Chloride is represented by blue (right).

6.3 Conclusion

Here, we introduce ps-pulsed 532 nm laser-induced nucleation and growth of $BaCO_3/SiO_2$ structures, marking a significant stride toward achieving 3D controlled self-assembly processes. Our findings indicate that when peak intensity and pulse rate reach sufficient high levels, local precipitation can be induced in a solution containing KP and MCl_2. This precipitation can be directed in the *z*-direction from an *x,y*-plane with high precision, resulting in structures that can even undergo conversion through ion exchange reactions.

We anticipate that further optimization, both in technical and chemical aspects, holds the potential to yield the $BaCO_3/SiO_2$ nanocomposites within the focal resolution. With regard to the laser irradiation, using a setup that enables the reduction of the pulse rate could be a promising avenue. This adjustment might decrease local activity without compromising the intensity necessary for two-photon absorption. Consequently, it could enable switching between nucleation, growth, and different modes. Alternatively, the use of more refined attenuators could adjust the pulse energy in a more sophisticated way than with the neutral density filters used in this work.

With regard to the sample cell, employing a flow cell could help to eliminate excess side products, resulting in grown structures devoid of additional layers of precipitation. Moreover, we recognize that for future research aimed at intricate designs, addressing the stability of these grown structures is crucial. Exploring potential avenues involves utilizing different media, such as hydrogels, which can offer support for delicate designs.[216] However, this approach might hinder the diffusion and supply of building blocks. Furthermore, delving deeper into the unidentified structures within the precipitation warrants investigation. While our current focus remains on familiar materials, this should not preclude the possibility that unconventional structures may offer equally, if not more, intriguing opportunities. Techniques such as FTIR spectroscopy could unveil different molecular structures within their chemical

compositions. Similarly, exploring their internal structure through X-Ray diffraction analysis (XRD) might provide valuable insights over the chemical composition and chemical reactions.

While the current precipitation is not entirely understood and does not purely consist of the familiar $BaCO_3/SiO_2$ co-precipitation found in microarchitectures, these preliminary results underscore the potential of utilizing a pulsed laser to induce photochemical reactions. This ability not only demonstrates the capacity to modulate various forms of precipitation but also underscores the potential for precise 3D control in directing self-assembly systems. Advancements in tuning self-assembly processes—such as those observed in silica gardens,[159,169,224] Liesegang systems,[156,225] and Turing patterns[226]—bring us incrementally closer to creating materials with properties reminiscent of those found in nature, serving structural, protective, and sensory functions. Enabling the 3D printing of those crystalline structures heralds a new level of complexity in material sciences, where functionality emerges from the intricate interplay among external shape, internal structure, and overall composition.

6.4 Experimental

Precursor preparation

Typically, the precursor solution was prepared by dissolving 12.6 mg (6 mM) ketoprofen (KP) (Fluorochem) and 175.0 mg (60 mM) DTAB (VWR) in an 8 mL aqueous solution containing 10.6 mg (11 mM) sodium metasilicate (Na_2SiO_3) (Sigma Aldrich). Sonication was used to enhance the dissolution of KP. In another vial, 49.5 (100 mM) mg barium chloride dihydrate ($BaCl_2{\cdot}2H_2O$) (Sigma Aldrich) is dissolved in 2 mL degassed water. The final precursor solution is made by adding the KP-DTAB-Na_2SiO_3 solution to the $BaCl_2$ solution yielding a final solution with 20 mM $BaCl_2$, 9 mM Na_2SiO_3, 5 mM KP, and 50 mM DTAB. For other KP values, a concentration ratio of 1:10 KP:DTAB was used. All solutions were kept under nitrogen during preparation to avoid uptake of carbonate species from the air.

Set-up

Two microscopes, with different 532 nm laser sources were used for inventory. One system contained the 532 nm Teem Photonics STG-03E-XSX laser with an intensity of 3.5 µJ, a maximum pulserate of 2 KHz and a pulse length of 350 ps. The other system contained a Time Bandwidth Lynx laser that is externally frequency doubled to 532 nm, resulting in 1 nJ pulses at a rate of 10 MHz and with a pulse length below 10 ps. Experiments were performed with the Time Bandwidth Lynx laser coupled into a Nikon Ti microscope with a 60x objective (Nikon S Plan Fluor ELWD, NA 0.7). Neutral density filters were used to tune the intensity of the laser.

Post growth analysis

SEM and EDX imaging was performed using an FEI Verios 460. Raman spectroscopy measurements were carried out by a confocal Raman microscope (Witec, Alpha 300R) with an EMCCD detector (Andor, Newton, DU970P-BVF-355). Excitation was performed with a 532 nm laser while spectra were collected in a spectrometer, equipped with a diffraction grating with a groove density of 600 grooves mm^{-1}. The spectra were each 20 times averaged with an integration time of 1 s.

Chapter 7

Insights & Outlook

With this thesis, entitled "Light-Controlled Self-Assembly – Crystallization in the Spotlight," we explore the potential of using light as a tool to precisely direct the crystallization process of biorelevant crystals. We develop innovative methodologies that can manipulate nucleation and growth with micrometer resolution by leveraging the versatility of light. We investigate the effectiveness of these new methods using $BaCO_3/SiO_2$ nanocomposites and biorelevant minerals (MCO_3, $SrSO_4$, calcium phosphate) as model systems. Through our experiments, we learned the nuances of the process and discovered that, as often, the success lies in the details. The aim of this chapter is to highlight the challenges encountered when exploring the intricacies of the subject matter and to lay the groundwork for future research endeavors. By recognizing the importance of the fine details and presenting preliminary data, our intention is to foster a pathway for deeper comprehension and advancements in this field of study. In pursuit of this goal, we explore fundamental facets of employing light-induced techniques to control crystallization, elucidating their specific relevance to our project. Additionally, we consider potential refinements to these methodologies and venture into diverse pathways for future exploration.

7.1 Controlling local gradients by using photochemistry

In the first method, we focus on creating a local gradient of precursors by inducing a photochemical reaction using either deep ultraviolet (UV) LED light for direct photoexcitation or a picosecond-pulsed 532 nm laser for two-photon absorption. In chapters 2, 3, 4, and 6, we explore how such photochemical reactions integrate into the crystallization process of $BaCO_3/SiO_2$ co-precipitation. We find that controlling nucleation and growth through photochemistry necessitates leveraging fundamental principles and properties of light, photochemistry, crystallization, and reaction kinetics. Consequently, carefully optimizing each parameter in conjunction with others allows us to harness the complex dynamics of both the photochemical reaction and the crystallization process. We anticipate that a comprehensive understanding of these subtleties will facilitate the application of this principle to various other systems. In this section, we discuss the key insights and considerations essential for successfully implementing this method.

Initial conditions

To use photochemistry to regulate crystallization, it is necessary to determine specific conditions in which the crystallization process remains inactive in the absence of light, but becomes responsive when exposed. This can be achieved by identifying a metastable phase in which all precursors are present but remain inactive due to specific environmental conditions.[113,177,227] When such circumstances arise, a photochemical reaction, such as a change in pH, alteration in solvent, or modification in hydrophobicity, can then trigger the crystallization process. Alternatively, the crystallization process may lack a specific precursor building block, which can be released during the photochemical reaction.

This concept is exemplified in the case of ketoprofen and the $BaCO_3/SiO_2$ nanocomposites. In this scenario, the solution of $BaCl_2$ and Na_2SiO_3 is initially inactive because the CO_2 building block is missing. However, by introducing ketoprofen and subjecting it to (deep) UV light irradiation, photodecarboxylation is initiated, resulting in the production of a localized CO_2 gradient.[139,154] This gradient then selectively triggers the co-precipitation of $BaCO_3/SiO_2$ architectures within the irradiated area. Furthermore, the $BaCO_3/SiO_2$ system exhibits a spectrum of sensitivity to the photochemical change of CO_2, thereby enhancing the level of control. This capability not only allows for the activation or deactivation of the reaction, but also offers the possibility of using light manipulation to direct various modes of growth.

Photoreactive compound

To sensitize a system to a photochemical reaction, introducing a photoreactive compound becomes necessary. Yet, dissolving photoreactive compounds in aqueous solutions presents challenges as their UV light absorption often relies on aromatic ring structures, rendering them water-insoluble.[118–120,188,228] Surfactants can be introduced to address this issue, but they might adversely affect crystal growth. Therefore, careful selection of surfactants is crucial to avoid hindering nucleation or growth within a specific system.[229–231] Furthermore, the required quantity of photoreactive compound in the system depends on its efficiency, determined by the induced chemical reaction upon light exposure. This efficiency considers both light absorption and quantum yield, representing the probability of a photochemical reaction per absorbed photon.[232]

The photodecarboxylation of ketoprofen has a quantum yield of 0.75, signifying a 75% occurrence of the reaction upon photon absorption.[233] Coupled with high absorbance, this photocompound showcases remarkable effectiveness, minimizing the need for additional substances that could impede crystallization. However, ketoprofen's protonated form exhibits limited solubility in water, and its released photoproducts are even less soluble.[154] Consequently, upon photoproduct release, the solution becomes turbid, scattering irradiated light and impeding monitoring. To address this, we introduce DTAB into the solution. Fortunately, the addition of DTAB doesn't affect the co-precipitation of $BaCO_3/SiO_2$. However, CTAB, Triton-X, Tween20, and the wetting agent 3-hydroxy(polyethyleneoxy)propyl heptamethyltrisiloxane do affect the $BaCO_3/SiO_2$ co-precipitation and even significantly impede the growth of pure $CaCO_3$.[229]

Light irradiation

The process of initiating crystallization via a photochemical reaction involves exposing the sample to light, wherein light intensity and wavelength play pivotal roles. Adjusting light intensity directly influences the photochemical reaction rate, while wavelength alterations govern light absorption levels. Following Lambert-Beer's law,[234,235] optimal irradiation close to ketoprofen's absorption peak maintains a shallow light penetration depth, ensuring higher spatial resolution. Lower absorption wavelengths penetrate deeper, generally reducing spatial resolution but offering directional growth aligned with light penetration. Doubling the wavelength required for photoexcitation opens the opportunity for two-photon absorption via a 'virtual state' transition.[214,215] This nonlinear effect demands extremely high peak intensities. The advantage is that this phenomenon occurs exclusively within the focal spot, creating a selective three-dimensional photoactive point.

In the case of ketoprofen, we modulate light intensity to control localized CO_2 photogeneration and consequently influence local supersaturation. Leveraging these properties alongside insights from nucleation theories enables us to disentangle nucleation, growth, and direct growth modes based on supersaturation levels. Differences in wavelengths—specifically, penetration depths of 275 nm and 365 nm —establish contour shaping of $BaCO_3/SiO_2$ growth following the irradiated area or for *z*-directional growth, respectively.

Through picosecond pulsed 532 nm irradiation, we experiment to induce ketoprofen photodecarboxylation via two-photon absorption. Observing growth of $BaCO_3/SiO_2$ nanocomposites within the focal spot suggests CO_2 photogeneration. However, the presence of unidentified precipitation indicates other effects, demanding further investigation and optimization. Understanding the impacts of high light intensity, nonlinear processes, and secondary photoreactions is crucial in this context.

Kinetics

The kinetics of photochemistry must align with the intended reactions. In photochemistry, a distinction exists between reaction kinetics in the excited state and those of the photoproducts. Excited states typically have fleeting lifetimes, in the realm of nanoseconds or even shorter.[236–238] When using photochemistry to selectively trigger a reaction involving the photoproduct, the reaction rate with the photoproduct, must exceed the lifetime of the excited state; otherwise, the photoproduct will quickly return to its ground state.

In reactions involving photoproducts, instantaneous or rapid product diffusion can impede the establishment of a gradient with spatial resolution. This challenge surfaced in our experiments with photoacids and bases, where we aimed to create a local pH gradient. Moreover, when employing a light pattern to establish adjacent localized gradients, diffusion kinetics becomes a limiting factor. Rapid diffusion might homogenize gradients between illuminated areas before desired reactions occur, causing a decrease in spatial resolution. Accelerating the kinetics of the intended reactions is crucial to address this issue.

Our experiments reveal that the diffusion of photoreleased CO_2, combined with light intensity, determines spatial resolution. Specifically, smaller illuminated areas require higher intensity than larger areas to reach the nucleation threshold, due to greater diffusion losses and reduced photogenerated CO_2. To create a hexagonal pattern of single $BaCO_3/SiO_2$ nanocomposites with 250 µm spacing, we reduced the nucleation threshold by pre-patterning substrates with $CaCO_3$ crystals. This step shortened the $BaCO_3/SiO_2$ nucleation time before significant CO_2 diffusion occurred.

7.2 Future work with photochemically induced crystallization

By integrating ketoprofen into the co-precipitation process of $BaCO_3/SiO_2$, we have pioneered a novel approach that enables exact spatiotemporal manipulation of crystallization at micrometer-scale resolution. We anticipate that refining both our equipment and crystallization parameters will significantly enhance spatial resolution, empowering advanced sculpting of $BaCO_3/SiO_2$ nanocomposites. Furthermore, harnessing light for precise control over reaction conditions holds implications across diverse scientific domains.

Technical adjustments

Technical adjustments present opportunities to enhance light irradiation on the sample. Altering lenses or employing higher-intensity light sources, such as a UV laser, has the potential to enhance the intensity of the projected light spot. This enhancement could stimulate nucleation and growth in smaller irradiation areas, thereby improving precision. Varied light source configurations offer potential for extended control in higher spatial dimensions. As discussed earlier, the choice of wavelength impacts light absorption and penetration depth. Implementing a small, collimated UV light source with high penetration depth, like 365 nm, could guide precise growth along the light beam, facilitating *z*-directional growth. Expanding on this approach, employing two overlapping UV focal spots or an intersecting light sheet could influence the growth tendency of $BaCO_3/SiO_2$. Initial results of this concept reveal light-guided growth towards the bulk (Figure 7.1).

Alternatively, we investigated two-photon absorption using pulsed laser irradiation. We envision that thorough exploration and refinement of these systems could lead to laser-induced nucleation and three-dimensional growth. This selective activation of the photochemical reaction within the focal spot holds promise for targeted growth in specific directions.

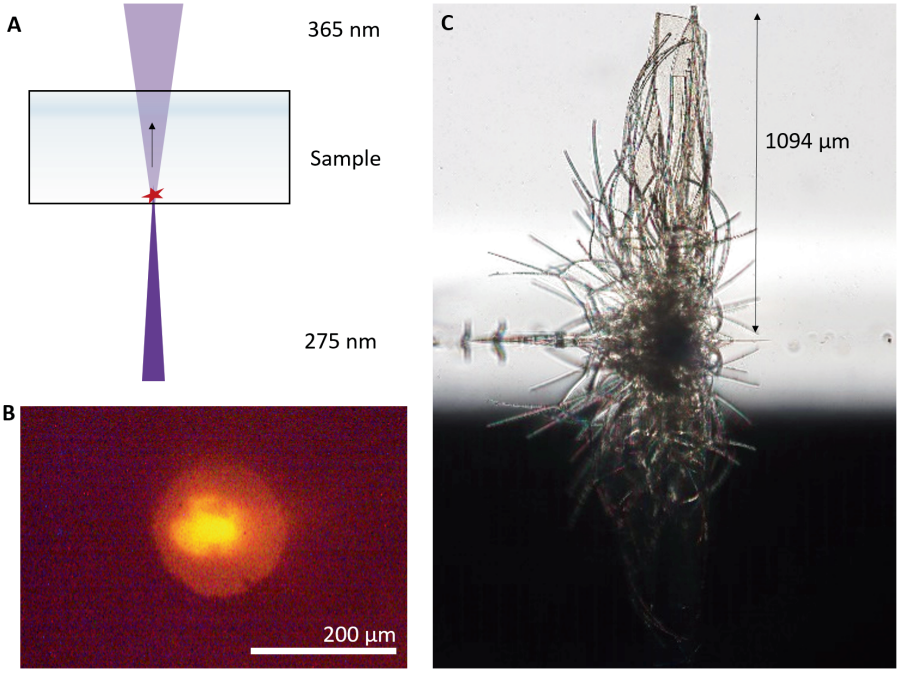

Figure 7.1: Utilizing overlapping irradiation spots achieved by 365 nm and 275 nm LED light irradiation to direct the growth of $BaCO_3/SiO_2$. A) Schematic of two light irradiations on a sample cell containing a precursor solution. B) Light microscope image of the two overlapping irradiation spots, the small bright spot is due to 275 nm, the bigger overlapping spot is due to 365 nm irradiation. C) Camera image of the resulting $BaCO_3/SiO_2$ structure.

Stability of the structures and the precursor solution

Enhancing crystallization conditions shows promise in addressing limitations related to the stability of the growth solution and the structural integrity of these formations. Particularly, larger structures with high aspect ratios heavily rely on single nucleation sites anchored on the substrate. These formations are prone to breakage due to limited support from the water solution, especially during the workup step, where significant tension is exerted on their surfaces. While exploring alternative media such as hydrogels might offer increased support, it may not completely resolve the fragility issue during the workup process. An alternative solution could involve employing ion-exchange conversion to fortify the silica matrix, providing the necessary reinforcement.

Regarding solution stability, challenges related to precursor depletion and aging of the silica solution have emerged. Implementing a flow cell is anticipated to address this, ensuring a consistent supply of fresh precursor solution. This advancement not only holds potential for scaling up growth beyond the millimeter scale but also allows for in-situ alterations. Modifying compositional growth could be achieved by adjusting the precursor solution or conducting an in-situ ion-exchange reaction to manipulate the structure during growth.

In-situ photochemical templating

Beyond its role in initiating crystallization, the photochemical reaction can act as a template that is generated in-situ. In experiments where we do not mitigate the presence of organic photoproducts, we observe a subtle interplay between sterically hindering colloids and $BaCO_3$ crystallization. Notably, this phenomenon manifests itself only under specific conditions where the kinetics of both crystallization and the colloid formation of the photoproducts were closely matched (Figure 7.2). This observation suggests that when the in-situ formation of colloidal photoproducts competes with crystallization kinetics, they intricately adapt to and influence each other's constraints.

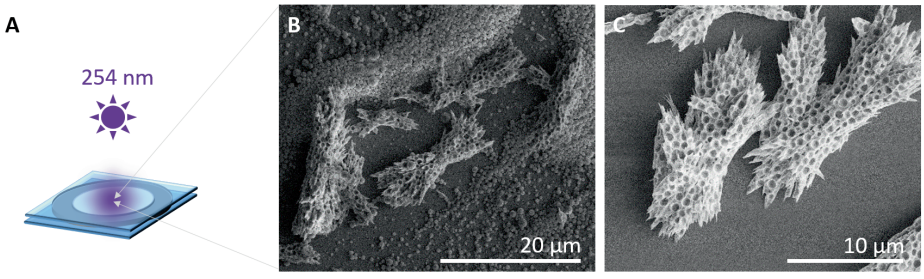

Figure 7.2: $BaCO_3$ crystallization in presence of colloidal photoproduct precipitation. A) Schematic of the 254 nm irradiation on a sample cell filled with 20 mM $BaCl_2$, 1 mM ketoprofen, adjusted to pH 11. B) and C), SEM images of the resulting precipitation found on the bottom substrate of the sample cell.

Other systems

The recent advancements in enhancing the water solubility of photoreactive compounds show promising prospects for expanding the application of photochemistry beyond the biorelevant crystallization processes discussed here.[228,239,240] Simultaneously, there is a growing interest in self-assembly and patterned growth, evident in phenomena such as Liesegang band formation and silica gardens.[152,156,158,225] These intriguing processes offer potential avenues for achieving precise spatiotemporal control. Moreover, the development in photoreactive compounds presents an exciting opportunity to create specific local conditions for ion conversion, enabling the selective positioning of compositions at desired locations and times.

Aligning the properties of various crystal systems with the appropriate photoreactive compounds, while considering the parameters discussed above, holds the potential to establish a novel and comprehensive approach for controlling crystallization systems with high spatiotemporal precision.

7.3 Controlling local gradients by NIR resonance

In chapter 5, we present a method demonstrating crystallization with precise spatiotemporal control induced by a localized heat gradient. Many biorelevant compounds exhibit retrograde solubility, wherein

their solubility decreases with higher temperatures.[196,201,204] By coupling near-infrared (NIR) resonance heating of water with these retrograde-soluble compounds, we induce local crystallization owing to the resultant heat gradient. This approach relies on NIR light's interaction with the solvent,[241] modifying the crystallization environment without requiring additives that might disrupt crystal nucleation and growth. However, achieving selective crystallization within the NIR focal spot still necessitates meticulous alignment of all light system parameters with the crystal system's characteristics. In this section we elaborate on the underlying principles that are required.

NIR resonance with vibrational modes

So far, we used NIR irradiation on water to create a local temperature gradient. The core principle of this method is the resonance between laser irradiation and solvent vibrational modes. Key parameters encompass wavelength and light intensity for irradiation, and heat capacity and absorbance for the solvent.[192] Additionally, consideration should extend to the light absorption of other components in the setup.

The spectral range of the first overtone of water spans the 1300-1600 nm region, offering distinct advantages by avoiding interference with crucial elements such as the glass substrate and the crystal compound itself. However, owing to the relatively lower energy favorability of water's first overtone, its absorption is reduced compared to the fundamental vibration.[241] Consequently, achieving high heating rates demands significantly elevated peak intensities of NIR light.[192,193] We utilize a 1435 nm laser diode with an output power of 180 mW, focused into a 10 µm radius spot. This configuration allows rapid heating to temperatures up to 100°C within milliseconds. Modulating the light intensity provides precise control over the local temperature.

Retrograde soluble compound

The induction of nucleation using generated NIR heat heavily depends on a retrograde soluble compound.[196,201,204] Ideally, this compound should exhibit broad temperature sensitivity and possess a considerable metastable zone, allowing for modulation of supersaturation and solution loading. Maintaining slight undersaturation in the precursor solution initially, prevents spontaneous nucleation. As a result, both the initial precursor concentration and the crystal system's metastable phase dictate the required light intensity for nucleation and influence the control of the nucleation rate. Additionally, modifying the substrate's surface energy or suppressing nucleation through complexation can effectively enhance the selectivity and control of nucleation under light irradiation.[227]

Our experiments reveal significant differences in stabilizing precursor solutions between $BaCO_3$ and $SrCO_3$ compared to $CaCO_3$, suggesting a potentially larger metastable phase for $CaCO_3$ and thus a higher energy barrier slowing down nucleation. Furthermore, the introduction of sodium chloride (NaCl) notably stabilized the solution, facilitating the nucleation of single crystals. Additionally, the NIR absorption of ITO, leading to localized heating, significantly contributed to heightened spatial resolution, thereby enabling localized $CaCO_3$ precipitation. Therefore, adjustments of the experimental conditions make it possible to increase the resolution of spatiotemporal control.

7.4 Future work with NIR resonance

Through NIR laser resonance heating, the nucleation and growth of singular biorelevant crystals with retrograde solubility were facilitated. We foresee that exploring the intricate technical and chemical aspects of NIR resonance heating holds great promise, offering advanced methods for refining shape manipulation and enabling the development of hybrid crystal structures. Additionally, heat accelerates almost all chemical reactions and can also induce thermal reactions, such as decarboxylation. Therefore, harnessing heat broadens possibilities, providing nuanced control across diverse spatiotemporal scenarios.

Hybrid crystals with a flow cell and diffusion control

Employing a flow cell enables the sequential growth of various compositions, forming hybrid crystals with multiple compositions. Yet, a major challenge in this process involves improving heating precision while preserving the stability of the surrounding environment. Heating-induced convection, observed in our studies, may trigger sensitive reactions or disrupt local growth, causing undesired mass transfer and compromising precise spatiotemporal control. Exploring alternative media to limit diffusion could be advantageous; however, we must also ensure the capability to replenish the local heated spot with precursor materials.

Retrograde soluble perovskite

Beyond water-based retrograde soluble compounds, various compounds with intriguing functionalities also exhibit retrograde solubility. Extending the principle of resonance heating to other solvents by applying the appropriate wavelength and necessary peak intensity expands the potential applications across different crystal systems. Perovskites, for instance, known to precipitate around 110°C, serve as an excellent example.[197,242] Determining the resonance wavelength with the vibrational modes of its solvents—primarily gamma-butyrolactone (GBL), dimethylformamide (DMF), or dimethyl sulfoxide (DMSO) —while considering heat capacity, holds promise for achieving controlled spatiotemporal perovskite precipitation.

Laser-induced phase separation

Another application of NIR resonance heating involves manipulating the miscibility of a solution, exemplified by the 2,6-lutidine-water mixture.[208,243] This binary solution showcases a lower solution critical temperature (LSCT), signifying complete miscibility below a specific temperature and phase separation above it.[244] Our initial findings reveal the induction of phase separation in this binary mixture through NIR irradiation at 10 mW (Figure 7.3). NIR irradiation can selectively trigger reactions in one of these phases if it is crucial for a specific reaction. For example, colloidal patchy particles exhibit significant changes in their assembly behavior within distinct temperature ranges. By leveraging NIR resonance heating, we can locally direct this assembly process, enabling the creation of patterned patchy particles as per user-defined designs.

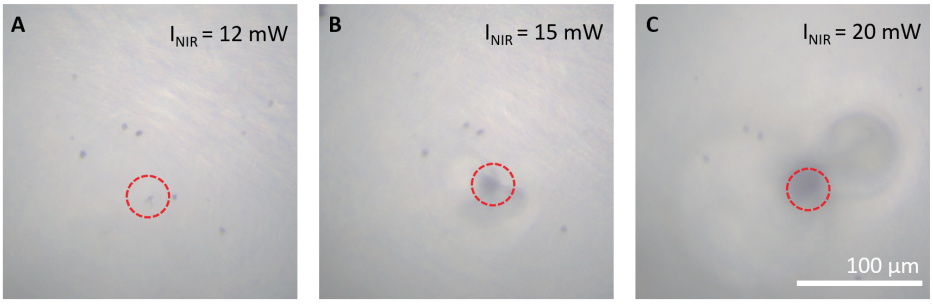

Figure 7.3: Light microscope images of a 2,6lutidine- water (L-W) 1:2 upon 1435 nm NIR irradiation with A) 12, B) 15, and C) 20 mW light intensity. The red solid circle indicates the NIR focal spot.

Plasmonic heating and other systems

The findings of this study underscore the efficacy of utilizing light for generating localized heat, which significantly impacts reactions. Expanding on this insight encourages exploration into alternative systems capable of achieving similar localized heat effects. Plasmonic heating emerges as a promising avenue for investigation, notwithstanding its need for high-powered lasers.[245,246] Nonetheless, its exceptional precision in nanoparticle resolution and wide temperature range offer precise and controlled applications. The high resolution of this method not only enables localized precipitation but also provides valuable insights into heat-driven reactions. Moreover, besides its involvement in crystallization, heat serves as a universal driving force in diverse reactions, including sintering, catalysis, and racemization. The utilization of this localized heat method opens up opportunities for precise control over a wide range of heat-dependent reactions.

In conclusion, our research underscores the potential of light in steering biorelevant crystallization with precise spatiotemporal control. The initiation of a metastable crystal system is achieved through locally induced environmental changes, employing either photochemical reactions or solvent resonance, thereby enabling nucleation. By regulating the intensity of light, we can distinctly manage nucleation separate from growth, allowing control over the shape and size of the crystals. Moreover, dynamic modulations in irradiation facilitate manipulation of crystal growth in more intricate modes. Additionally, the combination of light-directed growth with ion-conversion techniques enables the shaping of materials while independently controlling their form and composition. Understanding the pivotal roles played by parameters within light-crystal systems not only expands potential applications across various systems but also emphasizes the potency of light as a powerful tool for controlling local and dynamic reactions.

Appendix A

Appendix Chapter 2: Light-controlled nucleation and shaping of self-assembling nanocomposites

Movies light-induced nucleation and growth of $BaCO_3/SiO_2$ architectures

1. Light-controlled nucleation and growth

    - Precipitation of one nucleation site.
      In this movie, the nucleation and growth of a single nanocomposite is presented. The movie consists of 87 frames that cover a timespan of 87 minutes real-time growth.

    - Sequential positioned nucleation
      In this movie, the sequential nucleation and growth of two different shaped nanocomposites is presented. The blue frames with the green spot, shown prior to the frames of the growth of the nanocomposites, represents the projection of the light spot on the substrate. The yellow dashed lined circles in the following frames represent the projection of the UV light spot on the substrate during growth. The first part of the movie shows the growth of the helical-shaped composite and consists of 49 frames that cover a timespan of 190 minutes. The second part of the movie shows the growth of the coral-shaped composite and consists of 284 frames that cover a time span of 156 minutes.

2. Static shape contouring according to photomask

    - Static triangular light pattern.
      In this movie, the nucleation and growth of a nanocomposite within a triangular irradiated light area is presented. Prior to the growth, a projection of the triangular irradiated light area is shown. The yellow dashed lined triangle in the following frames represents the projection of the UV light on the substrate during growth. The movie consists of 33 frames that cover a time span of 15 hours real-time growth.

    - Static circular light pattern
      In this movie, the nucleation and growth of a nanocomposite within a circular irradiated

light area is presented. Prior to the growth, a projection of the circular irradiated light area is shown. The yellow dashed lined circle in the following frames represents the projection of the UV light on the substrate during growth. The movie consists of 49 frames that cover a time span of 12 hours real-time growth.

- Static cross light pattern
  In this movie, the nucleation and growth of a nanocomposite within a cross-shaped irradiated light area is presented. Prior to the growth, a projection of the cross-shaped irradiated light area is shown. The yellow dashed lined cross in the following frames represents the projection of the UV light on the substrate during growth. The movie consists of 330 frames that cover a time span of 5.5 hours real-time growth.

3. Dynamic light directed growth

   - Drawing a line with light
     In this movie, the nucleation and growth of a nanocomposite with a moving light beam presented. Prior to the growth, a projection of the irradiated light spot is shown. The yellow dashed lined circle in the following frames represent the projection of the UV light on the substrate during growth. The movie consists of 223 frames that cover a time span of 47 hours real-time growth

Movies are accesible via **dare.uva.nl**

Appendix B

Appendix Chapter 3: Light-controlled morphological development of self-organizing bioinspired nanocomposites

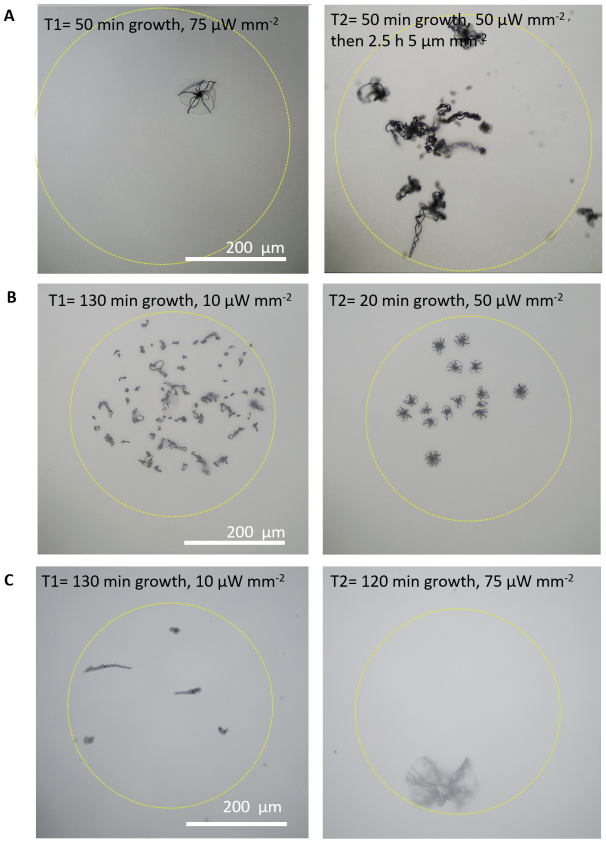

Figure B.1: Light microscope images showing switching between growth regimes due to modulations in light intensity at 275 nm UV in a solution of $BaCO_3/SiO_2$ precursor solutions (20 mM $BaCl_2$, 9 mM Na_2SiO_3) with A) 2 mM KP, 20 mM DTAB, pH 10.89, 250 µm radius (1. coral, 2.helix) ; B) 5 mM KP, 50 mM DTAB, pH 10.89, 200 µm radius (1.helix, 2.coral); and C) 2 mM KP, 20 mM DTAB, pH 10.85, 200 µm radius (1.helix, 2.coral). The yellow circle indicates the illuminated area.

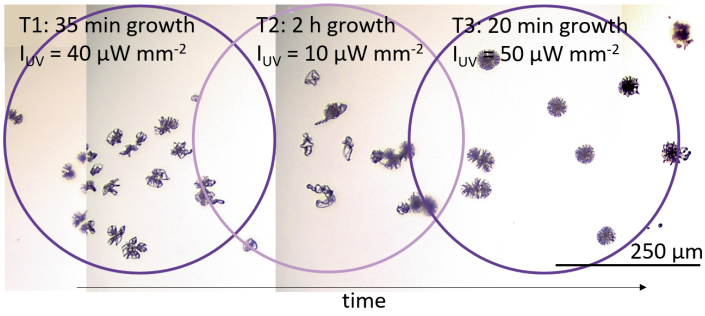

Figure B.2: Light-induced nucleation and growth of $BaCO_3/SiO_2$ structures using low and high light intensity irradiation to induce consecutive switching between coral and helical growth modes. The precursor solution contains 20 mM $BaCl_2$, 11 mM Na_2SiO_3, 5 mM KP, and 50 mM DTAB at pH 11.3. The circles represent the illuminated areas (250 µm radius) for high (dark purple) and low (light purple) light intensity, moving from T1 to T3.

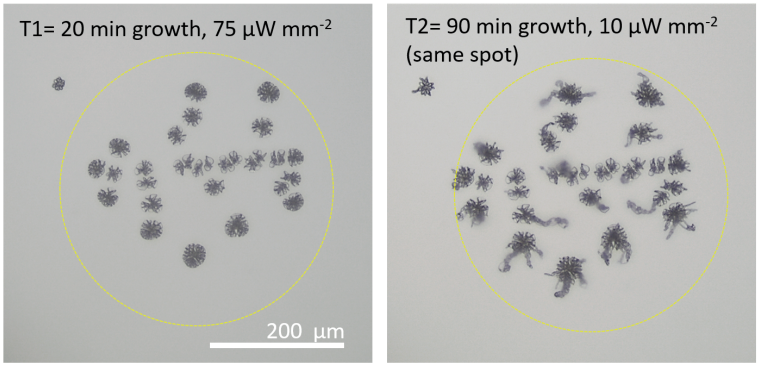

Figure B.3: Switching growth modes with single structures using first (T1) high light intensity irradiation of 275 nm on a precursor solution of 20 mM $BaCl_2$, 9 mM Na_2SiO_3, 5 mM KP, 50 mM DTAB, pH 10.9, 200 µm radius, followed by (T2) low light intensity irradiation. Consistent transitioning from coral to helical growth is observed upon reduction of the light intensity.

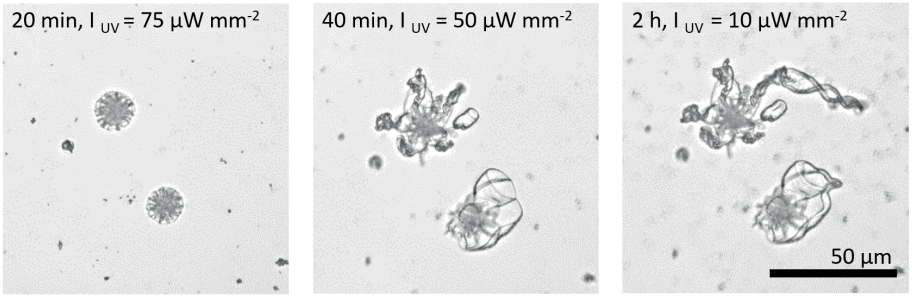

Figure B.4: Switching growth modes with single structures using first high light intensity irradiation of 275 nm on a precursor solution of 20 mM $BaCl_2$, 11.5 mM Na_2SiO_3, 5 mM KP, 50 mM DTAB, pH 10.9, 150 µm radius, followed by low light intensity irradiation.

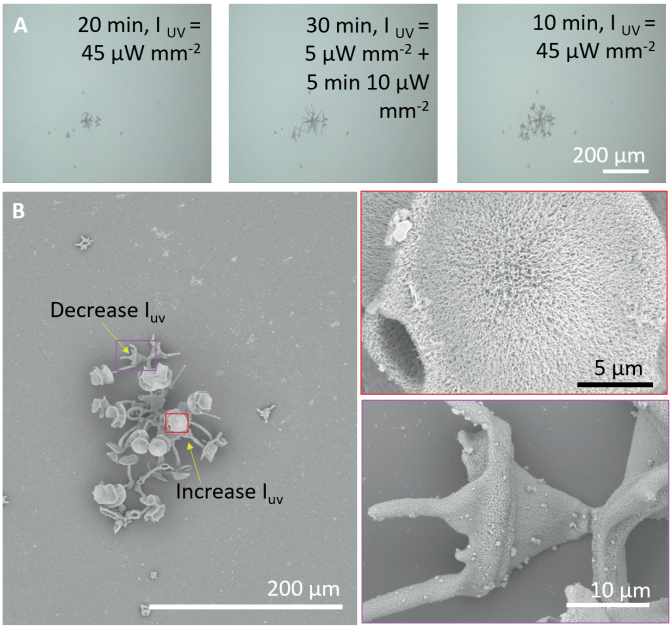

Figure B.5: Sculpting of $BaCO_3/SiO_2$ structures by decreasing and increasing the light intensity, causing narrowing and opening of the growth direction respectively. A) Timelapse and B) resulting SEM images of 275 nm UV irradiation on a precursor solution of 20 mM $BaCl_2$, 9 mM Na_2SiO_3, 5 mM KP, 50 mM DTAB, pH 11.5, 100 µm radius.

Movies light-controlled switching in growth modes of $BaCO_3/SiO_2$ architectures

1. Light-controlled switching from coral to helical growth mode.
   In this movie, the light-controlled transition from coral growth to helical growth of a single $BaCO_3/SiO_2$ nanocomposite is presented. The first 2 seconds show the growth of an architecture with light intensity (I_{UV}) = 75 µm mm^{-2}, yielding growth of a coral shape. Then I_{UV} is reduced to 10 µm mm^{-2}, inducing helical growth. The purple line is an indicative representation of the light intensity. The movie consists of 78 frames that cover a timespan of 140 minutes real-time growth.
2. Light-controlled switching from helical to coral growth mode.
   In this movie, the light-controlled the transition from helical growth to coral growth of a single $BaCO_3/SiO_2$ nanocomposite is presented. The first 4 seconds show the growth of an architecture with I_{UV} = 10 µm mm^{-2}, yielding helical growth. Then I_{UV} is briefly increased to 100 µm mm^{-2}, and subsequently set to 50 µm mm^{-2} inducing the growth of a coral shape. The purple line is an indicative representation of the light intensity. The movie consists of 35 frames that cover a timespan of 120 minutes real-time growth.

Movies are accesible via **dare.uva.nl**

Appendix C

Appendix Chapter 4: Compose and convert controlling shape and chemical composition of self-organizing nanocomposites

Conversion reactions

Conversion of $BaCO_3$ to $CdCO_3$

Anhydrous $CdCl_2$ (458 mg, 50mM) was dissolved in 50 mL demineralized water. A substrate containing fresh $BaCO_3$ nanocomposites was placed in the solution for at least 12 minutes. This yields a $CdCO_3/SiO_2$ nanocomposite.

Conversion of $CdCO_3$ to CdSe

A quartz substrate containing $CdCO_3$ nanocomposites was placed in a single zone tube furnace. An alumina boat, containing 99.9% pure selenium, was added upstream to the single zone tube furnace. The furnace was purged of oxygen and filled with nitrogen until a pressure between 20 and 50 mbar was reached. This pressure was maintained with a 6 sccm flow of N_2 as the furnace was heated to 500°C at a rate of 60°C/min and maintained at this temperature for 1 hour.

Conversion of $CdCO_3$ to CdS

A quartz substrate containing a $CdCO_3$ nanocomposite was placed in a single zone tube furnace. The furnace was purged of oxygen and filled with argon at atmospheric pressure with an argon flow rate of 90 sccm. The tube furnace was heated to 290°C at a rate of 10°C/min and maintained for 1 hour. Once 290°C was reached 10 sccm of H_2S was added to the flow for 50 minutes. Afterwards the oven was purged using argon and allowed to cool. This resulted in a CdS nanocomposite.

Conversion of $CdCO_3$ to CdO

A quartz substrate containing a $CdCO_3$ nanocomposite was placed in a single zone tube furnace. The furnace was purged of oxygen and filled with nitrogen gas till a pressure of 500 mbar was reached. This pressure was maintained with a 50 sccm flow of N_2 as the furnace was heated to 290°C for 4 hours. This resulted in a CdO nanocomposite.

Conversion of $BaCO_3$ to $Co(CO_3)_x(OH)_{2-2x}$) (basic cobalt carbonate)

Cobalt nitrate hexahydrate ($Co(NO_3)_2$) (727 mg, 2.50 mM) was added to a sealable jar together with a quartz substrate containing $BaCO_3$ nanocomposites. The air in the jar was replaced by argon and 50 mL of degassed and demineralized water was added to the jar. After 50 minutes the substrate was removed and carefully washed using demineralized and degassed water followed by a drying step using acetone. This yields a $Co(CO_3)_x(OH)_{2-2x}/SiO_2$ (basic cobalt carbonate) nanocomposite.

Conversion of basic cobalt carbonate to Co_3O_4

A quartz substrate containing basic cobalt carbonate nanocomposites was placed in a single zone tube furnace and left open to air. The furnace was heated to 300°C at a rate of 20°C/min before approaching the final temperature of 380°C at a rate of 5°C/min. The final temperature of 380°C was maintained for 8 hours. This resulted in Co_3O_4 nanocomposites.

Conversion of $BaCO_3$ to $MnCO_3$

Anhydrous $MnCl_2$ (650 mg, 0.1 M) was added to a sealable jar together with a quartz substrate containing $BaCO_3$ nanocomposites. The air in the jar was replaced by argon and 50 mL of degassed and demineralized water was added to the jar. After 60 minutes the substrate was removed and carefully washed using demineralized and degassed water followed by a drying step using acetone. This yields a $MnCO_3$ nanocomposite

Conversion of $MnCO_3$ to MN_2O_3

A quartz substrate containing an MN_2O_3 nanocomposite was placed in a single zone tube furnace and left open to air. The furnace was heated to 540°C at a rate of 10°C/min and maintained for 24 hours. This yields a MN_2O_3 nanocomposite.

Conversion of $MnCO_3$ to MnS

A quartz substrate containing a $MnCO_3$ nanocomposite was placedin a single zone tube furnace. The furnace was purged of oxygen and filled with argon at atmospheric pressure with an argon flow rate of 90 sccm. The tube furnace was heated to 400°C at a rate of 10°C/min and maintained for 1 hour. Once 400°C was reached 10 sccm of H_2S was added to the flow for 50 minutes. Afterwards the oven was purged using argon and allowed to cool. This resulted in a MnS nanocomposite.

Conversion of $BaCO_3$ to Ag_2CO_3

Silver nitrate (1.7 grams, 10 mM) was dissolved in 15 mL of degassed and demineralized water. A quartz substrate containing a fresh $BaCO_3$ nanocomposite was placed in this solution for 1 second before

being removed and washed in water followed by a wash with acetone. The resulting nanocomposite consists of Ag_2CO_3 which will naturally decay to Ag_2O in air over the course of a few days.

Conversion of Ag_2CO_3 to Ag_2O

A quartz substrate containing a Ag_2CO_3 nanocomposite was placed in a single zone tube furnace. The furnace was purged of oxygen and filled with nitrogen at atmospheric pressure with a flow of 30 sccm. The furnace was heated to 120°C at 5°C/min and maintained for 24 hours. This yields a Ag_2O nanocomposite.

Conversion of $SrCO_3$ to $PbCO_3$

Lead Nitrate ($Pb(NO_3)_2$, 15 g, 906 mM) was dissolved in 50 mL degassed and demineralized water under a nitrogen atmosphere. A quartz substrate containing a fresh $SrCO_3$ nanocomposites was placed in this solution for 45 seconds. Afterwards, the substrate containing the white nanocomposite was removed and washed in three demineralized water baths followed by an acetone bath. This yields a $PbCO_3$ nanocomposite

Conversion of $PbCO_3$ to $MAPbBr_3$ perovskite

A quartz substrate containing a $PbCO_3$ nanocomposite was placed in a saturated solution of MABr in IPA for 5 seconds before removing the substrate and washing with methanol. This yields a $MAPbBr_3$ perovskite nanocomposite.

Table conversion reactions

Related figure	Cationic conversion	Anionic conversion	Additional comments
4.3 - An array of corals	$BaCO_3$ to $CdCO_3$	$CdCO_3$ to CdO.	
4.4 – triangular shaped	$BaCO_3$ to $Co(CO_3)_x(OH)_{2-2x}/SiO_2$ (basic cobalt carbonate)	basic cobalt carbonate to CO_3O_4.	Slower initial heating rates cause more breakage of the nanocomposite.
4.5- a line with two turns	$BaCO_3$ to $MnCO_3$	$MnCO_3$ to MnS	The cationic conversion time was extended to 120 minutes to compensate for the denser structure.
4.6, 3 in a row, first structure	$BaCO_3$ to Ag_2CO_3	Ag_2CO_3 to Ag_2O	
4.6, 3 in a row, second structure	$BaCO_3$ to $MnCO_3$	$MnCO_3$ to Mn_2O_3	This reaction goes over 300°C. At this temperature Ag_2O is known to be converted from Ag_2O to Ag

4.6, 3 in a row, third structure	$BaCO_3$ to $Co(CO_3)_x(OH)_{2-2x}$ /SiO_2 (basic cobalt carbonate).	basic cobalt carbonate to CO_3O_4
4.7, 3 in a row, first structure	$BaCO_3$ to $CdCO_3$	$CdCO_3$ to CdSe
4.7, 3 in a row, second structure	$BaCO_3$ to $CdCO_3$	$CdCO_3$ to CdS
4.7, 3 in a row, third structure	$BaCO_3$ to $CdCO_3$	$CdCO_3$ to CdO
4.8, triangle w circle. Triangle	$BaCO_3$ to $CdCO_3$	$CdCO_3$ to CdSe
4.8, triangle w circle. Circle	$BaCO_3$ to Ag_2CO_3	Ag_2CO_3 to Ag_2O
4.10, Perovskite Pb core	$SrCO_3$ to $PbCO_3$	N/A
4.10, Perovskite overgrowth	N/A	$PbCO_3$ to MAPbBr3 perovskite

Schematic overview of light-microscope set-ups

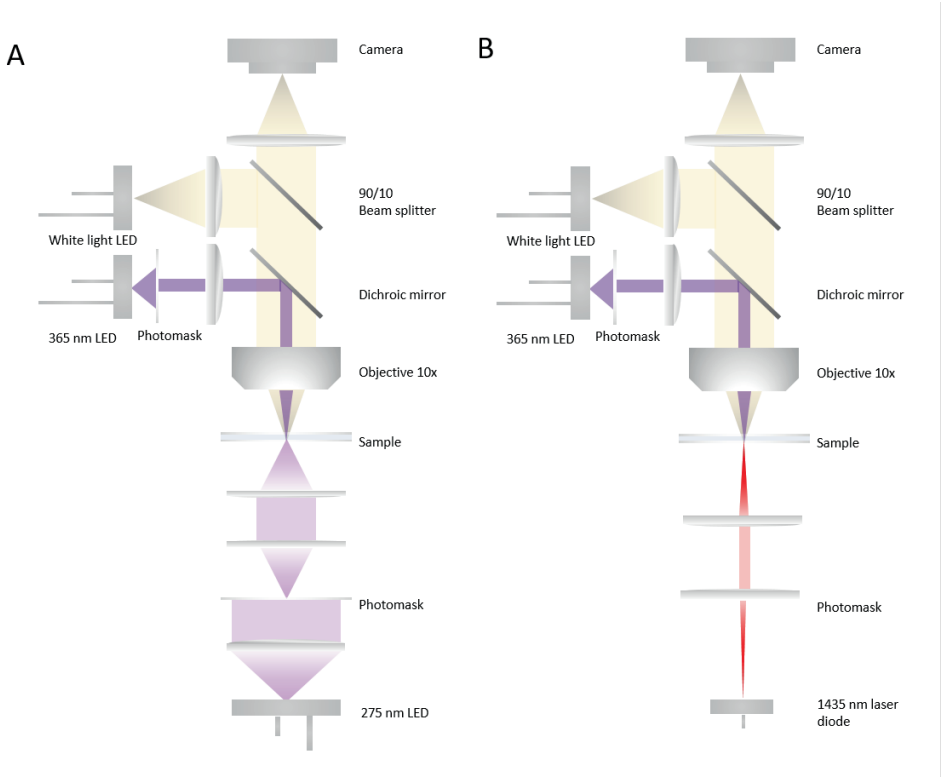

Figure C.1: Schematic overview of a double UV irradiation using (A) a 365 nm and 275 nm LED and (B) a 365 nm LED and 1435 nm laser diode.

Table light schedules for nucleation and growth of MCO_3/SiO_2

Fig.	Precursorsor solution (mM)	Light irradiation for nucleation (A= area, I= light intensity, t= time)	Light irradiation for growth (A= area, I= light intensity, t= time)
4.3 An array of corals	20 mM $BaCl_2C$, 9 mM Na_2SiO_3, 5 mM Ketoprofen, 50 mM DTAB	275 nm, A= radius 50 µm, I = 100 µW/mm^2, t = 15- 35 s per nucleation-site, in a constant irradiation of overlapping 365 nm, A= radius 250 µm, I = 4.5 µW/mm^2	365 nm, A= radius 250 µm, I = 4.5 µW/mm^2, t = 1 h 20 min
4.4 – triangular shaped	20 mM $BaCl_2C$, 9 mM Na_2SiO_3, 5 mM KP, 50 mM DTAB	275 nm, A= triangular shaped projection with arms of 350 µm , I = 75 µW/mm^2, t = 60 s per nucleation site	275 nm, A= triangular shaped projection with arms of 350 µm, I = 75 µW/mm^2, t = 5.5 h per nucleation site
4.5 a line with two turns	20 mM $BaCl_2C$, 9 mM Na_2SiO_3, 5 mM KP, and 50 mM DTAB	365 nm, A= radius 125 µm, I = 535 µW/mm^2, t = 3 s	1. 365 nm, A= radius 125 µm, I = 32 µW/mm^2, t = 3 min 2. 365 nm, A= radius 25 µm, I = 400 µW/mm^2, t = 5 min 3. 365 nm, A= radius 25 µm, I = 435 µW/mm^2, t = 3 h 20 min, additional 1435 nm overlapping with UV, ramping I= 10-25 mW within the first 10 min, then after 50 min to 30 mW.
4.6, 3 in a row, first structure	20 mM $BaCl_2C$, 9 mM Na_2SiO_3, 5 mM KP, 50 mM DTAB	275 nm, A= radius 50 µm, I = 100 µW/mm^2, t = 6 s per nucleation-site, in a constant irradiation of overlapping 365 nm, A= radius 250 µm, I = 10 µW/mm^2	365 nm, A= radius 250 µm, I = 10 µW/mm^2, t= 1 h 45 mi
4.6, 3 in a row, second structure	20 mM $BaCl_2C$, 9 mM Na_2SiO_3, 5 mM KP, 50 mM DTAB	275 nm, A= radius 100 µm, I = 100 µW/mm^2, t= 4 s	275 nm, A= radius 100 µm, I = 10 µW/mm^2, t= 2 h
4.6, 3 in a row, third structure	20 mM $BaCl_2C$, 9 mM Na_2SiO_3, 5 mM KP, 50 mM DTAB	275 nm, A= radius 100 µm, I = 100 µW/mm^2, t= 12 s	275 nm, A= radius 100 µm, I = 25 µW/mm^2, t= 2 h

4.7, 3 in a row, first structure	20 mM $BaCl_2C$, 9 mM Na_2SiO_3, 3 mM KP, 30 mM DTAB	365 nm, A= radius 75 µm, I = 400 µW/mm^2, t = 7 s	365 nm, A= radius 75 µm, I = 45 µW/mm^2, t= 1 h 20 min
4.7, 3 in a row, second structure	20 mM $BaCl_2C$, 9 mM Na_2SiO_3, 5 mM KP, 50 mM DTAB	365 nm, A= radius 75 µm, I = 400 µW/mm^2, t = 2 s	275 nm, A= radius 75 µm, I = 25 µW/mm^2, t= 1 h 40 min
4.7, 3 in a row, third structure	20 mM $BaCl_2C$, 9 mM Na_2SiO_3, 5 mM KP, 50 mM DTAB	365 nm, A= radius 75 µm, I = 535 µW/mm^2, t = 10 s	275 nm, A= radius 75 µm, I = 45 µW/mm^2, t= 1 h
4.8, triangle w circle. Triangle	20 mM $BaCl_2C$, 9 mM Na_2SiO_3, 5 mM KP, 50 mM DTAB	275 nm, A= triangular shaped projection with arms of 250 µm , I = 100 µW/m µW/mm^2, t = 3 s	275 nm, A= triangular shaped projection with arms of 250 µm , I = 50 µW/mm^2, t = 6 h

To grow a line with an arbitrarily shaped line we prepare a precursor solution of 20 mM $BaCl_2$, 9 mM Na_2SiO_3, 5 mM KP, and 50 mM DTAB. We fill the reaction cell and upon irradiation of an area with a radius of 125 µm with high intensity 365 nm light (535 µW/mm^2) for 3 seconds we induce nucleation. We directly lower the light intensity to 32 µW/mm^2 to enable growth for 3 minutes. Then we reduce the illuminated area to a spot size with a radius of 25 µm. We place the growing structure in the middle of the spot and increase the light intensity to 400 µW/mm^2 to continue growth. After 5 minutes we additionally turn on the 1435 NIR laser irradiation, which focal spot is located in the middle of the UV spot. We ramp the intensity of the NIR laser from 10 mW output power to 25 mW in 10 minutes, while we simultaneously increase the UV light irradiation to 435 µW/mm^2. We start moving the sample away from the light spots with a pace that matches the growth rate to keep the growth front in a constant location in the irradiated area and selectively enable growth in one direction. After 50 minutes of growth we increase the NIR output power to 30 mW. We change direction of movement after 75 minutes of growth in *x*- direction, to movement in *y*-direction. After one hour in growth in *y*-direction, we change the movement again in *x*-direction. We enable growth for another 50 minutes to complete a total growth time of 3 hours and 20 minutes. We observe a faster growth at the end, which can indicate a gradual increase of the bulk solution.

Crystal lattice shrinkage

Due to the different size of the crystal lattice between $BaCO_3$ and Co_3O_4, the converted structures shrinks in volume (Figure C.2).

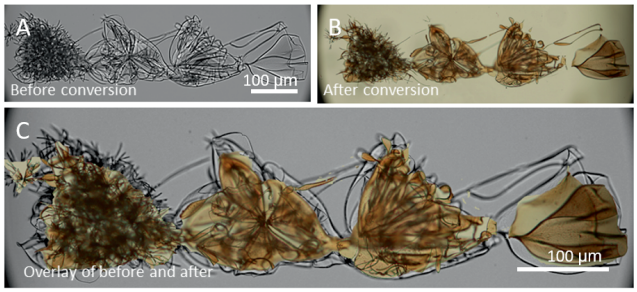

Figure C.2: Comparision of the volume change due to conversion. A) triangular shaped $BaCO_3/SiO_2$ structures before conversion (top left). B). Co_3O_4 triangular shaped after conversion. C) overlay of B (colored) on top of A (greyscale).

Preferable nucleation sites

We investigate the nucleation and growth of new $BaCO_3/SiO_2$ structure in presence of other grown and converted structures. We first enable nucleation and growth of $BaCO_3/SiO_2$ structures upon irradiation of 365 nm LED light for 90 minutes in precursor solution of 20 mM $BaCl_2$, 9 mM Na_2SiO_3, 1 mM KP, and 10 mM DTAB. We convert the grown structures to $CdCO_3$ subsequently to CdO by using the procedure in section 1. Afterwards we heat the tube furnace to 500°C and 500 mbar which is maintained for 72 hours. This experiment is repeated on a separate substrate except a pressure of 1 mbar is used in the heating step resulting in the sublimation of CdO and subsequent emptying of nanocrystals from the nanocomposite.

Then we prepare a new precursor solution (20 mM $BaCl_2$, 9 mM Na_2SiO_3, 2.5 mM KP, and 25 mM DTAB). We position a small UV spot with a radius of 50 µm at the substrate with the converted structures. When the UV spot overlaps with already grown and converted structures, we observe no new nucleation, but selectively overgrowth on the illuminated structure and the neighbouring structures. When the UV spot is positioned at locations on the substrate where no structures were grown, we observe new nucleation site within minutes (Figure C.3). This indicates that despite of the different crystal structure, growth on the converted structures is preferred over the substrate.

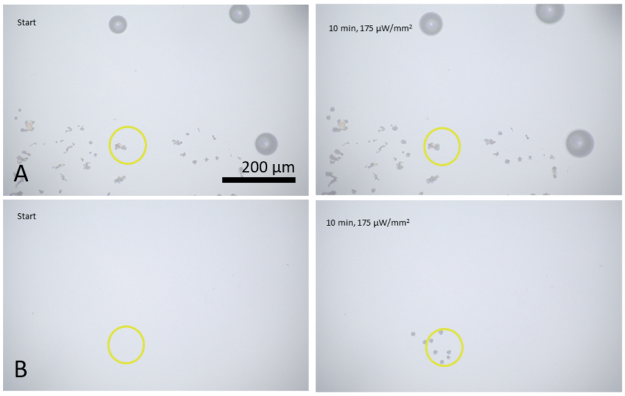

Figure C.3: Nucleation and growth of $BaCO_3/SiO_2$ structures in presence and absence of converted structures. A) left, start of irradiation with an overlap and neighboring converted structures. A) right, after 10 minutes irradiation with 175 µW/mm^2 growth is only observed at the converted structures. B) left, start of irradiation with a no neighboring converted structures (same substrate and reaction cell). B) right, after 10 minutes new nucleation sites in the UV irradiated area is observed. The yellow circle represents the position of the UV irradiated area.

Appendix D

Appendix Chapter 5: Light-driven nucleation, growth, and patterning of biorelevant crystals using resonant near-infrared laser heating

Interfacial temperature measurements at the center of the heating NIR beam.

The choice of wavelength (400 nm) allows us to excite HPTS at its absorption maximum:

$$\epsilon_{att} \approx 20000 \frac{l}{mol \cdot cm^{-1}} \tag{D.1}$$

For the UV light, this yields a penetration depth ($\frac{1}{e}$ transmission, ca. 37%) of

$$d^{UV} = \frac{\log e}{\epsilon_{att} \cdot c} \approx 43\,\mu m \tag{D.2}$$

which is much shorter compared to the ≈ 370 µm penetration depth of the NIR beam.[247,248] Because $d^{UV} \ll d^{NIR}$, we essentially sample the interfacial temperature of the heated solution. We find that the temperature a) changes within seconds, and b) increases approximately linearly with NIR intensity, and c) reaches ca. 90 ± 5 °C upon a NIR heating of 180 mW (Supplementary Figure 1c-e). For reaction cells built with ITO coated substrates, we find a higher maximum temperature change upon NIR light intensity, reaching ca. 110 ± 10 °C upon a NIR light intensity of 180 mW (Supplementary Figure 1f). Note that the irradiated part of the ITO coated substrate will be even higher in temperature than the measured solution due to additional heating (Supplementary Figure 3). Using the thermocouple, the bulk solution measured at ca. 1 mm from the heating spot rises only from ca. 26 °C to 30 °C during 17 h of NIR heating.

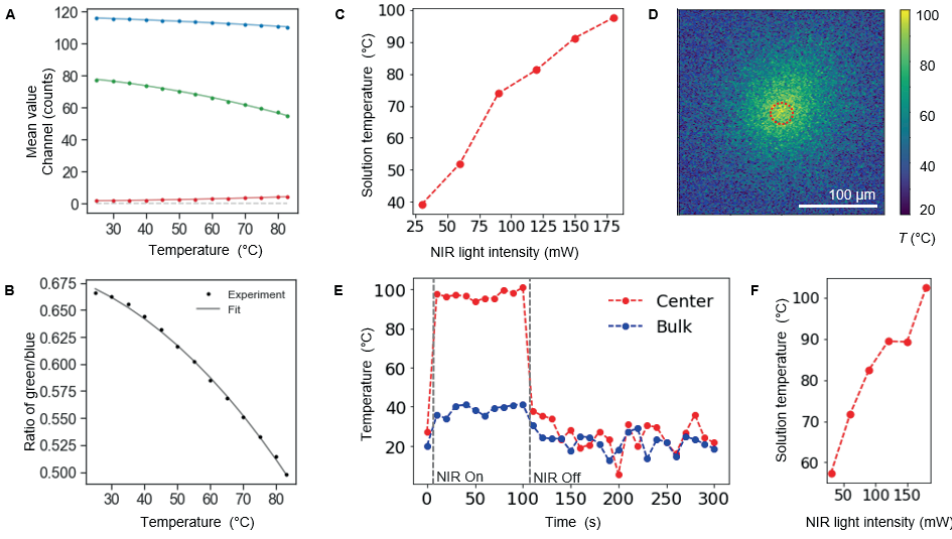

Figure D.1: To monitor spatially resolved interfacial temperature changes upon NIR laser irradiation, we developed a fluorescence-based experimental method that utilizes the photoacid 8-hydroxypyrene-1,3,6-trisulfonic trisodium salt (HPTS). HPTS has two emission bands, centered at 440 and 510 nm. These bands almost perfectly overlap with the green (G) and blue (B) channels of the CMOS sensor in our transmission microscope, which allows monitoring their ratios without a spectrometer. To excite HPTS, we illuminate the sample cell from the same side as the NIR laser diode, using a commercial, low-intensity 400 nm UV LED. To evaluate local temperature changes induced by the NIR laser heating, we construct a calibration curve based on G:B ratios. To this aim, we heat the HPTS solution in the reaction cell with a bath and circulation thermostat (Huber CC-K6) to 83 °C under illumination of a 400 nm LED and record the RGB channels. A) Mean values of blue, green, and red channel of the color CMOS camera upon externally controlled heating. Blue, green, and red dots and lines represent experimental and fitted data respectively of the different blue, green, and red channels. B) Calibration curve of the RGB ratio values with the absolute temperature. Data points are fitted with a second order polynomial. C) Solution temperature upon NIR light intensity in the beam area. D) Spatial temperature distribution upon 180 mW NIR irradiation. The dashed red circle represents the NIR focal spot. E) Time-dependent solution temperature upon with 180 mW NIR irradiation, at the beam center (red dots) and in the bulk of the solution, ca. 150 µm away from the NIR focal point (blue dots). The NIR was manually turned on and off after 10 and 110 seconds, respectively, indicated by the grey dashed lines. F) Solution temperature upon NIR irradiation on an ITO coated substrate.

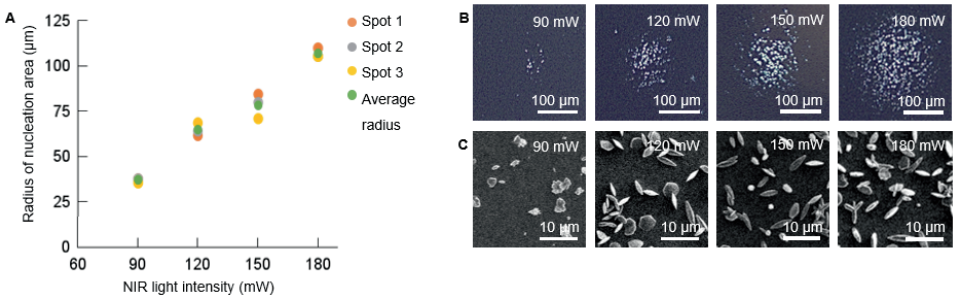

Figure D.2: To investigate how the NIR light intensity determines the nucleation rate of $CaCO_3$, four reaction cells with a freshly prepared precursor solution of fixed concentrations (1.5 mM $CaCl_2$, 1 mM Na_2CO_3, 300 mM NaCl, pH 10.7) are prepared and a NIR light beam is focused with different light intensities on the substrates of the reaction cells. Per reaction cell, one NIR light intensity (90, 120, 150, or 180 mW) with which we subsequentially irradiate three light spots is used, each for 45 s. After the NIR light irradiation, the cell with is directly washed with water and ethanol and let it dry in air. To analyze and compare the induced nucleation upon the irradiation with different light intensity, we use insitu monitoring, light microscope imaging, and SEM imaging. For the freshly prepared solutions, we find the nucleation of mainly vaterite and aragonite in a small radius (35-110 µm) of the irradiated area with all light intensities. A) Plot of the area in which nucleation is observed upon NIR light intensity. Within the regime of 90-180 mW, the area where nucleation is observed increases almost linearly for increasing light intensities. B) Light microscopy images of the NIR light induced nucleation. The results indicate a light intensity offset with respect to nucleation, since with 90 mW NIR light intensity almost no nucleation is observed. C) SEM images of NIR light induced nucleation at the center of the NIR irradiated area. For light intensities of 120 mW and higher, the nucleation density at the center of the light spot does not significantly differ within this time span of 45 s.

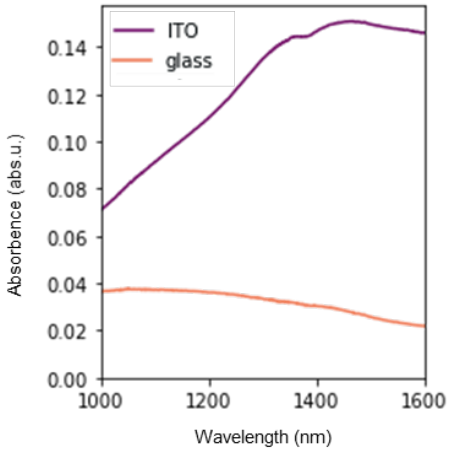

Figure D.3: NIR absorption of glass and ITO coated glass. Steady-state external absorbance measurements of glass (orange line) and ITO-coated glass (purple line) in the range of 1000-1600 nm using a LAMBDA 750 UV/vis/NIR spectrophotometer (Perkin Elmer), equipped with a deuterium and tungsten excitation source, an InGaAs detector, and an integrating sphere.

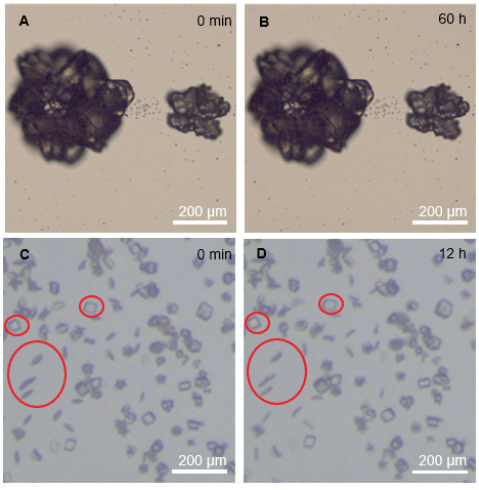

Figure D.4: Dissolution test. Monitor of NIR light induced $CaCO_3$ when placed outside the NIR light spot. To test if dissolution of NIR light induced crystals occurs when placed outside the NIR light spot, we closely monitor a reaction cell filled with a 2 days old $CaCO_3$ precursor solution (0.5 mM $CaCl_2$, 1 mM Na_2CO_3, 400 mM NaCl, pH 10.7) with and without NIR irradiation. First, we induce the nucleation and growth of $CaCO_3$ upon high intensity (180 mW). We continue NIR light irradiation until no further growth is observed (48 h). We turn off the NIR laser light, but we continue to monitor the grown crystals (60 h). A) Light microscopy image of NIR light induced $CaCO_3$ crystals at t = 0 min, directly, placed outside the NIR light spot and B) t = +60 h. No dissolution is observed dissolution for neither the large grown crystals nor small nucleated calcite-like crystals, indicating that the NIR light grown calcite crystals remain stable and that the growth solution is only slightly undersaturated at room temperature after the NIR irradiation. To evaluate the thermodynamic stability between polymorphs after irradiation, we induce the nucleation of a mixture of calcite and vaterite with a freshly prepared precursor solution which contains rather high precursor concentrations (5 mM $CaCl_2$, 1 mM Na_2CO_3, 100 mM NaCl pH 10.7). We irradiate for several hours with high light intensity to induce nucleation and growth of mixed $CaCO_3$ (180 mW for 3 h). C) Light microscopy image of NIR light induced vaterite and calcite crystals at t = 0 min, directly placed outside the NIR light spot, and D) t = +12 h. Red circles point out the dissolution of vaterite and growth of calcite. We observe slow dissolution of small vaterite crystals and further growth of calcite crystals which indicates that the light induced small vaterite is thermodynamic less stable than calcite.

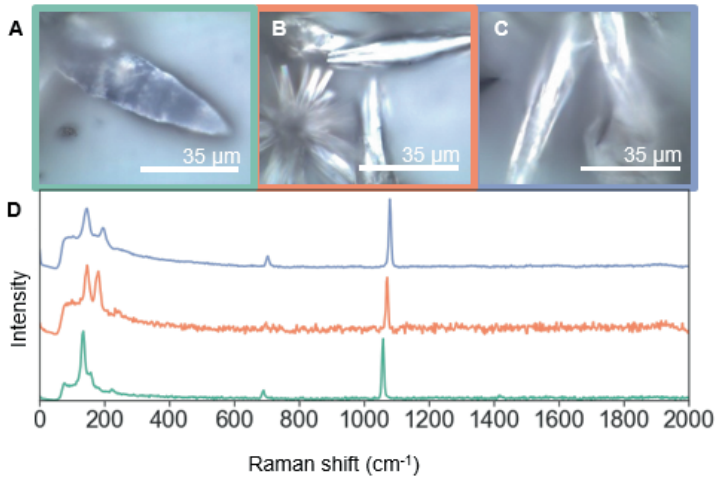

Figure D.5: Raman spectra of NIR light induced $CaCO_3$ polymorphs. A) Light microscope imaging of the probed area for Raman spectroscopy of $CaCO_3$ grown in presence of $MgCl_2$, B) $CaCO_3$ grown in presence of NaCl without equilibration time, and C) $CaCO_3$ grown in presence of NaCl after 3 h of equilibration time. D) Raman spectra of $CaCO_3$ indicated by colored boxes and indices corresponding with (a-c), top (yellow) aragonite, middle (green) vaterite, and bottom (pink) calcite.

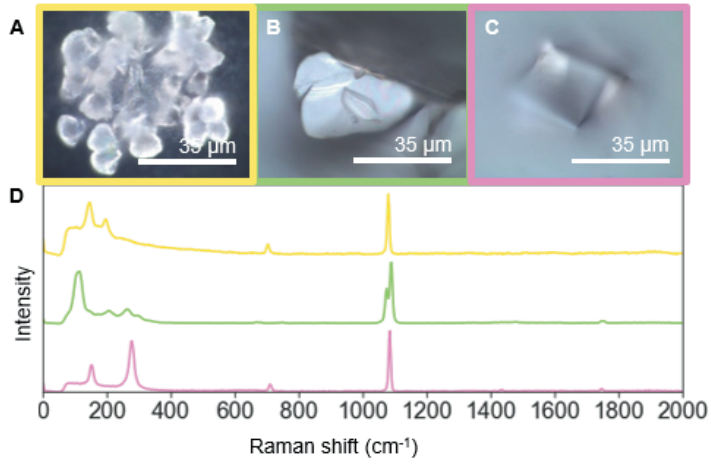

Figure D.6: Raman spectra of NIR light induced MCO_3 crystals. A) Light microscope imaging of the probed area for Raman spectroscopy of $BaCO_3$, B) $SrCO_3$, and C) $CaCO_3$. D) Raman spectra of the MCO_3 crystals indicated by colored boxes and indices corresponding with (a-c), top (blue) $CaCO_3$, middle (orange) $SrCO_3$, and bottom (green) $BaCO_3$.

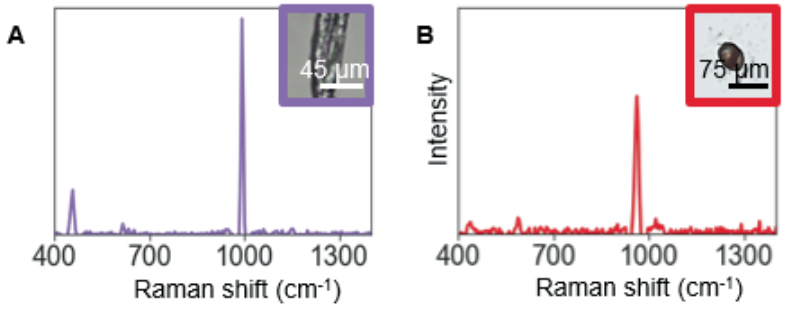

Figure D.7: Raman spectra of NIR light induced $SrSO_4$ and calcium phosphate crystals. A) $SrSO_4$, and B) calcium phosphate crystals with the light microscope image of the probed area in the inset.

Movie NIR light induced nucleation and growth of $CaCO_3$ crystals

In this movie, the nucleation and growth of $CaCO_3$ crystals positioned in a line (described in the main text) are presented. The red dashed circle represents the location of NIR light spot. The total movie consists of 453 frames that cover a time span of 61 h real-time growth. Due to the long timespan the video contains some time jumps. The real-time of crystallization per crystal as numbered in the movie is (times of nucleation are an estimation):

1. 16 h (growth 120 mW, nucleation within first minute with 180 mW)
2. 6 h (growth 120 mW, nucleation within first hour as well with 120 mW)
3. 14 h (growth 130 mW, nucleation within first hour with 140 mW)
4. 9 h (130 mW, nucleation within first 2 h as well with 130 mW)
5. 17 h (120 mW, nucleation within first 3 h as well with 120 mW)

Movies are accesible via `dare.uva.nl`

Appendix E

Appendix Chapter 6: Towards light-controlled nucleation and growth of self-assembling nanocomposites with three-dimensional spatial resolution

	water	Silica	KP	DTAB	BaCl2	CaCl2	SrCl2
Water	Nothing	Nothing	pH 12.5, small bubbles, line of precipitation, with leica not findable again	Nothing	Not done	Not done	Not done
Silica			Bubble formation, coffee ring precipitation, not findable in leica	Nothing	Nothing happens	Not done	Not done
KP				Local Bubble formation, some dark line precipation, not findable in leica	Not done	High pH needed, line of precipation + spontaneous calcite precipitation	Not done
Silica + KP					+ DTAB Bubbleformatio n and structure formation	Not done	+ DTAB Bubbleformation and structure formation
KP+ DTAB					Not done	Local bubbles, line formation, lightening stuff in there. SEM: photoproduct, but it was low pH.	Not done

Figure E.1: Observations of the irradiation of a 532 nm ps-pulsed laser (Time Bandwidth Lynx laser) with an intensity of 10 mW and a pulserate of 10 MHz equipped with 60X objective (Nikon S Plan Fluor ELWD, NA 0.7) on precursor solution with various components.

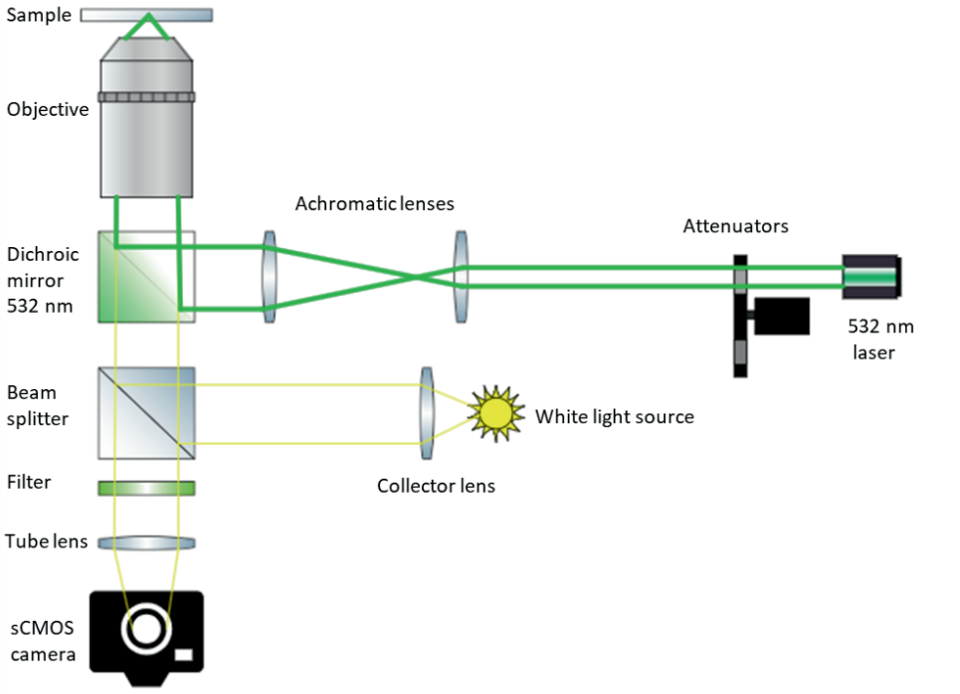

Figure E.2: Schematic overview of the 532 nm Time Bandwidth Lynx laser with an intensity of 1 nJ and a pulse rate of 10 MHz equipped with 60X Nikon S Plan Fluor ELWD, NA 0.7, objective.

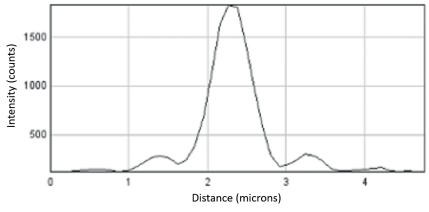

Figure E.3: Line intensity-plot of the focal spot of the ps-pulsed 532 nm laser

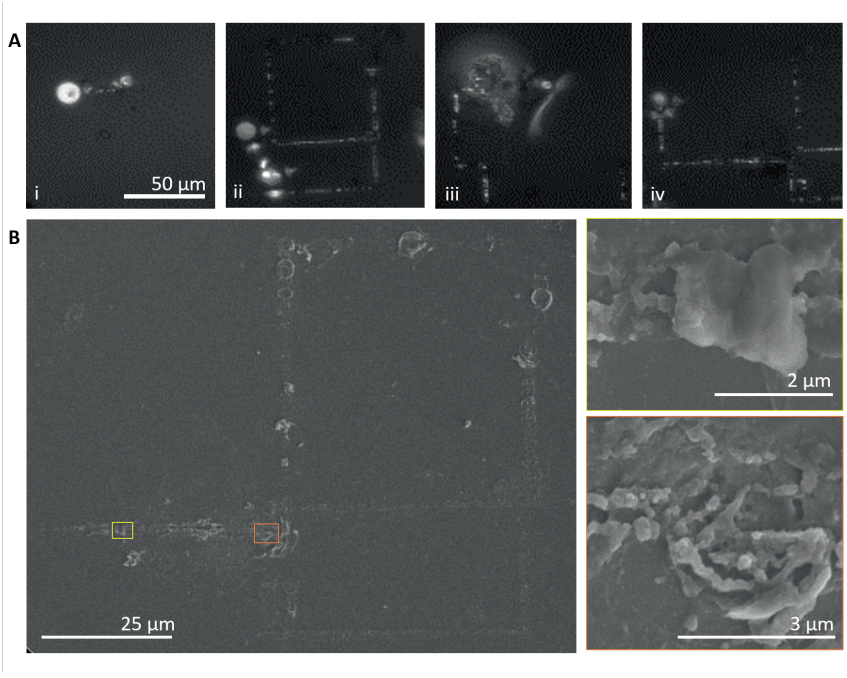

Figure E.4: Resulting precipitation due to 532 nm ps-pulsed laser irradiaton on a solution containing 5 mM KP with 5 mM $CaCl_2$, pH 5.

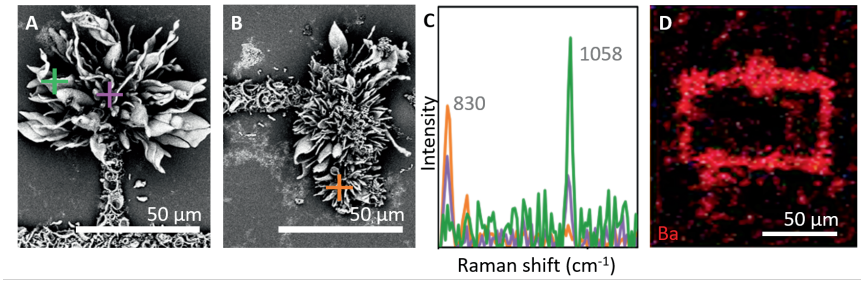

Figure E.5: Raman and EDX spectra of 532nm ps-pulsed laser-induced precipitation. A) and B) SEM images of 532 nm ps-pulsed laser-induced precipitation. C) Raman spectroscopy pectra of color matching indicated points in (A) and (B), showing either a peak at 1058 cm^{-1}, or a peak at 830 cm^{-1}, or both peaks. D) EDS image demonstrating Barium in the 532 nm laser-induced precipitation.

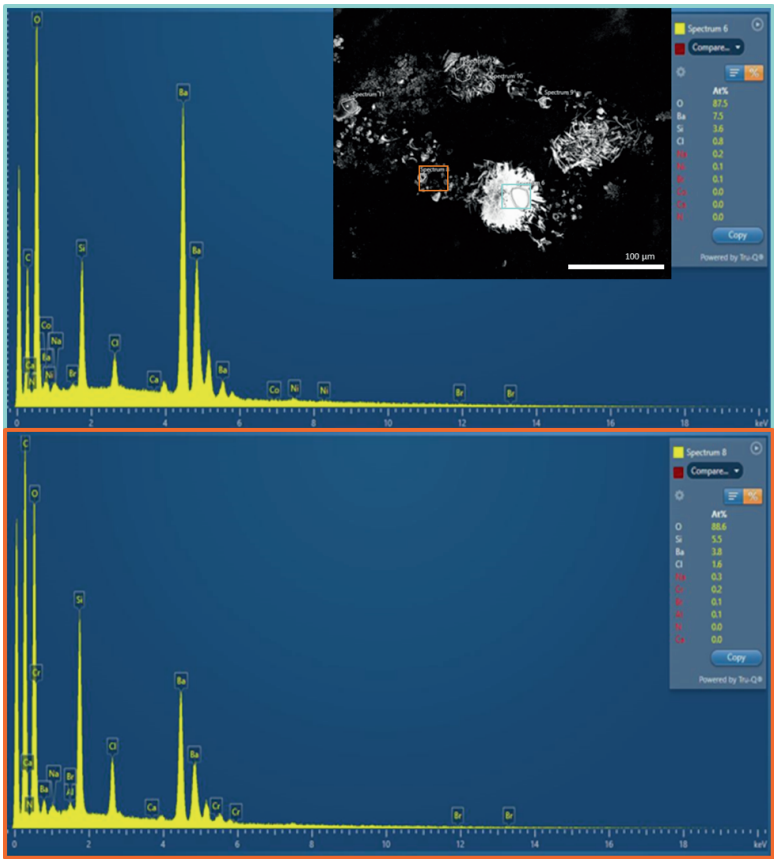

Figure E.6: Full EDX spectra of 532nm ps-pulsed laser-induced precipitation. The precipitation is lifted on a carbon sticker and measured in absence of a silica substrate. Spectrum 6 (top), representing the radial grown structures, indicated by the blue lining in the SEM image, contains 3.6% Si, 7.5% Ba, and 0.8% Cl of atomic weight. Spectrum 8 (bottom), representing the fast precipitation with a moving beam, indicated by orange lining, contains 5.5% Si, 3.8% Ba, and 1.6% Cl of atomic weight.

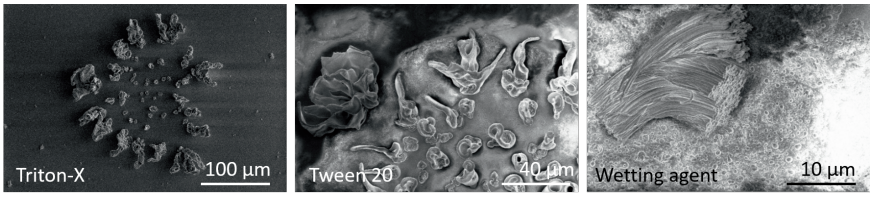

Figure E.7: SEM images of $BaCO_3/SiO_2$ growth upon 365 nm irradiation in presence of A) Triton-x, B) Tween 20, and C) wetting agent 3- hydroxy(polyethyleneoxy)propyl heptamethyltrisiloxane. The samples were used as reference samples to compare with the 532 nm ps-pulsed laser irradiation.

Summary

Controlled self-assembly forms the basis of how organisms construct functional materials in nature. In this process, the intricate interplay of chemical reactions and biophysical environments results in an autonomous mechanism that builds patterns and structures with sub-micrometer precision. These ordered arrangements exhibit advanced optomechanical properties, including strength, toughness, and sensory capabilities. Examples include the alignment of calcium phosphate crystals in teeth, making them the strongest part of the human body, and the alignment of calcite crystals in brittle stars, enabling optical features.

Intrigued by these self-assembling systems, researchers aim to mimic the self-assembly of biorelevant crystals in laboratory settings to gain a deeper understanding of nature and create new functional materials with high-precision. However, achieving control over local gradients that drive self-assembly on the submicro scale, both in time and space, remains challenging in chemical synthesis.

Addressing this challenge, the addition of external stimuli, particularly light-driven reactions, emerges as a promising solution. Light, being clean, precise, selective, and tunable in time and space, opens new opportunities. While light-driven reactions have been demonstrated in (colloidal) crystal self-assembling systems, limited research has been conducted for biorelevant systems, mainly due to the incompatibility of used principles with aqueous systems.

The thesis, titled "Light-controlled self-assembly - Crystallization in the Spotlight," explores the potential of using light-induced reactions in biorelevant crystallization. The exploration includes the use of photochemical reactions with deep ultraviolet (UV) light, vibrational resonance with near-infrared light (1435 nm), and two-photon absorption with a picosecond-pulsed 532 nm laser. Demonstrating the potential of light-driven reactions, the thesis focuses on the co-precipitation of barium carbonate nanocrystals with amorphous silica, and various pure biorelevant minerals such as metal carbonates, calcium phosphates, and strontium sulfates as model systems.

In Chapter 2, we explore the use of a 275 nm UV LED to initiate the photodecarboxylation of ketoprofen (KP). The photoreleased CO_2 creates a local CO_2 gradient, inducing the self-assembly of nanocrystalline $BaCO_3$ and SiO_2 within the UV light spot. Through modulation of the light irradiation intensity, we are able to tune the local CO_2 concentration and disentangle nucleation from growth. Properly balancing the essential reaction, diffusion, and crystallization processes confines this growth within the light

irradiation and allows for light-directed control.

Building on these insights, we utilize photomasks to pattern the light irradiation in a user-defined manner, steering the growth towards this pattern and controlling the contour of its shapes. Furthermore, employing a photomask that projects a field of spots onto the sample enables the nucleation and growth of multiple $BaCO_3/SiO_2$ nanocomposites simultaneously in a patterned arrangement. Additionally, by strategically moving the light spot ahead of the growth of a $BaCO_3/SiO_2$ nanocomposite, we can direct the growth while controlling the development of millimeter-sized structures from nano-sized building blocks.

In Chapter 3, we delve into the nuances of steering the morphology of $BaCO_3/SiO_2$ nanocomposites through the photodecarboxylation of KP. We observe that, in addition to the pH sensitivity of growth, the morphological development heavily relies on the balance in the precipitation rates of $BaCO_3$ and SiO_2, consequently influenced by the local concentration of CO_2. Revisiting the use of photodecarboxylation of KP, we successfully guide the growth mode of the $BaCO_3/SiO_2$ nanocomposites through light modulation.

Specifically, employing high light intensity, corresponding to a heightened local CO_2 concentration, results in outward growth, producing coral-shaped nanocomposites. Conversely, applying lower light intensity (5-10 times) on the same precursor solution, corresponding to a low local CO_2 concentration, induces inward growth, yielding helically-shaped nanocomposites. Furthermore, dynamic modulation and subtle, regular, short, intense adjustments in light intensity enable the growth of hybrid nanocomposites with both coral and helical shape, as well as patterned thickening of the nanocomposites, respectively.

In Chapter 4, we combine the light-directed growth of $BaCO_3/SiO_2$ nanocomposites with an ion exchange conversion reaction. This approach leads to the development of a two-step assembly/conversion method aimed at disentangling and ultimately controlling both shape and composition. Initially, we regulate the nucleation and growth of $BaCO_3/SiO_2$ through the photodecarboxylation of KP. Subsequently, we introduce a compositional change through ion exchange conversion reactions.

Taking into account thermodynamic stability and chemical reactivity, we strategically design orthogonal reaction pathways to sequentially position nanocomposites of different metal chalcogenide semiconductors next to each other. This comprehensive approach also allows us to apply the assembly/conversion method to the same nanocomposite, resulting in the formation of complex hybrid architectures with combined properties attributed to both composition and shape.

In Chapter 5, our focus shifts to pure minerals. The crystallization process of pure minerals proves susceptible to the influence of additional compounds, rendering the use of KP and its required surfactants. To overcome this limitation, we explore the utilization of 1435 nm light, resonating with the first overtone of water -generating heat in combination with retrograde solubile mineral compounds.

Employing a laser diode with a 180 mW laser output focused on a spot with a 15 radius on an aqueous sample, we observe an almost instantaneous temperature increase of up to approximately 100 °C within the focal spot of the laser. Capitalizing on this temperature surge, we can locally induce the nucleation and growth of biorelevant crystals with retrograde solubility- a decreasing solubility as temperatures rise- such as metal carbonates, calcium phosphate, and strontium sulfate. We discover that modulation of light intensity facilitates control over nucleation independent of growth. Furthermore, we establish that this method complements established techniques for controlling polymorphism, allowing us to position the three polymorphs of $CaCO_3$ next to each other.

In Chapter 6, we present the preliminary results of employing a picosecond-pulsed 532 nm laser. The utilization of such a laser allows us to generate exceptionally high peak intensities in the focal spot, capable of inducing non-linear optical effects, including two-photon absorption. Our exploration aims to determine whether this property can be harnessed to facilitate two-photon absorption, thereby inducing the photodecarboxylation of KP and initiating the nucleation and growth of $BaCO_3/SiO_2$ nanocomposites with three-dimensional (3D) control.

Upon reaching sufficiently high levels of peak intensity and pulse rate, we observe the local precipitation resembling the $BaCO_3/SiO_2$ nanocomposites. Moreover, we successfully direct this precipitation in the *z*-direction and even apply ion conversion reactions to it. However, alongside the desired precipitation of $BaCO_3/SiO_2$ nanocomposites, we observe additional unidentified precipitation that, upon inspection with Raman spectroscopy, result peaks corresponding to silicate-like species and disordered carbon. This discovery necessitates further optimization and analysis of the proposed method.

In conclusion, this work represents the initial strides in developing spatiotemporal controlled artificial self-assembly systems. We demonstrate the feasibility of utilizing light for controlled, biorelevant crystallization, albeit with the caveat that all technical and chemical elements must align, as outlined in Chapter 7. We anticipate that these findings can be extrapolated to regulate nucleation and growth across a diverse array of biorelevant minerals and functional crystals, including perovskites, employing similar light-induced, photochemical, and non-photochemical reactions.

Moreover, the implications of this research extend to potentially influencing the advancement of carbonate-silica nanocomposites as a versatile platform for functional materials. This could pave the way for an unprecedented application of artificial self-organization processes in materials science. With that, we introduce new perspectives on the fabrication techniques of functional materials, opening up opportunities for innovative approaches in the field where we employ precise hands-on command when necessary, and simple hands-off autonomy when possible.

Samenvatting

Gecontroleerde zelfassemblage vormt de basis van de bouw van functionele materialen door natuurlijke organismen. In dit proces resulteert het ingewikkelde samenspel van chemische reacties en biofysische omgevingen in een autonoom mechanisme dat patronen en structuren bouwt met submicrometer-precisie. Deze geordende arrangementen vertonen geavanceerde optomechanische eigenschappen, waaronder sterkte, hardheid en sensorische vermogens. Voorbeelden hiervan zijn de uitlijning van calciumfosfaatkristallen in tanden, die ze het sterkste deel van het menselijk lichaam vormen, en de ordening van calcietkristallen in zeesterren, die optische eigenschappen mogelijk maakt.

Geïntrigeerd door deze zelfassemblerende systemen willen onderzoekers de zelfassemblage van biorelevante kristallen in laboratoria nabootsen om de natuur beter te begrijpen en nieuwe functionele materialen met hoge precisie te maken. Echter, het bereiken van controle over de lokale gradiënten drijven zelf-assemblage op submicroschaal, zowel in termen van tijd en ruimte, blijft een uitdaging in de chemische synthese.

Het gebruiken van externe stimuli, met name lichtgestuurde reacties, lijkt een veelbelovende aanpak te zijn. Licht, dat schoon, precies, selectief en afstembaar is in tijd en ruimte, opent nieuwe mogelijkheden. Hoewel lichtgestuurde reacties zijn toegepast in (colloïdale) kristal zelfassemblerende systemen, is er beperkt onderzoek gedaan naar biorelevante systemen, voornamelijk vanwege de incompatibiliteit van de gebruikte principes met waterige systemen.

Het proefschrift, getiteld "Light-controlled self-assembly - Crystallization in the spotlight", onderzoekt de potentie van het gebruik van lichtgeïnduceerde reacties in biorelevante kristallisatie. Het onderzoek omvat het gebruik van fotochemische reacties met diep ultraviolet (UV) licht, vibratieresonantie met nabij-infrarood licht (1435 nm) en tweefotonabsorptie met een picoseconde gepulste 532 nm laser. Om het potentieel van lichtgestuurde reacties aan te tonen, richt het proefschrift zich op coprecipitatieprocessen met bariumcarbonaat nanokristallen, amorf silica en verschillende zuiver biorelevante mineralen zoals metaalcarbonaten, calciumfosfaten en strontiumsulfaten als modelsystemen.

In hoofdstuk 2 onderzoeken we het gebruik van een 275 nm UV-LED om de fotodecarboxylering van ketoprofen (KP) te starten. De vrijgekomen CO_2 creëert een lokale CO_2 gradiënt, waardoor de zelfassemblage van nanokristallijne $BaCO_3$ en SiO_2 binnen de UV-lichtvlek geïnduceerd wordt. Door de intensiteit van de lichtbestraling te moduleren, kunnen we de lokale CO_2-concentratie afstemmen en nucleatie en groei van elkaar scheiden. Door de essentiële reactie-, diffusie- en kristallisatieprocessen goed

in balans te brengen, wordt deze groei beperkt tot de bestraalde ruimte en is lichtgerichte controle mogelijk.

Voortbouwend op deze inzichten gebruiken we fotomaskers om een patroon te maken van de lichtbestraling op een door de gebruiker gedefinieerde manier, waarbij de groei naar dit patroon wordt gestuurd en de contouren van de vormen worden beheerst. Door gebruik te maken van een fotomasker dat een patroon van lichtplekken op het monster projecteert, kunnen meerdere $BaCO_3/SiO_2$ nanocomposieten gelijktijdig in een patroon groeien. Bovendien kunnen we, door de lichtspot strategisch te verplaatsen voor de groei van een $BaCO_3/SiO_2$ nanocomposiet, de groei sturen en tegelijkertijd de ontwikkeling van millimetergrote structuren uit nanometergrote bouwstenen controleren.

In hoofdstuk 3 gaan we dieper in op de nuances van het sturen van de morfologie van $BaCO_3/SiO_2$ nanocomposieten door de fotodecarboxylering van KP. We stellen vast dat naast de pH-gevoeligheid van de groei de morfologische ontwikkeling sterk afhankelijk is van de ratio in de neerslagsnelheden van $BaCO_3$ en SiO_2, en dus beïnvloed wordt door de plaatselijke CO_2-concentratie. Door opnieuw gebruik te maken van fotodecarboxylering van KP hebben we met succes de groeimodus gestuurd door lichtmodulatie.

Het gebruik van een hoge lichtintensiteit, die verhoogde lokale CO_2-concentratie geeft, resulteert in naar buiten gerichte groei, waarbij koraalvormige nanocomposieten ontstaan. Omgekeerd leidt het toepassen van een lagere lichtintensiteit (5-10 keer) op dezelfde precursoroplossing, wat overeenkomt met een lage plaatselijke CO_2-concentratie, tot inwaartse groei, wat schroefvormige nanocomposieten oplevert. Verder maken dynamische modulatie en subtiele, regelmatige, korte, intense aanpassingen van de lichtintensiteit de groei van hybride nanocomposieten met zowel koraal- als spiraalvormige groei mogelijk, evenals een patroonvormige verdikking van de nanocomposieten.

In hoofdstuk 4 integreren we de lichtgerichte groei van $BaCO_3/SiO_2$ nanocomposieten met een omzetting via ionenuitwisselings. Deze benadering leidt tot de ontwikkeling van een assemblage/conversie methode in twee stappen die gericht is op het ontwarren en uiteindelijk controleren van zowel vorm als samenstelling. In eerste instantie reguleren we de nucleatie en groei van $BaCO_3/SiO_2$ door de fotodecarboxylering van KP. Vervolgens introduceren we een verandering in samenstelling door omzettingsreacties met ionenuitwisseling.

Rekening houdend met thermodynamische stabiliteit en chemische reactiviteit, ontwerpen we strategisch orthogonale reactiepaden om nanocomposieten van verschillende metaalchalcogenide halfgeleiders achtereenvolgens naast elkaar te plaatsen.Deze uitgebreide aanpak stelt ons in staat om de assemblage/conversie methode toe te passen op hetzelfde nanocomposiet, wat resulteert in de vorming van complexe hybride architecturen met gecombineerde eigenschappen die worden toegeschreven aan zowel samenstelling als vorm.

In hoofdstuk 5 verschuift onze aandacht naar de kristalsystemen van zuivere mineralen. Het kristallisatieproces van pure mineralen blijkt gevoelig te zijn voor de invloed van additieven, waardoor het gewenst is

om hydrofobe verbindingen zoals KP en de benodigde oppervlakteactieve stoffen te vermijden. Om deze beperking te overwinnen, onderzoeken we het gebruik van 1435 nm licht, resonerend met de eerste boventoon van water, dat warmte genereert. Deze warmte gebruiken we in combinatie met de groei van mineralen die een verminderde oplosbaarheid vertonen bij hogere temperaturen.

Door gebruik te maken van een laserdiode met een laservermogen van 180 mW, gericht op een punt met een straal van 15 micrometer op een waterig monster, observeren we een bijna ogenblikkelijke temperatuurstijging tot ongeveer 100 °C binnen het brandpunt van de laser. Door gebruik te maken van deze temperatuurstijging kunnen we lokaal de nucleatie en groei van biorelevante kristallen met retrograde oplosbaarheid (een afnemende oplosbaarheid bij stijgende temperatuur) opwekken, zoals metaalcarbonaten, calciumfosfaat en strontiumsulfaat. We ontdekken dat modulatie van de lichtintensiteit controle over de nucleatie vergemakkelijkt, onafhankelijk van de groei. Verder stellen we vast dat deze methode een aanvulling is op gevestigde technieken om polymorfisme te sturen, waardoor we de drie polymorfen van $CaCO_3$ naast elkaar kunnen plaatsen.

In hoofdstuk 6 presenteren we de eerste resultaten van het gebruik van een picoseconde gepulste 532 nm laser. Het gebruik van een dergelijke laser stelt ons in staat om uitzonderlijk hoge piekintensiteiten te genereren in het brandpunt, waardoor niet-lineaire optische effecten kunnen worden opgewekt, waaronder tweefotonabsorptie. Ons onderzoek is erop gericht om te bepalen of deze eigenschap kan worden gebruikt om tweefotonabsorptie te vergemakkelijken, waardoor de fotodecarboxylering van KP wordt geïnduceerd en de nucleatie en groei van $BaCO_3/SiO_2$ nanocomposieten met driedimensionale (3D) controle wordt geïnitieerd.

Bij het bereiken van voldoende hoge niveaus van piekintensiteit en pulsfrequentie, observeren we de lokale neerslag die lijkt op de $BaCO_3/SiO_2$ nanocomposieten. Bovendien richten we deze neerslag met succes in de *z*-richting en passen we er zelfs ionenconversiereacties op toe. Naast de gewenste neerslag van $BaCO_3/SiO_2$ nanocomposieten, observeren we echter bijkomende niet-geïdentificeerde neerslag met Raman-pieken van silicaatachtige materialen en ongeordende koolstof. Deze ontdekking vereist verdere optimalisatie en analyse van de voorgestelde methode.

Samenvattend, presenteert dit werk de eerste stappen in de ontwikkeling van spatiotemporele gecontroleerde kunstmatige zelf-assemblage systemen. We tonen de haalbaarheid aan van het gebruik van licht voor gecontroleerde, biorelevante kristallisatie, zij het met het voorbehoud dat alle technische en chemische elementen op elkaar moeten zijn afgestemd, zoals beschreven in hoofdstuk 7.

We verwachten dat deze bevindingen geëxtrapoleerd kunnen worden om nucleatie en groei te reguleren in een breed scala aan biorelevante mineralen en functionele kristallen, waaronder perovskieten, door gebruik te maken van vergelijkbare lichtgeïnduceerde, fotochemische en niet-fotochemische reacties. De implicaties van dit onderzoek strekken zich bovendien uit tot het mogelijk beïnvloeden van de ontwikkeling van carbonaat-silicaat nanocomposieten als een veelzijdig platform voor functionele materialen. Dit zou het pad kunnen effenen voor een ongekende toepassing van kunstmatige zelforganiserende processen in de materiaalkunde. Daarmee introduceren we nieuwe perspectieven op de

fabricagetechnieken van functionele materialen, wat mogelijkheden biedt voor innovatieve benaderingen op dit gebied, waarbij we nauwkeurige *hands-on* besturing toepassen wanneer dat nodig is, en eenvoudige *hands-off* autonomie wanneer dat mogelijk is.

List of publications

1. **Bistervels, M. H.**, Kamp, M., Schoenmaker, H., Brouwer, A. M., & Noorduin, W. L. (2022). Light-Controlled Nucleation and Shaping of Self-Assembling Nanocomposites. *Advanced Materials*, 34 (5), 2107843.
2. **Bistervels, M. H.**, Antalicz, B., Kamp, M., Schoenmaker, H., & Noorduin, W. L. (2023). Light-driven nucleation, growth, and patterning of biorelevant crystals using resonant near-infrared laser heating. *Nature Communications*, 14 (1), 6350.
3. **Bistervels, M. H.**, Hoogendoorn, N. T., Kamp, M., Schoenmaker, H., Brouwer, A. M., & Noorduin, W. L. (2024). Light-controlled morphological development of self-organizing bioinspired nanocomposite. *Nanoscale*, 16, 2310.
4. **Bistervels, M. H.**, van der Weijden, A., Kamp, M., Schoenmaker, & Noorduin, W. L. (2024). Compose and convert: Controlling shape and chemical composition of self-organizing nanocomposites. *Advanced Functional Materials*, 2403715.
5. Helmbrecht, L., Tan, M., Röhrich, R., **Bistervels, M. H.**, Kessels, B. O., Koenderink, A. F., & Noorduin, W. L. (2020). Self-Assembled Microhelices: Directed Emission from Self-Assembled Microhelices. *Advanced Functional Materials, 30(26)*, 2070165.
6. van Campenhout, C., **Bistervels, M. H.**, Rietveld, J., Kamp, M., Schoenmaker, & Noorduin, W. L. (2024). Designing complex tapestries with photography inspired manipulation of self-organized thin-films *Advanced Science*, 2401625.

Bibliography

1. Beniash, E. *et al.* The hidden structure of human enamel. *Nature Communications* **10,** 4383 (2019).
2. Mass, T. *et al.* Amorphous calcium carbonate particles form coral skeletons. *Proceedings of the National Academy of Sciences of the United States of America* **114,** E7670–E7678 (2017).
3. Connors, M. *et al.* Bioinspired design of flexible armor based on chiton scales. *Nature communications* **10,** 5413 (2019).
4. Aizenberg, J., Tkachenko, A., Weiner, S., Addadi, L. & Hendler, G. Calcitic microlenses as part of the photoreceptor system in brittlestars. *Nature* **412,** 819–822 (2001).
5. Lowenstam, H. A. & Weiner, S. *On Biomineralization* (Oxford University Press, New York, USA, 1989).
6. Yang, T. *et al.* A damage-tolerant, dual-scale, single-crystalline microlattice in the knobby starfish, Protoreaster nodosus. *Science* **375,** 647–652 (2022).
7. Addadi, L. & Weiner, S. Biomineralization: Mineral formation by organisms. *Physica Scripta* **89** (2014).
8. Gilbert, P. U. P. A. *et al.* Biomineralization: Integrating mechanism and evolutionary history. *Science Advances* **8,** eabl9653 (2022).
9. Akiva, A. *et al.* Mineral Formation in the Larval Zebrafish Tail Bone Occurs via an Acidic Disordered Calcium Phosphate Phase. *Journal of the American Chemical Society* **138,** 14481–14487 (2016).
10. Kröger, N., Brunner, E., Estroff, L. & Marin, F. The role of organic matrices in biomineralization. *Discover Materials* **1,** 1–4 (2021).
11. Meldrum, F. C. & Colfen, H. Controlling mineral morphologies and structures in biological and synthetic systems. *Chemical reviews* **108,** 4332–4432 (2008).
12. Aizenberg, J. & Fratzl, P. Biological and biomimetic materials. *Advanced Materials* **21,** 387–388 (2009).
13. Nudelman, F. & Sommerdijk, N. A. Biomineralization as an inspiration for materials chemistry. *Angewandte Chemie - International Edition* **51,** 6582–6596 (2012).
14. Huang, W. *et al.* Multiscale Toughening Mechanisms in Biological Materials and Bioinspired Designs. *Advanced Materials* **31,** 1–37 (2019).
15. Rao, A. & Cölfen, H. *Morphology Control and Molecular Templates in Biomineralization* 51–93 (Elsevier Ltd., 2016).
16. Nepal, D. *et al.* Hierarchically structured bioinspired nanocomposites. *Nature Materials* **22,** 18–35 (2023).
17. Mann, S. The Chemistry of Form. *Angew.Chem.Int.Ed* **39,** 3392–3406 (2000).
18. Whitesides, G. M. & Grzybowski, B. Self-assembly at all scales. *Science* **295,** 2418–2421 (2002).

19. Arakaki, A. *et al.* Biomineralization-inspired synthesis of functional organic/inorganic hybrid materials: Organic molecular control of self-organization of hybrids. *Organic and Biomolecular Chemistry* **13,** 974–989 (2015).
20. Liu, Z., Meyers, M. A., Zhang, Z. & Ritchie, R. O. Functional gradients and heterogeneities in biological materials: Design principles, functions, and bioinspired applications. *Progress in Materials Science* **88,** 467–498 (2017).
21. Begley, M. R., Gianola, D. S. & Ray, T. R. Bridging functional nanocomposites to robust macroscale devices. *Science* **364,** eaav4299 (2019).
22. Kundu, P. K. *et al.* Light-controlled self-assembly of non-photoresponsive nanoparticles. *Nature chemistry* **7,** 646–652 (2015).
23. Bian, T., Chu, Z. & Klajn, R. The many ways to assemble nanoparticles using light. *Advanced Materials* **32,** 1905866 (2020).
24. Li, S. *et al.* Self-regulated non-reciprocal motions in single-material microstructures. *Nature* **605,** 76–83 (2022).
25. Korede, V. *et al.* A Review of Laser-Induced Crystallization from Solution. *Crystal Growth & Design* **23,** 3873–3916 (2023).
26. Mann, S. Biomineralization and biomimetic materials chemistry. *Journal of Materials Chemistry* **5,** 935–946 (1995).
27. Elsharkawy, S. & Mata, A. Hierarchical Biomineralization: from Nature's Designs to Synthetic Materials for Regenerative Medicine and Dentistry. *Advanced Healthcare Materials* **7,** 1–19 (2018).
28. Addadi, L. & Weiner, S. Control and design principles in biological mineralization. *Angewandte Chemie International Edition in English* **31,** 153–169 (1992).
29. Aizenberg, J. New nanofabrication strategies: inspired by biomineralization. *MRS bulletin* **35,** 323–330 (2010).
30. Song, R.-Q. & Cölfen, H. Additive controlled crystallization. *CrystEngComm* **13,** 1249–1276 (2011).
31. Cho, K. R. *et al.* The effects of different types of additives on growth of biomineral phases investigated by in situ atomic force microscopy. *Journal of Crystal Growth* **509,** 8–16 (2019).
32. Hopwood, J. D. & Mann, S. Synthesis of barium sulfate nanoparticles and nanofilaments in reverse micelles and microemulsions. *Chemistry of Materials* **9,** 1819–1828 (1997).
33. Shi, J., Alves, N. M. & Mano, J. F. Thermally responsive biomineralization on biodegradable substrates. *Advanced Functional Materials* **17,** 3312–3318 (2007).
34. Driessens, F. C. & Verbeeck, R. *Biominerals* (CRC press, 1990).
35. Kontrec, J., Tomašić, N., Matijaković Mlinarić, N., Kralj, D. & Njegić Džakula, B. Effect of pH and Type of Stirring on the Spontaneous Precipitation of $CaCO_3$ at Identical Initial Supersaturation, Ionic Strength and a (Ca^{2+})/a (CO_32-) Ratio. *Crystals* **11,** 1075 (2021).
36. Buljan Meic, I. *et al.* Comparative study of calcium carbonates and calcium phosphates precipitation in model systems mimicking the inorganic environment for biomineralization. *Crystal Growth & Design* **17,** 1103–1117 (2017).
37. Zhao, R. *et al.* Additive manufacturing of porous biominerals. *Advanced Functional Materials* **33,** 2300950 (2023).
38. Wegst, U. G., Bai, H., Saiz, E., Tomsia, A. P. & Ritchie, R. O. Bioinspired structural materials. *Nature Materials* **14,** 23–36 (2015).
39. Beniash, E. Biominerals—hierarchical nanocomposites: the example of bone. *Wiley Interdisciplinary Reviews: Nanomedicine and Nanobiotechnology* **3,** 47–69 (2011).

40. Eimar, H. *et al.* Regulation of enamel hardness by its crystallographic dimensions. *Acta biomaterialia* **8,** 3400–3410 (2012).
41. Mullin, J. W. *Crystallization* (Elsevier, 2001).
42. De Yoreo, J. J. & Vekilov, P. G. Principles of crystal nucleation and growth. *Reviews in mineralogy and geochemistry* **54,** 57–93 (2003).
43. Becker, R. & Döring, W. Kinetische behandlung der keimbildung in übersättigten dämpfen. *Annalen der physik* **416,** 719–752 (1935).
44. Volmer, M. & Weber, A. Keimbildung in übersättigten Gebilden. *Zeitschrift für physikalische Chemie* **119,** 277–301 (1926).
45. Smeets, P. J. *et al.* A classical view on nonclassical nucleation. *Proceedings of the National Academy of Sciences* **114,** E7882–E7890 (2017).
46. De Yoreo, J. J. *et al.* Crystallization by particle attachment in synthetic, biogenic, and geologic environments. *Science* **349,** aaa6760 (2015).
47. Gibbs, J. W. On the equilibrium of heterogeneous substances. *American journal of science* **3,** 441–458 (1878).
48. Lauer, A. R., Durán-Olivencia, M., Fernandez-Martinez, A. & Van Driessche, A. E. Multistep nucleation compatible with a single energy barrier: catching the non-classical culprit. *Faraday Discussions* **235,** 95–108 (2022).
49. Turnbull, D. Formation of crystal nuclei in liquid metals. *Journal of Applied Physics* **21,** 1022–1028 (1950).
50. Gebauer, D. & Cölfen, H. Prenucleation clusters and non-classical nucleation. *Nano Today* **6,** 564–584 (2011).
51. Li, D. *et al.* Direction-specific interactions control crystal growth by oriented attachment. *Science* **336,** 1014–1018 (2012).
52. Schwahn, D., Ma, Y. & Cölfen, H. Mesocrystal to single crystal transformation of D, L-alanine evidenced by small angle neutron scattering. *The Journal of Physical Chemistry C* **111,** 3224–3227 (2007).
53. Sommerdijk, N. A. & de With, G. Biomimetic $CaCO_3$ mineralization using designer molecules and interfaces. *Chemical Reviews* **108,** 4499–4550 (2008).
54. Erez, J. Vital effect on stable-isotope composition seen in foraminifera and coral skeletons. *Nature* **273,** 199–202 (1978).
55. Meldrum, F. Calcium carbonate in biomineralisation and biomimetic chemistry. *International Materials Reviews* **48,** 187–224 (2003).
56. Chan, K. & Heenan, D. Effect of lime ($CaCO_3$) application on soil structural stability of a red earth. *Soil Research* **36,** 73–86 (1998).
57. Cho, S. H. *et al.* Synthesis of precipitated calcium carbonate using a limestone and its application in paper filler and coating color. **544,** 881–884 (2007).
58. Matschei, T., Lothenbach, B & Glasser, F. P. The role of calcium carbonate in cement hydration. *Cement and concrete research* **37,** 551–558 (2007).
59. Augsburger, L. L. & Hoag, S. W. *Pharmaceutical dosage forms-tablets* (CRC press, 2016).
60. Al Omari, M., Rashid, I., Qinna, N., Jaber, A. & Badwan, A. Calcium carbonate. *Profiles of drug substances, excipients and related methodology* **41,** 31–132 (2016).
61. Lippmann, F. & Lippmann, F. *Crystal chemistry of sedimentary carbonate minerals* (Springer, 1973).
62. Gower, L. B. Biomimetic model systems for investigating the amorphous precursor pathway and its role in biomineralization. *Chemical reviews* **108,** 4551–4627 (2008).

63. Li, L, Fijneman, A., Kaandorp, J., Aizenberg, J. & Noorduin, W. Directed nucleation and growth by balancing local supersaturation and substrate/nucleus lattice mismatch. *Proceedings of the National Academy of Sciences* **115,** 3575–3580 (2018).
64. Tushtev, K., Murck, M. & Grathwohl, G. On the nature of the stiffness of nacre. *Materials Science and Engineering: C* **28,** 1164–1172 (2008).
65. Aizenberg, J., Muller, D. A., Grazul, J. L. & Hamann, D. Direct fabrication of large micropatterned single crystals. *Science* **299,** 1205–1208 (2003).
66. Anwar, J., Boateng, P. K., Tamaki, R. & Odedra, S. Mode of action and design rules for additives that modulate crystal nucleation. *Angewandte Chemie* **121,** 1624–1628 (2009).
67. Titiloye, J., Parker, S. & Mann, S. Atomistic simulation of calcite surfaces and the influence of growth additives on their morphology. *Journal of Crystal Growth* **131,** 533–545 (1993).
68. Meldrum, F. C. & Hyde, S. T. Morphological influence of magnesium and organic additives on the precipitation of calcite. *Journal of crystal growth* **231,** 544–558 (2001).
69. Jiang, W. *et al.* Chiral acidic amino acids induce chiral hierarchical structure in calcium carbonate. *Nature communications* **8,** 15066 (2017).
70. Kato, T., Sakamoto, T. & Nishimura, T. Macromolecular templating for the formation of inorganic-organic hybrid structures. *MRS bulletin* **35,** 127–132 (2010).
71. Davila Hernandez, F. A. *et al.* Directing polymorph specific calcium carbonate formation with de novo protein templates. *bioRxiv,* 2023–06 (2023).
72. Champ, S., Dickinson, J. A., Fallon, P. S., Heywood, B. R. & Mascal, M. Hydrogen-Bonded Molecular Ribbons as Templates for the Synthesis of Modified Mineral Phases. *Angewandte Chemie* **112,** 2828–2831 (2000).
73. Aizenberg, J., Black, A. J. & Whitesides, G. M. Control of crystal nucleation by patterned self-assembled monolayers. *Nature* **398,** 495–498 (1999).
74. Finnemore, A. S. *et al.* Nanostructured calcite single crystals with gyroid morphologies. *Advanced Materials* **21,** 3928–3932 (2009).
75. Uchida, M. *et al.* Biological containers: protein cages as multifunctional nanoplatforms. *Advanced Materials* **19,** 1025–1042 (2007).
76. Gong, X. *et al.* The crystal hotel: a microfluidic approach to biomimetic crystallization. *Advanced Materials* **27,** 7395 (2015).
77. Park, R. J. & Meldrum, F. C. Synthesis of single crystals of calcite with complex morphologies. *Advanced Materials* **14,** 1167–1169 (2002).
78. Du, H. *et al.* Additives: their influence on the humidity-and pressure-induced crystallization of amorphous $CaCO_3$. *Chemistry of Materials* **32,** 4282–4291 (2020).
79. Finnemore, A. *et al.* Biomimetic layer-by-layer assembly of artificial nacre. *Nature communications* **3,** 966 (2012).
80. Garcia-Ruiz, J. M., Melero-Garcia, E. & Hyde, S. T. Morphogenesis of Self-Assembled Nanocrystalline Materials of Barium Carbonate and Silica. *Science* **323,** 362–365 (2009).
81. Kellermeier, M., Cölfen, H. & García-Ruiz, J. M. Silica biomorphs: Complex biomimetic hybrid materials from "sand and chalk". *European Journal of Inorganic Chemistry* **2012,** 5123–5144 (2012).
82. Terada, T., Yamabi, S. & Imai, H. Formation process of sheets and helical forms consisting of strontium carbonate fibrous crystals with silicate. *Journal of Crystal Growth* **253,** 435–444 (2003).
83. Noorduin, W. L., Grinthal, A., Mahadevan, L. & Aizenberg, J. Rationally designed complex, hierarchical microarchitectures. *Science* **340,** 832–837 (2013).

84. Holtus, T. *et al.* Shape-preserving transformation of carbonate minerals into lead halide perovskite semiconductors based on ion exchange/insertion reactions. *Nature Chemistry* **10,** 740–745 (2018).
85. Helmbrecht, L. *et al.* Directed Emission from Self-Assembled Microhelices. *Advanced Functional Materials* **30,** 1–5 (2020).
86. Hendrikse, H. C. *et al.* Shape-Preserving Chemical Conversion of Architected Nanocomposites. *Advanced materials* **32,** 2003999 (2020).
87. Knoll, P. & Steinbock, O. Inorganic Reactions Self-organize Life-like Microstructures Far from Equilibrium. *Israel Journal of Chemistry* **58,** 682–692 (2018).
88. Opel, J. *et al.* Probing local pH-based precipitation processes in self-assembled silica-carbonate hybrid materials. *Nanoscale* **7,** 17434–17440 (2015).
89. Montalti, M. *et al.* Local pH oscillations witness autocatalytic self-organization of biomorphic nanostructures. *Nature Communications* **8,** 1–6 (2017).
90. Bittarello, E. & Aquilano, D. Self-assembled nanocrystals of barium carbonate in biomineral-like structures. *European Journal of Mineralogy* **19,** 345–351 (2007).
91. Nakouzi, E., Rendina, R., Palui, G. & Steinbock, O. Effect of inorganic additives on the growth of silica–carbonate biomorphs. *Journal of Crystal Growth* **452,** 166–171 (2016).
92. Opel, J. *et al.* Structural transition of inorganic silica–carbonate composites towards curved lifelike morphologies. *Minerals* **8,** 75 (2018).
93. Kellermeier, M. *et al.* Evolution and control of complex curved form in simple inorganic precipitation systems. *Crystal growth & design* **12,** 3647–3655 (2012).
94. Knoll, P., D'Silva, D. S., Adeoye, D. I., Roper, M. G. & Steinbock, O. Fibrous Bundles in Biomorph Systems: Surface-Specific Growth and Interaction with Microposts. *ChemSystemsChem* **3,** e2000061 (2021).
95. Xiang, X.-F., Li, P.-J. & Liu, B.-F. tuning the Superhydrophobic properties of Hierarchical nano-microstructural Silica Biomorph Arrays Grown at triphasic interfaces. *Scientific Reports* **10,** 4596 (2020).
96. Opel, J. *et al.* Symbiosis of silica biomorphs and magnetite mesocrystals. *Advanced Functional Materials* **29,** 1902047 (2019).
97. Opel, J., Wimmer, F. P., Kellermeier, M. & Cölfen, H. Functionalisation of silica–carbonate biomorphs. *Nanoscale Horizons* **1,** 144–149 (2016).
98. Opel, J. *et al.* Light-switchable anchors on magnetized biomorphic microcarriers. *Journal of Materials Chemistry B* **8,** 4831–4835 (2020).
99. Opel, J. *et al.* Hybrid biomimetic materials from silica/carbonate biomorphs. *Crystals* **9,** 157 (2019).
100. Hendrikse, H. C. *et al.* Rational Design of Bioinspired Nanocomposites with Tunable Catalytic Activity. *Crystal Growth and Design* **21,** 4299–4304 (2021).
101. Hendrikse, H. C. *et al.* Shaping Tin Nanocomposites through Transient Local Conversion Reactions. *Crystal Growth and Design* **21,** 4500–4505 (2021).
102. Weissenfels, M., Gemen, J. & Klajn, R. Dissipative self-assembly: fueling with chemicals versus light. *Chem* **7,** 23–37 (2021).
103. Li, J. & Jia, X. Photo-Controlled Self-Assembly of Nanoparticles: A Promising Strategy for Development of Novel Structures. *Nanomaterials* **13,** 2562 (2023).
104. Jia, X. & Zhu, L. Photoexcitation-Induced Assembly: A Bottom-Up Physical Strategy for Driving Molecular Motion and Phase Evolution. *Accounts of Chemical Research* **56,** 655–666 (2023).
105. Hoffmann, N. Photochemical reactions as key steps in organic synthesis. *Chemical reviews* **108,** 1052–1103 (2008).

106. Kuznetsova, N. A., Malkov, G. V. & Gribov, B. G. Photoacid generators. Application and current state of development. *Russian chemical reviews* **89,** 173 (2020).
107. Wu, T. *et al.* Photoinduced bulk polarization and its effects on photovoltaic actions in perovskite solar cells. *ACS nano* **11,** 11542–11549 (2017).
108. Bandara, H. D. & Burdette, S. C. Photoisomerization in different classes of azobenzene. *Chemical Society Reviews* **41,** 1809–1825 (2012).
109. DeForest, C. A. & Anseth, K. S. Cytocompatible click-based hydrogels with dynamically tunable properties through orthogonal photoconjugation and photocleavage reactions. *Nature chemistry* **3,** 925–931 (2011).
110. Cheng, H.-B. *et al.* Future-Oriented Advanced Diarylethene Photoswitches: From Molecular Design to Spontaneous Assembly Systems. *Advanced Materials* **34,** 2108289 (2022).
111. Cheng, H.-B., Zhang, S., Qi, J., Liang, X.-J. & Yoon, J. Advances in application of azobenzene as a trigger in biomedicine: Molecular design and spontaneous assembly. *Advanced Materials* **33,** 2007290 (2021).
112. Klajn, R. Spiropyran-based dynamic materials. *Chemical Society Reviews* **43,** 148–184 (2014).
113. Klajn, R., Wesson, P. J., Bishop, K. J. & Grzybowski, B. A. Writing self-erasing images using metastable nanoparticle "inks". *Angewandte Chemie International Edition* **48,** 7035–7039 (2009).
114. Liu, D. *et al.* Resettable, multi-readout logic gates based on controllably reversible aggregation of gold nanoparticles. *Angewandte Chemie International Edition* **50,** 4103–4107 (2011).
115. Mukherjee, A., Seyfried, M. D. & Ravoo, B. J. Azoheteroarene and Diazocine Molecular Photoswitches: Self-Assembly, Responsive Materials and Photopharmacology. *Angewandte Chemie International Edition* **62,** e202304437 (2023).
116. Stricker, L., Fritz, E.-C., Peterlechner, M., Doltsinis, N. L. & Ravoo, B. J. Arylazopyrazoles as light-responsive molecular switches in cyclodextrin-based supramolecular systems. *Journal of the American Chemical Society* **138,** 4547–4554 (2016).
117. Yucknovsky, A., Mondal, S., Burnstine-Townley, A., Foqara, M. & Amdursky, N. Use of photoacids and photobases to control dynamic self-assembly of gold nanoparticles in aqueous and nonaqueous solutions. *Nano Letters* **19,** 3804–3810 (2019).
118. Kagel, H., Frohme, M. & Glökler, J. Photoacids in biochemical applications. *Journal of Cellular Biotechnology* **4,** 23–30 (2018).
119. Martin, C. J., Rapenne, G., Nakashima, T. & Kawai, T. Recent progress in development of photoacid generators. *Journal of Photochemistry and Photobiology C: Photochemistry Reviews* **34,** 41–51 (2018).
120. Shirai, M. & Tsunooka, M. Photoacid and photobase generators: chemistry and applications to polymeric materials. *Progress in polymer science* **21,** 1–45 (1996).
121. Li, S. *et al.* Facile preparation of diversified patterns of calcium carbonate in the presence of DTAB. *Journal of crystal growth* **312,** 1766–1773 (2010).
122. Huynh, T. P., Pedersen, C., Wittig, N. K. & Birkedal, H. Precipitation of Inorganic Phases through a Photoinduced pH Jump: From Vaterite Spheroids and Shells to ZnO Flakes and Hexagonal Plates. *Crystal Growth and Design* **18,** 1951–1955 (2018).
123. Garetz, B., Aber, J., Goddard, N., Young, R. & Myerson, A. Nonphotochemical, polarization-dependent, laser-induced nucleation in supersaturated aqueous urea solutions. *Physical review letters* **77,** 3475 (1996).
124. Alexander, A. J. & Camp, P. J. Non-photochemical laser-induced nucleation. *The Journal of chemical physics* **150** (2019).

125. Ashkin, A., Dziedzic, J. M., Bjorkholm, J. E. & Chu, S. Observation of a single-beam gradient force optical trap for dielectric particles. *Optics letters* **11,** 288–290 (1986).
126. Masuhara, H., Sugiyama, T., Yuyama, K.-i. & Usman, A. Optical trapping assembling of clusters and nanoparticles in solution by CW and femtosecond lasers. *Optical Review* **22,** 143–148 (2015).
127. Vogel, A., Noack, J, Hüttman, G & Paltauf, G. Mechanisms of femtosecond laser nanosurgery of cells and tissues. *Applied physics B* **81,** 1015–1047 (2005).
128. Sugiyama, T. & Wang, S.-F. Manipulation of nucleation and polymorphism by laser irradiation. *Journal of Photochemistry and Photobiology C: Photochemistry Reviews* **52,** 100530 (2022).
129. Lindinger, B, Mettin, R., Chow, R & Lauterborn, W. Ice crystallization induced by optical breakdown. *Physical review letters* **99,** 045701 (2007).
130. Irimia, D. *et al.* Influence of Laser Parameters and Experimental Conditions on Nonphotochemical Laser-Induced Nucleation of Glycine Polymorphs. *Crystal Growth and Design* **21,** 631–641 (2021).
131. Ward, M. R., Mackenzie, A. M. & Alexander, A. J. Role of impurity nanoparticles in laser-induced nucleation of ammonium chloride. *Crystal Growth & Design* **16,** 6790–6796 (2016).
132. Hueckel, T., Hocky, G. M. & Sacanna, S. Total synthesis of colloidal matter. *Nature Reviews Materials* **6,** 1053–1069 (2021).
133. Grzybowski, B. A. & Huck, W. T. The nanotechnology of life-inspired systems. *Nature Nanotechnology* **11,** 585–592 (2016).
134. Eder, M., Amini, S. & Fratzl, P. Biological composites—complex structures for functional diversity. *Science* **362,** 543–547 (2018).
135. Wuthrich, K., Weckhuysen, B., Rongy, L. & De Wit, A. *Computational Modeling: From Chemistry To Materials To Biology-Proceedings Of The 25th Solvay Conference On Chemistry* (World Scientific, 2020).
136. Helmbrecht, L., Futscher, M. H., Muscarella, L. A., Ehrler, B. & Noorduin, W. L. Ion exchange lithography: Localized ion exchange reactions for spatial patterning of perovskite semiconductors and insulators. *Advanced Materials* **33,** 2005291 (2021).
137. Van Rijt, M. M., Nooteboom, S. W., van der Weijden, A., Noorduin, W. L. & de With, G. Stability-limited ion-exchange of calcium with zinc in biomimetic hydroxyapatite. *Materials & Design* **207,** 109846 (2021).
138. Menichetti, A. *et al.* Local Light-Controlled Generation of Calcium Carbonate and Barium Carbonate Biomorphs via Photochemical Stimulation. *Chemistry–A European Journal* **27,** 12448 (2021).
139. Cosa, G., Martínez, L. J. & Scaiano, J. C. Influence of solvent polarity and base concentration on the photochemistry of ketoprofen: Independent singlet and triplet pathways. *Physical Chemistry Chemical Physics* **1,** 3533–3537 (1999).
140. Hamm, L. M. *et al.* Reconciling disparate views of template-directed nucleation through measurement of calcite nucleation kinetics and binding energies. *Proceedings of the National Academy of Sciences* **111,** 1304–1309 (2014).
141. Brinker, C. J. & Scherer, G. W. Sol-gel sciences. *The Processing and the Chemistry of Sol-Gel Processing* (1990).
142. Cui, Y., Li, H., Li, Y. & Mao, L. Novel insights into nanomaterials for immunomodulatory bone regeneration. *Nanoscale Advances* **4,** 334–352 (2022).
143. Meldrum, F. C. & Cölfen, H. The many lives of calcium carbonate. *Nature Chemistry* **15,** 1196 (2023).
144. Nakayama, M., Kajiyama, S., Kumamoto, A., Ikuhara, Y. & Kato, T. Bioinspired selective synthesis of liquid-crystalline nanocomposites: Formation of calcium carbonate-based composite nanodisks and nanorods. *Nanoscale Advances* **2,** 2326–2332 (2020).

145. Turali-Emre, E. S. *et al.* Self-Organization of Iron Sulfide Nanoparticles into Complex Multicompartment Supraparticles. *Advanced Materials* **35,** 1–17 (2023).
146. Isapour, G., Miller, B. H. & Kolle, M. Modular Assembly of Mechanoresponsive Color-Changing Materials from Hydrogel-Based Photonic Crystal Microspheres. *Advanced Photonics Research* **3,** 1–7 (2022).
147. Nahi, O. *et al.* Polyamines Promote Aragonite Nucleation and Generate Biomimetic Structures. *Advanced Science* **10,** 1–12 (2023).
148. Himel, M. H., Sikder, B., Ahmed, T. & Choudhury, S. M. Biomimicry in nanotechnology: a comprehensive review. *Nanoscale Advances* **5,** 596–614 (2022).
149. Xu, Z. *et al.* Formation of hierarchical bone-like apatites on silk microfiber templates: Via biomineralization. *RSC Advances* **6,** 76426–76433 (2016).
150. Kaplan, C. N. *et al.* Controlled growth and form of precipitating microsculptures. *Science* **355,** 1395–1399 (2017).
151. Kellermeier, M. *et al.* Additive-induced morphological tuning of self-assembled silica-barium carbonate crystal aggregates. *Journal of Crystal Growth* **311,** 2530–2541 (2009).
152. Batista, B. C. & Steinbock, O. Perovskite chemical gardens: highly fluorescent microtubes from self-assembly and ion exchange. *Chemical Communications* **58,** 12736–12739 (2022).
153. Bistervels, M. H., Kamp, M., Schoenmaker, H., Brouwer, A. M. & Noorduin, W. L. Light-Controlled Nucleation and Shaping of Self-Assembling Nanocomposites. *Advanced Materials* **34,** 2107843 (2022).
154. Boscá, F., Miranda, M. A., Carganico, G. & Mauleon, D. Photochemical and photobiological properties of ketoprofen associated with the benzophenone chromophore. *Photochemistry and photobiology* **60,** 96–101 (1994).
155. Cai, W. J. *et al.* Controls on surface water carbonate chemistry along North American ocean margins. *Nature Communications* **11,** 1–13 (2020).
156. Van Campenhout, C. T., Schoenmaker, H., van Hecke, M. & Noorduin, W. L. Patterning Complex Line Motifs in Thin Films Using Immersion-Controlled Reaction-Diffusion. *Advanced Materials* **35,** 1–8 (2023).
157. Wang, Q. & Steinbock, O. Shape-preserving conversion of calcium carbonate tubes to self-propelled micromotors. *Physical Chemistry Chemical Physics* **24,** 14538–14544 (2022).
158. Batista, B. C., Morris, A. Z. & Steinbock, O. Pattern selection by material aging: Modeling chemical gardens in two and three dimensions. *Proceedings of the National Academy of Sciences* **120,** 2017 (2023).
159. Barge, L. M. *et al.* From chemical gardens to chemobrionics. *Chemical Reviews* **115,** 8652–8703 (2015).
160. Xu, Y. F. *et al.* Intermolecular channels direct crystal orientation in mineralized collagen. *Nature Communications* **11,** 5068 (2020).
161. Albéric, M. *et al.* Heat-Mediated Micro- and Nano-pore Evolution in Sea Urchin Biominerals. *Crystal Growth and Design* **22,** 3727–3739 (2022).
162. Wu, X., Meldrum, F. C., Skipper, K., Yang, Y. & Royall, C. P. Tuning Higher Order Structure in Colloidal Fluids, 1–11. eprint: 2303.09029 (2023).
163. Bistervels, M. H., Antalicz, B., Kamp, M., Schoenmaker, H. & Noorduin, W. L. Light-driven nucleation, growth, and patterning of biorelevant crystals using resonant near-infrared laser heating. *Nature Communications* **14,** 1–9 (2023).

164. Bistervels, M. *et al.* Light-controlled morphological development of self-organizing bioinspired nanocomposites. *Nanoscale* (2024).
165. Van der Weijden, A., Léonard, A.-S. & Noorduin, W. L. Architected Metal Selenides via Sequential Cation and Anion Exchange on Self-Organizing Nanocomposites. *Chemistry of Materials* **35,** 2394–2401 (2023).
166. Van der Weijden, A., van Hecke, M. & Noorduin, W. L. Contraction and expansion of nanocomposites during Ion exchange reactions. *Crystal Growth & Design* **22,** 2289–2293 (2022).
167. Whitesides, G. M. *et al.* Noncovalent synthesis: using physical-organic chemistry to make aggregates. *Accounts of Chemical Research* **28,** 37–44 (1995).
168. Vantomme, G. & Meijer, E. The construction of supramolecular systems. *Science* **363,** 1396–1397 (2019).
169. Aslanbay Guler, B., Demirel, Z. & Imamoglu, E. Comparative Evaluation of Chemical Garden Growth Techniques. *Langmuir* **39** (2023).
170. Palin, D. *et al.* Forming Anisotropic Crystal Composites: Assessing the Mechanical Translation of Gel Network Anisotropy to Calcite Crystal Form. *Journal of the American Chemical Society* **143,** 3439–3447 (2021).
171. Schenk, A. S. *et al.* Hierarchical calcite crystals with occlusions of a simple polyelectrolyte mimic complex biomineral structures. *Advanced functional materials* **22,** 4668–4676 (2012).
172. Hedegaard, C. L. & Mata, A. Integrating self-assembly and biofabrication for the development of structures with enhanced complexity and hierarchical control. *Biofabrication* **12,** 032002 (2020).
173. Schiffmann, N. *et al.* Characterization and possible function of an enigmatic reflector in the eye of the shrimp Litopenaeus vannamei. *Faraday Discussions* **223,** 278–294 (2020).
174. Li, L. & Ortiz, C. Biological design for simultaneous optical transparency and mechanical robustness in the shell of placuna placenta. *Advanced Materials* **25,** 2344–2350 (2013).
175. Hyde, S. T. & Meldrum, F. C. Starfish grow extraordinary crystals. *Science* **375,** 615–616 (2022).
176. Cai, J. *et al.* Polarization-sensitive optoionic membranes from chiral plasmonic nanoparticles. *Nature Nanotechnology* **17,** 408–416 (2022).
177. Zhang, J. *et al.* Cooperative photoinduced metastable phase control in strained manganite films. *Nature materials* **15,** 956–960 (2016).
178. Schaffner, M., England, G., Kolle, M., Aizenberg, J. & Vogel, N. Combining Bottom-Up Self-Assembly with Top-Down Microfabrication to Create Hierarchical Inverse Opals with High Structural Order. *Small* **11,** 4334–4340 (2015).
179. Shaked, H., Polishchuk, I., Nagel, A., Bekenstein, Y. & Pokroy, B. Long-term stabilized amorphous calcium carbonate—an ink for bio-inspired 3D printing. *Materials Today Bio* **11,** 100120 (2021).
180. Mann, S., Heywood, B. R., Rajam, S. & Birchall, J. D. Controlled crystallization of $CaCO_3$ under stearic acid monolayers. *Nature* **334,** 692–695 (1988).
181. Li, L., Sanchez, J. R., Kohler, F., Røyne, A. & Dysthe, D. K. Microfluidic Control of Nucleation and Growth of $CaCO_3$. *Crystal Growth and Design* **18,** 4528–4535. eprint: 1708.06299 (2018).
182. Zeng, M. *et al.* Confinement generates single-crystal aragonite rods at room temperature. *Proceedings of the National Academy of Sciences of the United States of America* **115,** 7670–7675 (2018).
183. Meldrum, F. C. & O'Shaughnessy, C. Crystallization in confinement. *Advanced Materials* **32,** 2001068 (2020).
184. Song, R. Q. *et al.* Formation of Periodically-Ordered Calcium Phosphate Nanostructures by Block Copolymer-Directed Self-Assembly. *Chemistry of Materials* **28,** 838–847 (2016).

185. Hatton, B. D. & Aizenberg, J. Writing on superhydrophobic nanopost arrays: Topographic design for bottom-up assembly. *Nano Letters* **12,** 4551–4557 (2012).
186. Deng, X. *et al.* Topographically guided hierarchical mineralization. *Materials Today Bio* **11,** 100119 (2021).
187. Kim, K. S. *et al.* Non-epitaxial single-crystal 2D material growth by geometric confinement. *Nature* **614,** 88–94 (2023).
188. Grommet, A. B., Lee, L. M. & Klajn, R. Molecular Photoswitching in Confined Spaces. *Accounts of chemical research* **53,** 2600–2610 (2020).
189. Niehues, M., Engel, S. & Ravoo, B. J. Photo-Responsive Self-Assembly of Plasmonic Magnetic Janus Nanoparticles. *Langmuir* **37,** 11123–11130 (2021).
190. Almeida, M. *et al.* Laser induced crystallization of Co–Fe–B films. *Scientific Reports* **11,** 14104 (2021).
191. Sun, K. *et al.* Three-dimensional direct lithography of stable perovskite nanocrystals in glass. *Science* **375,** 307–310 (2022).
192. Holmstrom, E. D. & Nesbitt, D. J. Real-Time Infrared Overtone Laser Control of Temperature in Picoliter H(2)O Samples: "Nanobathtubs" for Single Molecule Microscopy. *The journal of physical chemistry letters* **1,** 2264–2268 (2010).
193. De Lorenzo, S., Ribezzi-Crivellari, M., Ricardo Arias-Gonzalez, J, Smith, S. B. & Ritort, F. A Temperature-Jump Optical Trap for Single-Molecule Manipulation. *Biophysical Journal* **108,** 2854–2864 (2015).
194. Viger, M. L. *et al.* Near-infrared-induced heating of confined water in polymeric particles for efficient payload release. *ACS Nano* **8,** 4815–4826 (2014).
195. Miller, J. P. A portion of the system calcium carbonate-carbon dioxide-water, with geological implications. *American Journal of Science* **250,** 161–203 (1952).
196. McDowell, H, Gregory, T. M. & Brown, W. E. Solubility of $Ca_5(PO_4)_3OH$ in the system $Ca(OH)_2$-$H3PO_4$-H2O at 5-degrees-C, 15-degrees-C, 25-degrees-C and 37-degrees-C. *Journal of Research of the National Bureau of Standards* **81A,** 273 (1977).
197. Saidaminov, M. I., Abdelhady, A. L., Maculan, G. & Bakr, O. M. Retrograde solubility of formamidinium and methylammonium lead halide perovskites enabling rapid single crystal growth. *Chemical Communications* **51,** 17658–17661 (2015).
198. Nandi, N. & Sahu, K. Analysis of excited state proton transfer dynamics of HPTS in methanol-water mixtures from time-resolved area-normalised emission spectrum (TRANES). *Journal of Photochemistry and Photobiology A: Chemistry* **374,** 138–144 (2019).
199. Boon, M., Rickard, W. D., Rohl, A. L. & Jones, F. Stabilization of Aragonite: Role of Mg2+and Other Impurity Ions. *Crystal Growth and Design* **20,** 5006–5017 (2020).
200. Wehrmeister, U., Jacob, D., Soldati, A., Häger, T. & Hofmeister, W. Vaterite in freshwater cultured pearls from China and Japan. *The Journal of Gemmology* **30,** 399–412 (2007).
201. Busenberg, E., Plummer, L. N. & Parker, V. B. The solubility of strontianite ($SrCO_3$) in CO_2-H2O solutions between 2 and 91°C, the association constants of $SrHCO^{+3}$(aq) and $SrCO_{+3}$(aq) between 5 and 80°C, and an evaluation of the thermodynamic properties of Sr2+(aq) and $SrCO_3$(cr) at 25°C and 1 atm total pressure. *Geochimica et Cosmochimica Acta* **48,** 2021–2035 (1984).
202. Busenberg, E. & Plummer, L. N. The solubility of $BaCO_3$(cr) (witherite) in CO_2-H2O solutions between 0 and 90°C, evaluation of the association constants of $BaHCO_3^+$(aq) and $BaCO_3^0$(aq) between 5 and 80°C, and a preliminary evaluation of the thermodynamic properties of Ba^{2+}(aq). *Geochimica et Cosmochimica Acta* **50,** 2225–2233 (1986).
203. Kaabar, W., Bott, S. & Devonshire, R. Raman spectroscopic study of mixed carbonate materials. *Spectrochimica Acta Part A: Molecular and Biomolecular Spectroscopy* **78,** 136–141 (2011).

204. Safari, H., Shokrollahi, A., Moslemizadeh, A., Jamialahmadi, M. & Ghazanfari, M. H. Predicting the solubility of $SrSO_4$ in Na-Ca-Mg-Sr-Cl-SO_4-H2O system at elevated temperatures and pressures. *Fluid Phase Equilibria* **374,** 86–101 (2014).
205. Stammeier, J. A., Purgstaller, B., Hippler, D., Mavromatis, V. & Dietzel, M. In-situ Raman spectroscopy of amorphous calcium phosphate to crystalline hydroxyapatite transformation. *MethodsX* **5,** 1241–1250 (2018).
206. Chen, Y. H., Huang, E. & Yu, S. C. High-pressure Raman study on the $BaSO_4$ - $SrSO_4$ series. *Solid State Communications* **149,** 2050–2052 (2009).
207. Regehly, M. *et al.* Xolography for linear volumetric 3D printing The range of applications for additive manufacturing is expanding quickly, including mass production of athletic footwear parts. *Nature* **588,** 620–624 (2020).
208. Hertlein, C., Helden, L., Gambassi, A., Dietrich, S. & Bechinger, C. Direct measurement of critical Casimir forces. *Nature* **451,** 172–175 (2008).
209. Zhang, G., Verdugo-Escamilla, C., Choquesillo-Lazarte, D. & García-Ruiz, J. M. Thermal assisted self-organization of calcium carbonate. *Nature Communications* **9,** 1–7 (2018).
210. Van Der Burgt, J. S. *et al.* Integrating Sphere Fourier Microscopy of Highly Directional Emission. *ACS Photonics* **8,** 1143–1151 (2021).
211. Zhang, C. *et al.* Nano/Micro-Manufacturing of Bioinspired Materials: a Review of Methods to Mimic Natural Structures. *Advanced Materials,* 6292–6321.
212. Liu, K. *et al.* 3D printing colloidal crystal microstructures via sacrificial-scaffold-mediated two-photon lithography. *Nature Communications* **13,** 4563 (2022).
213. Yang, D.-L., Faraz, F., Wang, J.-X. & Radacsi, N. Combination of 3D printing and electrospinning techniques for biofabrication. *Advanced Materials Technologies* **7,** 2101309 (2022).
214. Gagey, N., Neveu, P. & Jullien, L. Two-photon uncaging with the efficient 3, 5-dibromo-2, 4-dihydroxycinnamic caging group. *Angewandte Chemie* **119,** 2519–2521 (2007).
215. Scaiano, J., Johnston, L., McGimpsey, W. & Weir, D. Photochemistry of organic reaction intermediates: novel reaction paths induced by two-photon laser excitation. *Accounts of Chemical Research* **21,** 22–29 (1988).
216. Saccone, M. A., Gallivan, R. A., Narita, K., Yee, D. W. & Greer, J. R. Additive manufacturing of micro-architected metals via hydrogel infusion. *Nature* **612,** 685–690 (2022).
217. Li, F. *et al.* 3D printing of inorganic nanomaterials by photochemically bonding colloidal nanocrystals. *Science* **381,** 1468–1474 (2023).
218. Han, F. *et al.* Three-dimensional nanofabrication via ultrafast laser patterning and kinetically regulated material assembly. *Science* **378,** 1325–1331 (2022).
219. Baldacchini, T. *et al.* Translation of laser-based three-dimensional printing technologies. *MRS Bulletin* **46,** 174–185 (2021).
220. Zheng, L. *et al.* Nanofabrication of high-resolution periodic structures with a gap size below 100 nm by two-photon polymerization. *Nanoscale research letters* **14,** 1–9 (2019).
221. Chopelas, A. Single crystal Raman spectra of forsterite, fayalite, and monticellite. *American Mineralogist* **76,** 1101–1109 (1991).
222. Foster, N., Wozniakiewicz, P. J., Price, M. C., Kearsley, A. T. & Burchell, M. J. Identification by Raman spectroscopy of Mg–Fe content of olivine samples after impact at 6 km s- 1 onto aluminium foil and aerogel: In the laboratory and in Wild-2 cometary samples. *Geochimica et Cosmochimica Acta* **121,** 1–14 (2013).

223. Ferrari, A. C. & Robertson, J. Interpretation of Raman spectra of disordered and amorphous carbon. *Physical review B* **61,** 14095 (2000).
224. Bruno C. Batistaa, Amari Z. Morrisa & Steinbock, O. Pattern selection by material aging: Modeling chemical gardens in two and three dimensions. *Proceedings of the National Academy of Sciences* **120,** 1–8 (2023).
225. Van Campenhout, C. T., Ten Napel, D. N., van Hecke, M. & Noorduin, W. L. Rapid formation of uniformly layered materials by coupling reaction–diffusion processes with mechanical responsiveness. *Proceedings of the National Academy of Sciences* **119,** e2123156119 (2022).
226. Escárcega-Bobadilla, M. V., Maldonado-Domínguez, M., Romero-Ávila, M. & Zelada-Guillén, G. A. Turing patterns by supramolecular self-assembly of a single salphen building block. *Iscience* **25** (2022).
227. Yang, Y. *et al.* Maintenance of the Metastable State and Induced Precipitation of Dissolved Neodymium (III) in an Na_2CO_3 Solution. *Minerals 2021, Vol. 11, Page 952* **11,** 952 (2021).
228. Li, J., Zhang, X., Nie, J. & Zhu, X. Visible light and water-soluble photoinitiating system based on the charge transfer complex for free radical photopolymerization. *Journal of Photochemistry and Photobiology A: Chemistry* **402,** 112803 (2020).
229. Falini, G. *et al.* Polymeric admixtures effects on calcium carbonate crystallization: relevance to cement industries and biomineralization. *CrystEngComm* **9,** 1162–1170 (2007).
230. Donners, J. J. J. M. *et al.* Control over Calcium Carbonate Phase Formation by Dendrimer/Surfactant Templates.
231. Guru, S., Bajpai, A. K. & Amritphale, S. S. Influence of nature of surfactant and precursor salt anion on the microwave assisted synthesis of barium carbonate nanoparticles. *Materials Chemistry and Physics* **241** (2020).
232. Wong, K.-L., Bünzli, J.-C. G. & Tanner, P. A. Quantum yield and brightness. *Journal of Luminescence* **224,** 117256 (2020).
233. Musa, K. A., Matxain, J. M. & Eriksson, L. A. Mechanism of photoinduced decomposition of ketoprofen. *Journal of Medicinal Chemistry* **50,** 1735–1743 (2007).
234. Beer, A. *Grundriß des photometrischen Calcüles.-Braunschweig, Friedrich Vieweg u. Sohn 1854* (Vieweg, 1854).
235. Beer. Bestimmung der Absorption des rothen Lichts in farbigen Flüssigkeiten. *Annalen der Physik* **162,** 78–88 (1852).
236. Schlag, E.-W., Schneider, S & Fischer, S. Lifetimes in excited states. *Annual Review of Physical Chemistry* **22,** 465–526 (1971).
237. Ankudinov, V., Bobashev, S. & Andreev, E. Measurement of lifetimes of excited states of the hydrogen atom. *Soviet Physics Jetp* **21** (1965).
238. Zatryb, G & Klak, M. On the choice of proper average lifetime formula for an ensemble of emitters showing non-single exponential photoluminescence decay. *Journal of Physics: Condensed Matter* **32,** 415902 (2020).
239. Ramamurthy, V. Photochemistry within a water-soluble organic capsule. *Accounts of chemical research* **48,** 2904–2917 (2015).
240. Besirske, P. *et al.* Localized Crystallization of Calcium Phosphates by Light-Induced Processes. *Chemistry–A European Journal,* e202302327 (2023).
241. Carleer, M. *et al.* The near infrared, visible, and near ultraviolet overtone spectrum of water. *The Journal of chemical physics* **111,** 2444–2450 (1999).

242. Jeong, J. *et al.* Pseudo-halide anion engineering for α-FAPbI3 perovskite solar cells. *Nature* **592,** 381–385 (2021).
243. Gonnella, G., Lamura, A., Piscitelli, A. & Tiribocchi, A. Phase separation of binary fluids with dynamic temperature. *Physical Review E* **82,** 046302 (2010).
244. Korotkevich, A. A. & Bakker, H. J. Confined Water Molecules in Binary Mixtures of Water and 2, 6-Lutidine Near Lower Solution Critical Temperature. *The Journal of Physical Chemistry B* **125,** 287–296 (2020).
245. Baffou, G., Bordacchini, I., Baldi, A. & Quidant, R. Simple experimental procedures to distinguish photothermal from hot-carrier processes in plasmonics. *Light: Science & Applications* **9,** 108 (2020).
246. Baldi, A. & Askes, S. H. Pulsed Photothermal Heterogeneous Catalysis. *ACS catalysis* **13,** 3419–3432 (2023).
247. Hale, G. M. & Querry, M. R. Optical constants of water in the 200-nm to 200-μm wavelength region. *Applied optics* **12,** 555–563 (1973).
248. Sabnis, R. W. *Handbook of fluorescent dyes and probes* (John Wiley & Sons, 2015).

Acknowledgements

In this section, I want to articulate my experiences from the past years and express what I am grateful for. And phew, it took me some time to put this on paper, but not because I had nothing to say—far from it! These have been such intense years filled with events, during which I've had the privilege to learn from many people in various areas, making it feel almost impossible to weave it all into a coherent narrative.

As I reflect on the past years, one word keeps coming back: 'development.' And by development, I don't just mean scientific progress—the 'what' that is mostly central to our research. I'm referring to mental development—the 'how' that precedes, accompanies, or sometimes stands apart from the scientific 'what.' While this 'what' is the promised product of a PhD, many who have walked this path would likely agree that the personal outcome is much more about the abstract 'how', a kind of development in your way of thinking and being, built from knowledge, setbacks, and the freedom that the PhD journey entails. I even would like to say that the scientific 'what' cannot be defined without developing this 'how,' in both practical and philosophical terms. You have to literally 'uitdokteren,' which is probably why you become a doctor.

Although this concept may seem vague, it is crystal clear to me now. I am incredibly grateful for the 'how's' that I have been able to develop over the past years. Of course, it's hard to find references in life because we only live one life that we consciously experience. So, I can't say whether I would have gone through the same mental development if I had done something else. But I do know that pursuing a PhD certainly challenged me, and it was almost inevitable to work on my personal growth.

I also know that I experienced AMOLF, with the people who were there day in and day out, as a wonderful and safe space. A place where I could be myself, where I could bump my head (literally and figuratively), and where I could grow. Here, I could laugh, cry, be frustrated and grumpy, but also feel enthusiastic and inspired. I could tackle challenges and turn the most outrageous ideas into reality. In this part of my thesis, I want to thank everyone—both within AMOLF and beyond—who has supported me on my journey. Since I get nervous thinking about forgetting someone, I'll keep it brief. But if you're reading this, you're likely someone who contributed. Feel free to call me, and I'll gladly share my gratitude personally.

The first person I am very grateful to and want to thank is my supervisor and promoter, Wim. Dear Wim, from our very first conversation, you made me feel like I wanted to learn so much from you—not just scientifically, but especially about how you interact with people and life. You told me that a PhD

is an opportunity to discover many new things and develop yourself in various ways, and that you genuinely enjoy guiding people through this process. Now, five years later, I know you were not lying, and I consider myself incredibly lucky to have had you as my mentor. You care deeply about your students and prioritize their well-being. From day one, you made me feel that you had confidence in me, which gave me the strength and motivation to dive in wholeheartedly, rise up, and flourish in what I had to do! Moreover, you brought joy and humor to every meeting, allowing me to confidently say that this PhD was anything but boring, and I truly had fun!

Closely connected to the group leader is, of course, the group itself—an research group doesn't exist without its members! Iarik, Hans, Lukas, Arno, followed by Christiaan, Sjoerd, Ariane, and finally Anne-Sophie, Marius, and Susanna. The temporary presence of Nesrin, Stivell, Pietro, Kendra, Imane, Miriam, Jeppe, Niels, Emma, Diede, and Ilias also contributed to this. Each of you is a unique figure, with your own passion, talent, personality, and quirks. I've enjoyed and learned from each one of you. You've inspired me both professionally and personally. The group was a place where I could truly be myself, probably because everyone else was too. Thank you for the endless joy, the interesting discussions, the shared frustrations, and the unconditional support.

Two very special places in the group, and even more special in my work, are for Marko and Hinco. Dear Marko and Hinco, you have been invaluable to me, and I want to thank you immensely for all the help, lessons, and inspiration I've gained from you. Not only have I learned a lot from you, but I also had an incredible amount of fun working together. You were always ready to help me, even having the patience to deal with my impatience and enthusiasm, and you were always intensely involved in every project. You are truly part of the foundation upon which AMOLF is built.

I also want to thank all the support staff at AMOLF: the workshop team, technical and chemical facilities, the nanolab, reception, secretariat, procurement, finance, the drawing room, marketing/PR—everything that happens at AMOLF is made possible by you!

And I would like to give a special thanks to my office mates, Lori and Kevin. Our office was truly a safe space, although that may have been a bit different for you with me around. I'm just glad I got to share that space with you and that we could occasionally unwind during what I like to call an expression session!

Of course, I want to thank my co-promoter, Fred, for the useful discussions, valuable input, and sharp observations. Your scientific advice was key to the success of many projects described in this book. I appreciate your attention to detail and your help in refining the work right up to the very last moment.

I also want to thank my entire committee for the time and effort you dedicated to my defense, but especially for being an inspiration and role model in this academic world. I feel very honored to have you as my committee.

My development over the past years hasn't just been shaped by people at AMOLF. However, since I don't know where to begin or end, I'll keep this brief. I certainly want to thank my parents for their constant encouragement and support in what I do, and I am 1000 times grateful for all my friends and acquaintances who kept me on the necessary days away from AMOLF and entertained me with fun, emotions, support, parties, dinners, vacations, good conversations, challenges, and adventures of all kinds. A special thank you to Sanne and Hannah, who were for me the best reason to attend lectures since the very first day of our studies, enabling me to end up here.

I also want to express my gratitude to those who helped me with a personal project—let's just call it the HC-project. Although this project might seem far removed from the work in this book, it greatly contributed to my well-being and is inextricably linked to how I approached my research. It was a significant challenge, harder and heavier than all the laws of nature described in this book. But it was worth every cell in my body. In particular, I want to mention Aafke and Simone. Dear Aafke and Simone, thank you for your trust, guidance, and the insights you provided me. Where I had already given up, you hadn't, and you offered me something I didn't even know existed for me. I also want to thank my sister and express my endless gratitude to Karin and Hannah for holding my hand. With you by my side, I didn't have to do this alone. I wish for everyone the experience of diving into the deep end and emerging like a dolphin. It's the greatest gift you can give yourself and your relationships.

With that wisdom, I would like to conclude this acknowledgment. Don't forget to call me if your name isn't mentioned here—there are many of you. Then we can have a personal tribute over the phone or enjoy a drink together!